약학박사학위논문

섬유증 및 종양 미세환경 내에서 활성화되도록 설계된 약물 전달 시스템 개발 연구

Programmed drug delivery systems activated in the fibrotic and tumor microenvironment

2023 년 2월

서울대학교 대학원
약학과 약제학 전공
변 준 호

섬유증 및 종양 미세환경 내에서 활성화되도록 설계된 약물 전달 시스템 개발 연구

Programmed drug delivery systems activated in the fibrotic and tumor microenvironment

지도 교수 이 우 인

이 논문을 약학박사 학위논문으로 제출함

2022년 11월

서울대학교 대학원
약학과 약제학 전공

변 준 호

변준호의 약학박사 학위논문을 인준함

2022년 12월

위 원 장 변 영 로 (인)

부위원장 김 대 덕 (인)

위 원 최 한 곤 (인)

위 원 임 수 정 (인)

위 원 이 우 인 (인)

Abstract

Programmed drug delivery systems activated in the fibrotic and tumor microenvironment

Junho Byun

Department of Pharmaceutical Sciences

College of Pharmacy

The Graduate School

Seoul National University

The microenvironment plays a crucial role in both the progression and treatment of diseases including tumor and hepatic fibrosis. However, current therapeutics are non-targeting or cell-targeting agents which can induce systemic adverse effects. The limited therapeutic efficacy of these agents was mainly associated with the deleterious microenvironment of the tissue. Therefore, strategies for targeted modulation of the microenvironment should be further investigated. Herein, we developed the programmed drug delivery systems that can be activated by exogenous or endogenous stimuli at the tumor and fibrotic microenvironment. This thesis work is composed of two parts, which are the exogenous stimuli-actuated delivery system for tumor immune microenvironment modulation and peptide-delivery nanotherapeutic for regulation of fibrotic microenvironment.

In Part I, we developed stimuli-responsive delivery platforms that are programmed to be activated by light or cold atmospheric plasma (CAP). With these delivery systems, our goal was to eradicate primary tumors as well as distant tumors following immune microenvironment activation. In the first chapter, the gold-DNA nanocluster was developed for photo-immunotherapy on a tumor. Previous studies mainly used one light source for a single type of phototherapy, such as photothermal or photodynamic therapy, which has limited therapeutic efficacy as well as insufficient immune reaction. In this

context, we designed gold-DNA nanocluster intercalating methylene blue for dual-light activated photo-immunotherapy. By exploiting a CpG sequence as a template for DNA polymer, delivery of nucleic acid to the dendritic cell was achieved to activate the tumor immune microenvironment followed by the prevention of distant tumor growth. Our in vivo study suggest that systemic injection of the nanocluster elicited enhanced tumor eradication and immune activation at the tumor site after the dual-light irradiation. In the second chapter, we developed programmed antigen-releasing hydrogel actuated by CAP irradiation. Previous clinical trials have utilized CAP for residual tumor removal, however, its limited penetration depth has limited its effectiveness in treating primary tumors. Our findings show that the CAP-activated hydrogel system is capable of sustained release of both tumor antigen and TGF-beta inhibitor, leading to increased anti-tumor immune response and primary as well as distant tumor eradication. These results highlight the potential of the CAP-responsive in situ hydrogel system as a promising therapeutic platform for overcoming the limitations of CAP's depth-related restriction in treating primary tumors.

In part II of the thesis, the fibrotic microenvironment was modulated for the treatment of liver fibrosis. We designed an anti-fibrotic peptide delivery system that is programmed to be liberated by activated hepatic stellate cells (aHSCs). Despite the urgent global needs, there is no clinically approved therapeutic for liver fibrosis. In the fibrotic microenvironment, aHSCs play a central role in fibrogenesis and express distinct enzyme proteins such as fibroblast activation protein (FAP). Our goal was selective eradication of aHSCs in the fibrotic liver by exploiting promelittin, which is a FAP-responsive prodrug form of melittin. Treatment of promelittin-conjugated liposome could elicit anti-fibrotic effects in three different hepatic fibrosis models as well as apoptosis of aHSC. Although this peptide-delivery system was tested in liver fibrosis, it could be applied to other fibrotic diseases, such as lung fibrosis and cardiac fibrosis.

Taken together, studies on programmed in situ drug delivery systems, which can be activated by stimuli, were achieved in this thesis work and showed promising therapeutic effects following the modulation of the tumor and fibrotic microenvironment. Furthermore, the drug delivery strategies suggested in this thesis address the current limitation of the therapeutics, which can broaden the current therapeutic indication.

Keywords : Drug delivery system, tumor microenvironment, immunotherapy, fibrotic microenvironment, biologics delivery

Student Number : 2017-20756

Contents

Part II. Modulation of the fibrotic microenvironment

List of Tables

Chapter I

List of Figures

Chapter I

Chapter II

Chapter III

Chapter IV

Chapter I

Overview

1. Disease and the tissue microenvironment

Recently, the tissue microenvironment has received a great deal of attention for its crucial role in the progression of disease [1, 2]. During the disease progression, unfavorable stimulation could elicit the complex interaction between the diseased cell and its surroundings, which involves secretion of cytokines, immune cell polarization, proliferation of specific cells, and metabolic reprogramming followed by aggravation of the disease [3-5]. Although the aspect of the interactions is diverse with the characteristics of the diseases, the unfavorable effect of microenvironment is considered to primary hurdle for the clinical translation of the therapeutics [2, 6] (Table 1).

Table 1. Distinct features of microenvironment diseased tissues

Type of microenvironment	Disease & Tissue	Feature	Reference
Tumor microenvironment			
Tumor cells		PDL-1 overexpression	[4, 7, 24]
M2 macrophages		Increased population	[3, 8, 14]
M1 macrophages		Decreased population, Anti-tumor	[8, 9, 29, 30]
Exhausted CD8 T cells		PD-1 overexpression, Pro-tumor	[10-12, 24]
Adipocytes	Obesity	Inflammation, Pro-tumor	[2]
Cancer-associated fibroblasts		FAP overexpression, Immune suppression	[13]
Tolerogenic dendritic cells		T cell exhaustion	[12, 32]
Regulatory CD4 T cells		Pro-tumor Anti-inflammatory effect	[3, 14]
Hypoxia		Pro-tumor, Acidification induction	[7, 15, 16, 17]
Acidosis		Pro-tumor, Metabolic change	[12, 16]
Granulocyte colony-stimulating factor		Overexpression, Pro-tumor	[18]
Lysyl oxidase–like-2		Promotion of tumor metastasis	[19]
Fibrotic disease			
Hepatic stellate cells	Liver	Activated and proliferated, Fibrogenic cell, Fibroblast activation protein overexpression	[20]
CD8+ T cell		Decreased population	[21, 23]
NK cells		Decreased population	[22]
Tumor necrosis factor-alpha		Inflammation, Pro-fibrotic	[24]
IL-6		Inflammation, Pro-fibrotic	[20]
Regulatory CD4+ T cells	Heart	Protective function	[40]
Macrophages		Involve in inflammation and resolution of fibrosis	[18, 44]
Autoimmune diseases			
T helper 17 cells	Rheumatoid arthritis	Pro-inflammatory, Promotes autoimmune disease	[25]
Regulatory CD4 T cells		Anti-inflammatory, Resolution of autoimmune disease	[26]
Infection			
CD8 T cells			[27]
Macrophages			[28]

Among the various diseases, tumor microenvironment has been widely investigated in terms of negative interaction with an abnormal tumor cell and their immune suppressive coexisting cells including regulatory CD4 T cells, M2 macrophages, tolerogenic dendritic cells and cancer-associated fibroblasts [3, 4, 29, 30]. Tumor-associated macrophages, which were composed mainly of M2-phenotype macrophages, are known to promote tumor development by inducing chronic inflammation with tumor-promoting factors such as transforming growth factor, vascular endothelial growth factor, and interleukin 4 [14, 31]. Also, the function of dendritic cells, which is a major antigen-presenting cell for T cell activation, is deteriorated by the immunosuppressive tumor microenvironment [32]. Additionally, other factors that composed the microenvironment also play an essential role, which are hypoxia, angiogenesis, extracellular matrix, low pH, and metabolites [7, 12]. An increased population of exhausted CD8+ T cells, which showed high expression of PD-1, is also a specific feature of the tumor microenvironment [24]. Although chemotherapeutics, which directly target the tumor cells that have abnormal cell cycle patterns, were the mainstream for anti-cancer therapy with meaningful progress, therapeutic efficacy was not sufficient enough mainly due to the diversity of the tumor and complexity of the microenvironment. Targeting the component of the tumor microenvironment for anti-tumor therapy has been considered a promising way to overcome traditional cancer therapy [31, 33]. In this context, an immune checkpoint inhibitor, which leads to great success in immunotherapy, showed a convincing therapeutic effect on certain types of tumors by blocking highly expressed immune checkpoints like PD-1 on exhausted CD8+ T cells [7, 34]. Therefore, modulation of the tumor microenvironment with therapeutic modifiers has the potential to bring benefits to both chemotherapy and immunotherapy [35].

Besides cancer, fibrotic disease has also distinct microenvironment features represented by activated fibroblast and excess extracellular matrix. It is known that immune cells in the microenvironment also significantly affect fibrogenesis such as macrophages and T cells [36-38]. As seen in various fibrotic diseases including liver, pulmonary, kidney, and cardiac fibrosis, pro-fibrotic factors derived from multi-directional crosstalk within the microenvironment can aggravate the fibrosis progression, leading to organ failure [20, 39, 40]. An abundance of fibrosis-related cytokines and enzymes in the fibrotic microenvironment is a crucial factor for fibrogenesis, such as IL-10, TGF-beta, matrix metalloproteinases, and fibroblast activation protein [40-42]. To ameliorate the severity of fibrosis, remodeling of the fibrotic microenvironment is needed such as depletion of activated fibroblasts and reprogramming of pro-fibrotic immune cells [8, 43]. Recent studies showed that regulatory T cells have protective functions for cardiac fibrosis resulting in the improvement of myocardial infarction-related lethal symptoms [40]. Also, macrophages play a crucial role in inducing inflammation in the injured

lung followed by lung fibrosis progression [44]. It was reported that hepatic macrophages play a central role in the resolution of liver fibrosis for the treatment of relaxin, which is known as the anti-fibrotic hormone, by a switch of phenotype from fibrogenic to resolution state [8]. For liver fibrosis progression, hepatic stellate cell act as central role as principal collagen-producing cells in the liver microenvironment, which can be activated with complex interaction with surrounding liver cells [45, 46]. Therefore, specific ablation of the fibrotic cells in the microenvironment can be a promising therapeutic approach for diverse fibrotic diseases.

As described above, the microenvironment of disease site has gained tremendous attention for its multifacet properties, not only enemy should be conquered, but also exploitable component [47, 48]. Therapeutic approaches for targeting the microenvironment could be novel treatment options for incurable diseases as well as broaden the therapeutic options by overcoming the limitation of current therapeutics [4, 9, 42].

2. Stimuli-responsive drug delivery systems

For decades, the development of medicine is challenging mainly due to its complex and unpredictable pharmacological issues as well as pharmacokinetic problems after administration [49-51]. Although there were tremendous feasible results in preclinical studies, systemic toxicity and off-target effect hinder the clinical translation of the drugs [52]. Inadequate drug amount reaching disease area also contribute to unsatisfactory drug development [53].

Recently, as therapeutic biomaterials and nanotechnology evolved, there is great interest in the development of drug delivery systems that specifically target the disease site without systemic adverse effects [54, 55]. For this purpose, diverse targeting strategies were investigated for nanomedicine delivery. For targeting the tumor tissue, the most popular targeting strategy is the enhanced permeability and retention (EPR) effect for passive accumulation [50, 54]. Additionally, active targeting strategies were also widely investigated by the conjugation of target-specific ligands on the nanoparticles. Nanoparticles can actively target the various molecules on the surface of pathogenic cells. Various moieties can be exploited for active targetings, such as antibodies, aptamers, peptides, small molecules, and polymers. For example, mannose is widely used for targeting moiety the macrophage that overexpresses mannose receptors [56]. However, the therapeutic efficiency of these strategies is controversial and mostly insufficient for clinical application.

Stimuli-responsive drug delivery system, which can induce a therapeutic effect on the stimuli-applied area, is a promising strategy in terms of targeting efficiency. Diverse types of stimuli that could apply to the drug delivery system have been reported and can be classified as exogenous stimuli and endogeneous stimuli.

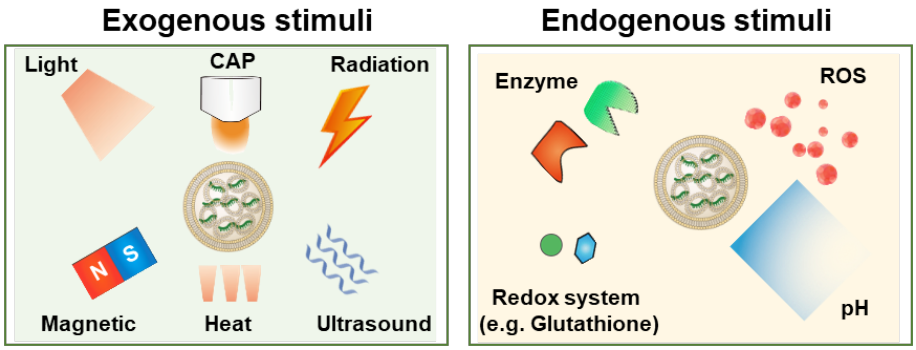

Figure 1. Types of exogenous stimuli and endogenous stimuli

Exogeneous stimuli-responsive drug delivery systems exploit external sources for the stimulation, such as light, cold atmospheric plasma, ultrasound, heat, and radiation. The therapeutic effect of the system can be accomplished by external stimuli itself or stimuli-actuated drugs. The light-responsive

therapeutic system is maybe the most widely investigated in the context of photodynamic therapy and photothermal therapy. Along with specific wavelengths of light, photosensitizers such as chlorin e6 and indocyanine green can generate reactive oxygen species [57, 58]. Also, some materials including gold nanoparticles, polydopamine, melanin, and graphene can increase their temperature after light exposure [59-61]. Cold atmospheric plasma, the ionized gas with reactive oxygen species, has been reported as a clinical tool for anti-bacterial, wound healing, and tumor treatment [62-64].

For the endogeneous stimuli-responsive delivery systems, distinct pathophysiological properties of the microenvironment at diseased tissues were used as stimuli to activate therapeutics. An overexpressed enzyme, distinguished redox system, pH, reactive oxygen species, and metabolites can be employed as a tool to activate the delivery system. Since the high expression level of matrix metalloproteinase (MMP) is a well-known feature of the tumor microenvironment, the MMP-cleavable peptide sequence can be used for an MMP-actuated delivery system [23]. Harnessing the excessive amount of ROS in colitis, ROS cleavable polymer was used to formulate colitis-targeted delivery of therapeutics [65].

3. Scope of the study

In my Ph.D. thesis, I aimed to develop a stimuli-responsive drug delivery system that can interact with the microenvironment of disease tissue. Since the microenvironment has multifaced characteristics of disease development, I proposed two different approaches. First, considering the microenvironment as a foe to conquer, I revised the pathogenic microenvironment with an external stimuli-responsive system into a feasible condition for curing the disease. On the other hand, I got benefits from the microenvironment by exploiting endogenous enzymes to design the internal stimuli-responsive peptide delivery system.

Specifically, exogenous stimuli including red-infrared dual light and cold atmospheric plasma were investigated to modulate the tumor microenvironment, respectively. I focused on the improvement of adaptive immune response in terms of anti-tumoral dendritic cell and T cell activation with the assistance of a drug delivery system.

Additionally, modulation of pathogenic cell population in the fibrotic microenvironment has been investigated, by using a cell-specific marker as internal stimuli. In this context, hepatic fibrosis was used for the disease model and fibroblast activation protein, which showed distinctively high expression on activated fibroblast, was exploited for the endogenous stimuli. I intend to deliver anti-fibrotic peptides and deplete activated fibroblast in the microenvironment resulting in the resolution of fibrosis.

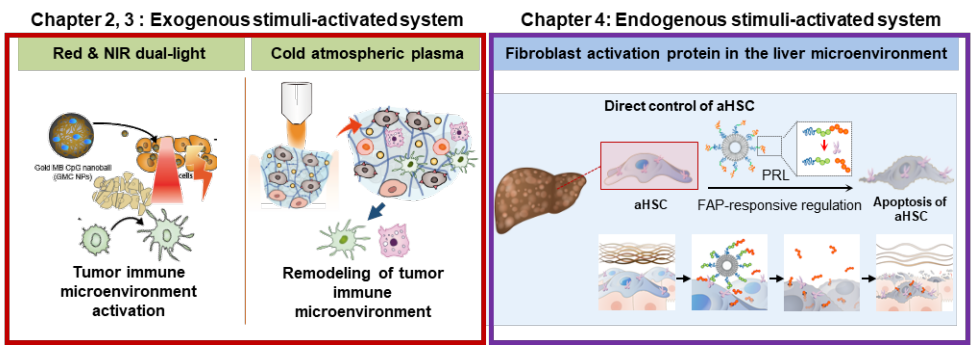

Figure 2. Scope of the studies

In chapter II, dual light-responsive nanomaterial was investigated for cancer therapy. Following dual light irradiation (660 nm/808 nm), it can eradicate the local tumor region and boost the anti-tumor immune microenvironment followed by the prevention of rechallenged tumors. The photosensitizer-trapped gold nanocluster was formulated by utilizing methylene blue as a model photosensitizer, gold nanocluster as a model photothermal agent, and polymerized DNA with CpG sequence as the backbone of the nanocluster. This dual light-responsive nanosystem could function as an effective phototherapeutic for the treatment of cancer disease as well as the activation of immune cells.

In chapter III, the cold atmospheric plasma-responsive on-site hydrogel was developed to reconstruct the tumor immune microenvironment. Cold atmospheric plasma irradiation can generate reactive oxygen species and trigger the presentation of tumor-associated antigens. To maximize the antigen-specific immune reaction, hyaluronic acid-tyramine conjugate with transforming growth factor β-blocking neoadjuvant was intratumorally injected. After cold atmospheric plasma irradiation, a micro-network of TLN-loaded hydrogel was yielded. Immune cells including dendritic cells and T cells could infiltrate the micro-network and be reprogrammed to anti-tumor phenotype.

Lastly, in chapter IV, fibrosis activated protein responsive peptide releasing system was formulated to deliver the anti-fibrotic peptide to activated hepatic stellate cells. The promelittin peptide was conjugated to PEGylated liposomes, resulting in site-specific liberation of melittin to activated hepatic stellate cells. In three types of liver fibrosis models, intravenously administered nanoparticles significantly reduced fibrotic regions and the activated hepatic stellate cell population in the microenvironment.

4. References

[1] Chu C, Artis D, Chiu IM. Neuro-immune Interactions in the Tissues. Immunity. 2020 Mar 17;52(3):464-474.

[2] Quail DF, Dannenberg AJ. The obese adipose tissue microenvironment in cancer development and progression. Nat Rev Endocrinol. 2019 Mar;15(3):139-154.

[3] Zhao L, Liu Y, Zhang S, Wei L, Cheng H, Wang J, Wang J. Impacts and mechanisms of metabolic reprogramming of tumor microenvironment for immunotherapy in gastric cancer. Cell Death Dis. 2022 Apr 20;13(4):378.

[4] McLaughlin M, Patin EC, Pedersen M, Wilkins A, Dillon MT, Melcher AA, Harrington KJ. Inflammatory microenvironment remodelling by tumour cells after radiotherapy. Nat Rev Cancer. 2020 Apr;20(4):203-217.

[5] Koda Y, Teratani T, Chu PS, Hagihara Y, Mikami Y, Harada Y, Tsujikawa H, Miyamoto K, Suzuki T, Taniki N, Sujino T, Sakamoto M, Kanai T, Nakamoto N. CD8+ tissue-resident memory T cells promote liver fibrosis resolution by inducing apoptosis of hepatic stellate cells. Nat Commun. 2021 Jul 22;12(1):4474.

[6] Mascharak S, desJardins-Park HE, Longaker MT. Fibroblast Heterogeneity in Wound Healing: Hurdles to Clinical Translation. Trends Mol Med. 2020 Dec;26(12):1101-1106.

[7] Carlino MS, Larkin J, Long GV. Immune checkpoint inhibitors in melanoma. Lancet. 2021 Sep 11;398(10304):1002-1014.

[8] Alexanian M, Przytycki PF, Micheletti R, Padmanabhan A, Ye L, Travers JG, Gonzalez-Teran B, Silva AC, Duan Q, Ranade SS, Felix F, Linares-Saldana R, Li L, Lee CY, Sadagopan N, Pelonero A, Huang Y, Andreoletti G, Jain R, McKinsey TA, Rosenfeld MG, Gifford CA, Pollard KS, Haldar SM, Srivastava D. A transcriptional switch governs fibroblast activation in heart disease. Nature. 2021 Jul;595(7867):438-443.

[9] Binnewies M, Roberts EW, Kersten K, Chan V, Fearon DF, Merad M, Coussens LM, Gabrilovich DI, Ostrand-Rosenberg S, Hedrick CC, Vonderheide RH, Pittet MJ, Jain RK, Zou W, Howcroft TK, Woodhouse EC, Weinberg RA, Krummel MF. Understanding the tumor immune microenvironment (TIME) for effective therapy. Nat Med. 2018 May;24(5):541-550.

[10] Lotfinejad P, Kazemi T, Mokhtarzadeh A, Shanehbandi D, Jadidi Niaragh F, Safaei S, Asadi M, Baradaran B. PD-1/PD-L1 axis importance and tumor microenvironment immune cells. Life Sci. 2020 Oct 15;259:118297

[11] Bu X, Mahoney KM, Freeman GJ. Learning from PD-1 Resistance: New Combination Strategies. Trends Mol Med. 2016 Jun;22(6):448-451.

[12] DeVito NC, Plebanek MP, Theivanthiran B, Hanks BA. Role of Tumor-Mediated Dendritic Cell Tolerization in Immune Evasion. Front Immunol. 2019 Dec 10;10:2876.

[13] Mao X, Xu J, Wang W, Liang C, Hua J, Liu J, Zhang B, Meng Q, Yu X, Shi S. Crosstalk between cancer-associated fibroblasts and immune cells in the tumor microenvironment: new findings and future perspectives. Mol Cancer. 2021 Oct 11;20(1):131.

[14] Duan Z, Luo Y. Targeting macrophages in cancer immunotherapy. Signal Transduct Target Ther. 2021 Mar 26;6(1):127.

[15] Petrova V, Annicchiarico-Petruzzelli M, Melino G, Amelio I. The hypoxic

tumour microenvironment. Oncogenesis. 2018 Jan 24;7(1):10.
[16] Boussadia Z, Gambardella AR, Mattei F, Parolini I. Acidic and Hypoxic Microenvironment in Melanoma: Impact of Tumour Exosomes on Disease Progression. Cells. 2021 Nov 25;10(12):3311.
[17] Jing X, Yang F, Shao C, Wei K, Xie M, Shen H, Shu Y. Role of hypoxia in cancer therapy by regulating the tumor microenvironment. Mol Cancer. 2019 Nov 11;18(1):157.
[18] Mouchemore KA, Anderson RL, Hamilton JA. Neutrophils, G-CSF and their contribution to breast cancer metastasis. FEBS J. 2018 Feb;285(4):665-679.
[19] Barry-Hamilton V, Spangler R, Marshall D, McCauley S, Rodriguez HM, Oyasu M, Mikels A, Vaysberg M, Ghermazien H, Wai C, Garcia CA, Velayo AC, Jorgensen B, Biermann D, Tsai D, Green J, Zaffryar-Eilot S, Holzer A, Ogg S, Thai D, Neufeld G, Van Vlasselaer P, Smith V. Allosteric inhibition of lysyl oxidase-like-2 impedes the development of a pathologic microenvironment. Nat Med. 2010 Sep;16(9):1009-17.
[20] Long Y, Niu Y, Liang K, Du Y. Mechanical communication in fibrosis progression. Trends Cell Biol. 2022 Jan;32(1):70-90.
[21] van Buuren N, Ramirez R, Turner S, Chen D, Suri V, Aggarwal A, Moon C, Kim S, Kornyeyev D, Bui N, Bhardwaj N, Chan HL, Marcellin P, Buti M, Wallin J, Gaggar A, Fletcher SP, Diehl L, Li L, Mo H, Feierbach B. Characterization of the liver immune microenvironment in liver biopsies from patients with chronic HBV infection. JHEP Rep. 2021 Oct 24;4(1):100388.
[22] Liu Y, Dong Y, Wu X, Wang X, Niu J. Identification of Immune Microenvironment Changes and the Expression of Immune-Related Genes in Liver Cirrhosis. Front Immunol. 2022 Jul 12;13:918445.
[23] Liu C, Zhao Z, Gao R, Zhang X, Sun Y, Wu J, Liu J, Chen C. Matrix Metalloproteinase-2-Responsive Surface-Changeable Liposomes Decorated by Multifunctional Peptides to Overcome the Drug Resistance of Triple-Negative Breast Cancer through Enhanced Targeting and Penetrability. ACS Biomater Sci Eng. 2022 Jul 11;8(7):2979-2994.
[24] Jiang Y, Chen P, Hu K, Dai G, Li J, Zheng D, Yuan H, He L, Xie P, Tu M, Peng S, Qu C, Lin W, Chung RT, Hong J. Inflammatory microenvironment of fibrotic liver promotes hepatocellular carcinoma growth, metastasis and sorafenib resistance through STAT3 activation. J Cell Mol Med. 2021 Feb;25(3):1568-1582.
[25] Tsukasaki M, Takayanagi H. Osteoimmunology: evolving concepts in bone-immune interactions in health and disease. Nat Rev Immunol. 2019 Oct;19(10):626-642.
[26] Dominguez-Villar M, Hafler DA. Regulatory T cells in autoimmune disease. Nat Immunol. 2018 Jul;19(7):665-673.
[27] Ye CH, Hsu WL, Peng GR, Yu WC, Lin WC, Hu S, Yu SH. Role of the Immune Microenvironment in SARS-CoV-2 Infection. Cell Transplant. 2021 Jan-Dec;30:9636897211010632.
[28] Sefik E, Qu R, Junqueira C, Kaffe E, Mirza H, Zhao J, Brewer JR, Han A, Steach HR, Israelow B, Blackburn HN, Velazquez SE, Chen YG, Halene S, Iwasaki A, Meffre E, Nussenzweig M, Lieberman J, Wilen CB, Kluger Y, Flavell RA. Inflammasome activation in infected macrophages drives

COVID-19 pathology. Nature. 2022 Jun;606(7914):585-593.
[29] Barkley D, Moncada R, Pour M, Liberman DA, Dryg I, Werba G, Wang W, Baron M, Rao A, Xia B, França GS, Weil A, Delair DF, Hajdu C, Lund AW, Osman I, Yanai I. Cancer cell states recur across tumor types and form specific interactions with the tumor microenvironment. Nat Genet. 2022 Aug;54(8):1192-1201.
[30] Ren X, Zhang L, Zhang Y, Li Z, Siemers N, Zhang Z. Insights Gained from Single-Cell Analysis of Immune Cells in the Tumor Microenvironment. Annu Rev Immunol. 2021 Apr 26;39:583-609.
[31] Chen Y, McAndrews KM, Kalluri R. Clinical and therapeutic relevance of cancer-associated fibroblasts. Nat Rev Clin Oncol. 2021 Dec;18(12):792-804.
[32] Wculek SK, Cueto FJ, Mujal AM, Melero I, Krummel MF, Sancho D. Dendritic cells in cancer immunology and immunotherapy. Nat Rev Immunol. 2020 Jan;20(1):7-24.
[33] Tang T, Huang X, Zhang G, Hong Z, Bai X, Liang T. Advantages of targeting the tumor immune microenvironment over blocking immune checkpoint in cancer immunotherapy. Signal Transduct Target Ther. 2021 Feb 20;6(1):72.
[34] Raskov H, Orhan A, Christensen JP, Gögenur I. Cytotoxic CD8+ T cells in cancer and cancer immunotherapy. Br J Cancer. 2021 Jan;124(2):359-367.
[35] Murciano-Goroff YR, Warner AB, Wolchok JD. The future of cancer immunotherapy: microenvironment-targeting combinations. Cell Res. 2020 Jun;30(6):507-519.
[36] Kisseleva T, Brenner D. Molecular and cellular mechanisms of liver fibrosis and its regression. Nat Rev Gastroenterol Hepatol. 2021 Mar;18(3):151-166.
[37] Cheng D, Chai J, Wang H, Fu L, Peng S, Ni X. Hepatic macrophages: Key players in the development and progression of liver fibrosis. Liver Int. 2021 Oct;41(10):2279-2294.
[38] Zhang M, Zhang S. T Cells in Fibrosis and Fibrotic Diseases. Front Immunol. 2020 Jun 26;11:1142.
[39] Wynn TA, Ramalingam TR. Mechanisms of fibrosis: therapeutic translation for fibrotic disease. Nat Med. 2012 Jul 6;18(7):1028-40.
[40] Tzahor E, Dimmeler S. A coalition to heal-the impact of the cardiac microenvironment. Science. 2022 Sep 2;377(6610):eabm4443.
[41] Ceccato TL, Starbuck RB, Hall JK, Walker CJ, Brown TE, Killgore JP, Anseth KS, Leinwand LA. Defining the Cardiac Fibroblast Secretome in a Fibrotic Microenvironment. J Am Heart Assoc. 2020 Oct 20;9(19):e017025.
[42] Rurik JG, Tombácz I, Yadegari A, Méndez Fernández PO, Shewale SV, Li L, Kimura T, Soliman OY, Papp TE, Tam YK, Mui BL, Albelda SM, Puré E, June CH, Aghajanian H, Weissman D, Parhiz H, Epstein JA. CAR T cells produced in vivo to treat cardiac injury. Science. 2022 Jan 7;375(6576):91-96.
[43] Lee J, Byun J, Shim G, Oh YK. Fibroblast activation protein activated antifibrotic peptide delivery attenuates fibrosis in mouse models of liver fibrosis. Nat Commun. 2022 Mar 21;13(1):1516.
[44] Aran D, Looney AP, Liu L, Wu E, Fong V, Hsu A, Chak S, Naikawadi RP, Wolters PJ, Abate AR, Butte AJ, Bhattacharya M. Reference-based analysis

of lung single-cell sequencing reveals a transitional profibrotic macrophage. Nat Immunol. 2019 Feb;20(2):163-172.

[45] Higashi T, Friedman SL, Hoshida Y. Hepatic stellate cells as key target in liver fibrosis. Adv Drug Deliv Rev. 2017 Nov 1;121:27-42.

[46] Tsuchida T, Friedman SL. Mechanisms of hepatic stellate cell activation. Nat Rev Gastroenterol Hepatol. 2017 Jul;14(7):397-411.

[47] Yin J, Hou S, Wang Q, Bao L, Liu D, Yue Y, Yao W, Gao X. Microenvironment-Responsive Delivery of the Cas9 RNA-Guided Endonuclease for Efficient Genome Editing. Bioconjug Chem. 2019 Mar 20;30(3):898-906.

[48] Li Y, Lin J, Wang P, Luo Q, Zhu F, Zhang Y, Hou Z, Liu X, Liu J. Tumor Microenvironment Cascade-Responsive Nanodrug with Self-Targeting Activation and ROS Regeneration for Synergistic Oxidation-Chemotherapy. Nanomicro Lett. 2020 Sep 14;12(1):182.

[49] De Rycker M, Baragaña B, Duce SL, Gilbert IH. Challenges and recent progress in drug discovery for tropical diseases. Nature. 2018 Jul;559(7715):498-506.

[50] Manzari MT, Shamay Y, Kiguchi H, Rosen N, Scaltriti M, Heller DA. Targeted drug delivery strategies for precision medicines. Nat Rev Mater. 2021 Apr;6(4):351-370.

[51] Ekins S, Puhl AC, Zorn KM, Lane TR, Russo DP, Klein JJ, Hickey AJ, Clark AM. Exploiting machine learning for end-to-end drug discovery and development. Nat Mater. 2019 May;18(5):435-441.

[52] Ma C, Peng Y, Li H, Chen W. Organ-on-a-Chip: A New Paradigm for Drug Development. Trends Pharmacol Sci. 2021 Feb;42(2):119-133.

[53] Devine PN, Howard RM, Kumar R, Thompson MP, Truppo MD, Turner NJ. Extending the application of biocatalysis to meet the challenges of drug development. Nature Reviews Chemistry. 2018;2(12):409-21.

[54] Rosenblum D, Joshi N, Tao W, Karp JM, Peer D. Progress and challenges towards targeted delivery of cancer therapeutics. Nat Commun. 2018 Apr 12;9(1):1410.

[55] Zhang Y, Li N, Suh H, Irvine DJ. Nanoparticle anchoring targets immune agonists to tumors enabling anti-cancer immunity without systemic toxicity. Nat Commun. 2018 Jan 2;9(1):6.

[56] Kang M, Lee SH, Kwon M, Byun J, Kim D, Kim C, Koo S, Kwon SP, Moon S, Jung M, Hong J, Go S, Song SY, Choi JH, Hyeon T, Oh YK, Park HH, Kim BS. Nanocomplex-Mediated In Vivo Programming to Chimeric Antigen Receptor-M1 Macrophages for Cancer Therapy. Adv Mater. 2021 Oct;33(43):e2103258.

[57] Rurik JG, Tombácz I, Yadegari A, Méndez Fernández PO, Shewale SV, Li L, Kimura T, Soliman OY, Papp TE, Tam YK, Mui BL, Albelda SM, Puré E, June CH, Aghajanian H, Weissman D, Parhiz H, Epstein JA. CAR T cells produced in vivo to treat cardiac injury. Science. 2022 Jan 7;375(6576):91-96.

[58] Kim D, Byun J, Park J, Lee Y, Shim G, Oh YK. Biomimetic polymeric nanoparticle-based photodynamic immunotherapy and protection against tumor rechallenge. Biomater Sci. 2020 Feb 21;8(4):1106-1116.

[59] Le QV, Kim D, Lee J, Shim G, Oh YK. Photosensitizer-Free Phototherapy with Peptide Micelle Nanoadjuvants for Cancer Vaccine against Metastasis

of Melanoma. Adv Ther-Germany. 2021;4(8).

[60] Le QV, Suh J, Choi JJ, Park GT, Lee JW, Shim G, et al. In Situ Nanoadjuvant-Assembled Tumor Vaccine for Preventing Long-Term Recurrence. Acs Nano. 2019;13(7):7442-62.Wu Y, Li Q, Shim G, Oh YK. Melanin-loaded CpG DNA hydrogel for modulation of tumor immune microenvironment. J Control Release 330, 540-553 (2021).

[61] Kim D, Wu Y, Shim G, Oh YK. Genome-Editing-Mediated Restructuring of Tumor Immune Microenvironment for Prevention of Metastasis. Acs Nano. 2021;15(11):17635-56.

[62] Chen G, Chen Z, Wen D, Wang Z, Li H, Zeng Y, Dotti G, Wirz RE, Gu Z. Transdermal cold atmospheric plasma-mediated immune checkpoint blockade therapy. Proc Natl Acad Sci U S A. 2020 Feb 18;117(7):3687-3692.

[63] Laroussi M. Cold Plasma in Medicine and Healthcare: The New Frontier in Low Temperature Plasma Applications. Front Phys-Lausanne. 2020;8.

[64] Chen ZT, Chen GJ, Obenchain R, Zhang R, Bai F, Fang TX, et al. Cold atmospheric plasma delivery for biomedical applications. Mater Today. 2022;54:153-88.

[65] Tan C, Fan H, Ding J, Han C, Guan Y, Zhu F, Wu H, Liu Y, Zhang W, Hou X, Tan S, Tang Q. ROS-responsive nanoparticles for oral delivery of luteolin and targeted therapy of ulcerative colitis by regulating pathological microenvironment. Mater Today Bio. 2022 Mar 23;14:100246.

Chapter II

Photosensitizer-trapped gold nanocluster for dual light-responsive phototherapy

1. Introduction

External stimulus-responsive systems are being proposed as a new alternative modality in the field of cancer-targeted therapy [1,2]. Photo-responsive agents have been particularly studied to achieve complete tumor ablation through photothermal [3,4] or photodynamic [2,5] effects, which generate heat or reactive oxygen species (ROS), respectively, upon light irradiation. Photothermal treatment using near-infrared (NIR) light has various advantages over conventional anti-cancer therapy [3,6]. For example, phototherapy facilitates minimally invasive treatment by irradiating light to the diseased area, and thereby prevents systemic toxicity. Moreover, photothermal therapy-mediated hyperthermic cell death provides a molecular switch that can trigger cell death without the limitations of chemotherapy, such as severe side effects and drug resistance.

However, there are a few remaining concerns surrounding the use of photoresponsive materials as a new therapeutic. For example, in vivo fate of photoresponsive materials is important issue because it can produce effective therapeutic effects through light irradiation to the target area under optimal conditions. Modification of the photo-responsive materials—gold [7], carbon [8], and polymers [9]—has been intensively studied as a means to track the in vivo behavior of nanomaterials for theranostic purposes. However, the above-listed photoresponsive materials suffer from the quenching of fluorescence when the fluorescent probe interacts with the hydrophobic surface of the nanoparticles, and it is a cumbersome process to insert a spacer or a cleavable linker molecule to prevent this phenomenon. In addition, since tumor recurrence is often observed in an irradiated lesion after phototherapy, the phototherapeutic efficacy needs to be improved to ensure complete eradication of tumor tissues. [10]. In terms of clinical development, some photoresponsive materials have limitations due to toxicity, safety issues, and/or unverified excretion profiles [11,12].

In this study, we designed a dual light-responsive DNA-based nanocluster to achieve an effective image-guided dual phototherapy that is capable of dual photothermal and photodynamic therapy for theranostic purposes (Fig. 1). We selected methylene blue (MB) as a model photosensitizer and gold (iii) ion as the seed material for the photothermal nanocluster. We synthesized a polymerized DNA fiber via rolling circle amplification (RCA); this fiber serves multiple functions, acting as a safe and biodegradable backbone, a delivery carrier of MB, and a template for the gold nanocluster. MB is a well-known photosensitizer and clinically used for the treatment of methemoglobinemia with US Food and Drug Administration approval (Provayblue®) [13]. Several studies reported the applications of MB for photodynamic anticancer therapy [14-16]. Equipped with the DNA intercalating ability, MB was loaded in DNA nanostructures [14,15]. With the light-to-heat conversion feature, gold in nanomaterials was studied for photothermal therapy [17-19]. Photothermal gold nanomaterials have been

investigated in various shapes of nanosphere, nanoshell, nanorod, and nanocluster. The application of gold nanoshells for phototherapy of prostate tumors is in a clinical trial [20]. Taken together, the clinical reports of MB and gold nanomaterials suggest the potential of MB and gold nanocluster for translational studies. MB-trapped gold DNA nanoclusters (GMDN) were generated by reducing gold ions with MB-intercalated long DNA as a cluster template (Fig. 2A). GMDN yielded acceptable tumor ablation efficacy due to the response to dual light (660 nm for MB, 808 nm for gold) irradiation. Moreover, the in vivo behavior of GMDN can be traced by monitoring the entrapped MB, which has long wavelength-excitable fluorescence. Here, we report that GMDN can exert phototherapeutic effects via combined photodynamic and photothermal therapy. Moreover, GMDNs allow image-guided phototherapy, and thus show potential as a theranostic nanoplatform.

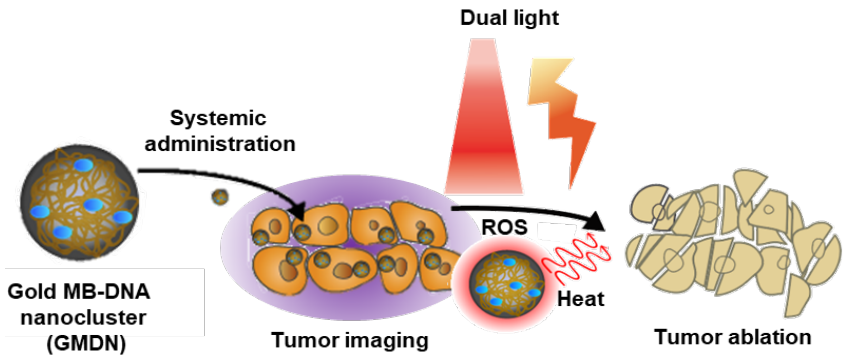

Figure 1. Schematic illustration. For synergistic dual phototherapy, methylene blue (MB) was trapped in gold DNA nanoclusters to form MB-trapped gold DNA nanoclusters (GMDN). After systemic administration, tumor accumulation of GMDN was monitored by molecular imaging. Then, dual light irradiation (660 nm and 808 nm) was applied to induce photodynamic and photothermal therapy for tumor ablation.

2. Materials and methods

Preparation of GMDN

GMDNs were prepared by clustering, which occurred when Au3+ ions were reduced with MB-intercalated DNA. An oligo primer (5′ -TATATACTAGTCAGATATTACT-3′) and a linear DNA sequence (5′ -ATCTGACTAGTATATAAACGTCAGGAACGTCATGGAAACGTCAGG AACGTCATGGAAGTAAT-3′) were used to produce polymerized CpG DNA (PD) as previously reported [16]. The linear DNA template was annealed with the primer (Macrogen Inc., Daejeon, Republic of Korea) in hybridization buffer (10 mM Tris−HCl, 1 mM EDTA, 100 mM NaCl, pH 8.0), and then incubated with T4 DNA ligase (125 units/mL; Thermo Fisher Scientific, Inc.), Waltham, MA, USA); this ligated any nicks in the hybridized DNA complex to generate a circular template. Inactivation of T4 DNA ligase was performed at 70 °C for 5 min. This was followed by DNA amplification, which was performed using phi29 DNA polymerase (100 units/mL; Thermo Fisher Scientific, Inc.) and 2 mM of dNTPs (ELPIS Biotech, Inc., Daejeon, Republic of Korea) for 24 h at 30 °C. Free dNTPs were removed by centrifugation at 11,000× g for 3 min, and the resulting PD was resuspended in triple-distilled water (TDW). MB was intercalated to PD by incubating 25 μL of PD (10 μg) with 75 μL of MB (100 μM) for 5 min. The resulting MB-intercalated PD (MB-PD) was purified by centrifugation at 11,000× g for 3 min and resuspended in 180 μL of TDW. To prepare GMDN, 10 μL of HAuCl4·3H2O (50 mM; Sigma-Aldrich, St. Louis, MO, USA) and 10 μL of dimethylamine borane (5 mM, DMAB; Sigma-Aldrich) were added to 180 μL of MB-PD with vigorous mixing. Gold DNA nanoclusters (GDN) were prepared under the same conditions but without loading of MB. For further experiments, various groups were prepared in aqueous 5% glucose solution.

Characterization of GMDN

The physicochemical properties of various nanoclusters were evaluated in terms of their size distribution, morphology, electron mapping, absorbance, cargo-loading efficiency, and photo-responsivity. To evaluate morphology and perform electronic mapping of phosphorus and sulfur, nanoparticles were observed by energy dispersive X-ray spectroscopy-scanning transmission electron microscopy (EDS-STEM) using a JEM-2100 F transmission electron microscope (TEM; JEOL Ltd., Tokyo, Japan). To measure the particle size distribution, dynamic light scattering was applied with an ELSZ-1000 instrument (Otsuka Electronics Co., Osaka, Japan). The zeta potential was measured by laser Doppler micro electrophoresis at an angle of 22° with an ELSZ-1000 instrument (Otsuka Electronics). The UV/Vis spectra of RCA products were obtained using a SpectraMAX M5 (Molecular Devices Corp., Sunnyvale, CA, USA) from 400 nm to 750 nm. The contents of gold and MB were quantified by inductively coupled plasma mass spectrometry (ICP-MS) and UV-Vis absorbance spectrum analysis, respectively. The loading amount

of Au3+ was analyzed with ICP-MS using a Varian 820-MS system (Varian, Sydney, Australia). The MB contents in the various groups were quantified with an emission peak at 686 nm (λex 665 nm) by fluorescence measurement using a SpectraMAX M5 (Molecular Devices). The temperature elevation of GMDN was evaluated using an infrared thermal camera (FLIR T420; FLIR System Inc., Danderyd, Sweden) upon 808 nm irradiation by a NIR laser (BWT Beijing Ltd., Beijing, China) at 1.5 W power.

Cellular Uptake

Cellular uptake of nanoclusters was determined by optical imaging of the cell pellets, UV-Vis spectra, cellular TEM imaging, and cellular fluorescence imaging. Murine colon carcinoma CT26 cells (American Type Culture Collection (ATCC), Manassas, VA, USA) were seeded to a 24-well plate at a density of 5 × 104 cells per well and incubated for 12 h. The cells were treated with the various formulations at a PD concentration of 40 μg/mL. After 4 h incubation, cells were harvested and centrifuged at 100× g for 3 min. The cell pellet color was visualized by optical imaging. The cell pellet was resuspended with 200 μL of 5% glucose solution, and the absorbance of cell suspension was measured at 600 nm using a SpectraMAX M5 (Molecular Devices). The localization of nanoclusters within tumor cells was visualized by TEM (Talos L120C; Thermo Fisher Scientific, Inc.). To prepare the cell samples for TEM imaging, cell pellets were fixed with Karnovsky's fixative for 2 h at 4 °C and then washed with cold sodium cacodylate buffer (0.05 M). The cell pellets were treated with 1% osmium tetroxide solution, and then subjected to negative staining with 0.5% uranyl acetate. After dehydration by a series ethanol gradient, the cell pellets were transferred to propylene oxide and embedded in Spurr's resin as previously reported [3]. Thin sections (60 nm) of embedded cell pellets were cut by a microtome and observed by TEM.

Intracellular ROS Generation

The intracellular ROS level of nanocluster-treated and light-irradiated cells was measured by 2 ,7′ -dichlorodihydrofluorescein diacetate (H2DCFDA) staining. CT26 cells were seeded to a 24-well plate at a density of 5 × 104 cells per well and incubated for 12 h. The various formulations were applied to the wells at a PD concentration of 40 μg/mL. After 4 h, cells were washed with phosphate-buffered saline (PBS) and irradiated with a 660-nm light emitting diode (LED; Mikwang Electronics, Busan, Republic of Korea) at an intensity of 8000 mCd for 30 min. To detect intracellular ROS formation, cells were incubated with 10 μM of H2DCFDA (Thermo Fisher Scientific, Inc.) in serum-free RPMI at 37 °C for 15 min. After the cells were washed with PBS, and the fluorescence intensity was visualized with a Leica TCS SP8 confocal microscope (Leica Microsystems, Wetzlar, Germany) and quantified by flow cytometry (FACS Lyric; BD Biosciences, San Jose, CA, USA).

In Vitro Photoresponsive Anti-Cancer Efficacy

The in vitro therapeutic effect of GMDN plus dual irradiation was evaluated by cell viability test and live and dead cell staining. CT26 cells were seeded to a 24-well plate at a density of 5 × 104 cells per well and incubated for 12 h. The various formulations were applied to the wells at a PD concentration of 40 μg/mL. After 4 h, cells were washed with phosphate-buffered saline (PBS) and irradiated with a 660-nm LED or 808-nm laser. After 20 h, cell viability was quantified by 3-(4,5-dimethylthizol-2-yl)-2,5-diphenyltetrazolium bromide (MTT) assay. The cells were incubated with MTT (250 μg/mL)-containing culture medium at 37 °C for 2 h and washed with PBS. The intracellular formazan was dissolved in dimethyl sulfoxide and absorbance was measured at 570 nm. Live and dead cell staining (Thermo Fisher Scientific, Inc.) was performed to visualize the cell killing effect by dual irradiation, as previously described [3]. The cells were stained with calcein acetoxymethyl (2 μg/mL) and propidium iodide (3 μg/mL) at 37 °C for 20 min and observed by fluorescence microscopy (Leica DM IL LED; Leica Microsystems).

Animal Experiments

Five-week-old female BALB/c mice (Raon Bio, Yongin-si, Republic of Korea) were used for in vivo experiments. All animal experiments were performed in accordance with the Guidelines for the Care and Use of Laboratory Animals of the Institute of Laboratory Animal Resources. The study protocol (#SNU-190821-5, 21/08/2019, Seoul National University Institutional Animal Care and Use Committee) was approved by the Institutional Review Board for the use of animals at the College of Pharmacy, Seoul National University.

In Vivo Biodistribution

The in vivo distribution of GMDN was evaluated by molecular imaging of the fluorescence of MB. CT26-bearing BALB/c mice were established by subcutaneous inoculation of 1 × 106 CT26 cells. On day 7 after CT26 inoculation, tumor-bearing mice were intravenously injected with free MB or GMDN at an MB dose of 1.14 mg/kg. In vivo fluorescence images of the mice were collected at 1 h, 6 h, and 24 h after the administration of GMDN using an IVIS Spectrum in Vivo Imaging System (PerkinElmer, Inc., Waltham, MA, USA).

In Vivo Anticancer Effect

The in vivo therapeutic effect of systemically injected GMDN was tested in CT26 tumor-bearing model mice exposed to dual light irradiation. To establish the tumor model, 6-week-old female BALB/c mice were subcutaneously inoculated with 1 × 106 CT26 tumor cells in the right flank. On day 7 after inoculation, the various formulations were administered intravenously at a PD dose of 5 mg/kg. At 24 h post-injection, the tumors

were irradiated with a 660 nm LED (8000 mCd) and an 808 nm laser (1.5 W/cm2) for 5 min each. The temperature of the tumor region was monitored during NIR irradiation using an infrared thermal camera (FLIR T420). The volume of tumors was measured by calipers and calculated as previously reported according to the formula: (Length) × (Width)2 × 0.5 [4].

Ex Vivo Killing Effect of T Cells after GMDN Treatment

To assessment of adaptive immune response, tumor cell killing effect of T cells was monitored. GMDN-treated and dual light irradiated mice were sacrificed at 7 days after the treatment and T cells were isolated from the spleen by nylon wool fiber column method as previously reported [3]. Isolated T cells were stained with CellTracker Green CMTPX dye (Thermo Fisher Scientific, Inc.) and CT26 tumor cells were labeled by CellTracker Red CMTPX dye (Thermo Fisher Scientific, Inc.). T cells and CT26 cells were co-cultured at a ratio of 100:1 and a real-time video was recorded using an Operetta High-Content Imaging System (PerkinElmer, Inc.).

Statistical Analysis

Statistical analysis and visualization of experimental data were performed with a one-way analysis of variance (ANOVA) with Student-Newman-Keuls post-hoc test using GraphPad Prism 7 (GraphPad Software Inc., San Diego, CA, USA). A p-value less than 0.05 was considered statistically significant.

3. Results

Characterization of GMDN

The GMDN were characterized for their morphological, physicochemical, and photoresponsive characteristics. Elemental mapping showed that Au, phosphorous, and sulfur co-localized in the nanoclusters, indicating the presence of gold nanoclusters, DNA, and MB, respectively (Fig. 2B). The average size of GMDN was 51.7 ± 7.7 nm (Fig. 2C). GMDN showed a higher zeta-potential (−28.2 ± 0.6 mV) than PD (−48.2 ± 0.3 mV). The amount of encapsulated Au was similar in GMDN and GDN (Fig. 2D), at 129.8 ± 11.7 and 105.7 ± 37.3 ng/μg DNA, respectively. The amount of MB in GMDN was 228.0 ± 0.1 ng/ μg DNA, which was not significantly different from that in PD (Fig. 2E). The formation of gold clusters was characterized by analysis of the absorbance spectrum (Fig. 2F). Whereas PD and MB-PD did not exhibit any significant absorption peak, GMDN revealed remarkable absorbance at 500–700 nm. Due to the loading of Au, the particle had a photothermal effect (Fig. 2G). While TDW, PD, and MB-PD did not exhibit any temperature change upon NIR laser irradiation, the temperatures of GDN and GMDN increased from room temperature to 68.6 ± 1.7 and 65.3 ± 2.1 °C, respectively, at 3 min after NIR irradiation.

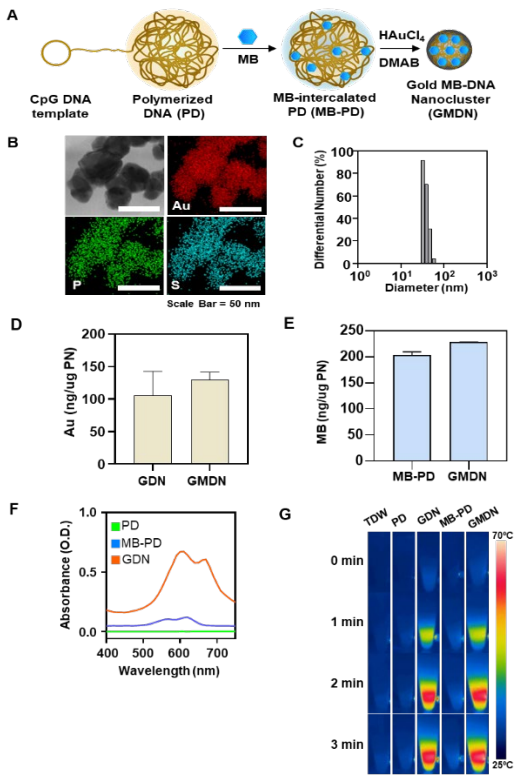

Figure 2. Characterization of nanoclusters. (A) Schematic illustrations of GMDN preparation. (B) Elemental mapping images obtained by energy dispersive X-ray spectroscopy-scanning transmission electron microscopy (EDS-STEM) for gold, phosphorous, and sulfur. Scale bar: 50 nm. (C) Size distribution of GMDN. (D) Au contents of gold DNA nanoclusters (GDN)

and GMDN were evaluated by inductively coupled plasma mass spectrometry (ICP-MS). (E) Loading amounts of methylene blue (MB) in MB-intercalated polymerized CpG DNA (MB-PD) and GMDN were measured by fluorescence spectrometry. (F) Absorbances of polymerized CpG DNA (PD), MB-PD, and GMDN were assessed by UV/Vis spectrometry. (G) Photoresponsive properties of various groups were observed by temperature monitoring during NIR irradiation.

Cellular Uptake of GMDN

The cellular uptake of the gold nanoclusters was observed based on cell color, cellular TEM imaging, and fluorescence microscopy. First, the cellular uptake of GMDN was visualized by the color of the cell pellet (Fig. 3A). The pellets of GDN- and GMDN-treated cells were much darker than those of the other groups, and GDN- and GMDN-treated cells had much higher absorbances than the other groups (Fig. 3B). Gold nanoclusters were observed in the cytoplasm of GDN- and GMDN-treated cells (Fig. 3C). The cellular uptake of GMDN was also evaluated by assessing the fluorescence of MB. PD- and GDN-treated cells did not exhibit any fluorescence, whereas the MB-PD- and GMDN-treated groups showed strong fluorescence, indicating cellular uptake of MB. Cells treated with GMDN showed a higher uptake rate compared to those treated with MB-PD, as assessed by examining the fluorescence of methylene blue by FACS analysis (Fig. 3E). The nanosized clusters of GMDN had 2.0-fold higher fluorescence than the microsized structures of MB-PD (Fig. 3F).

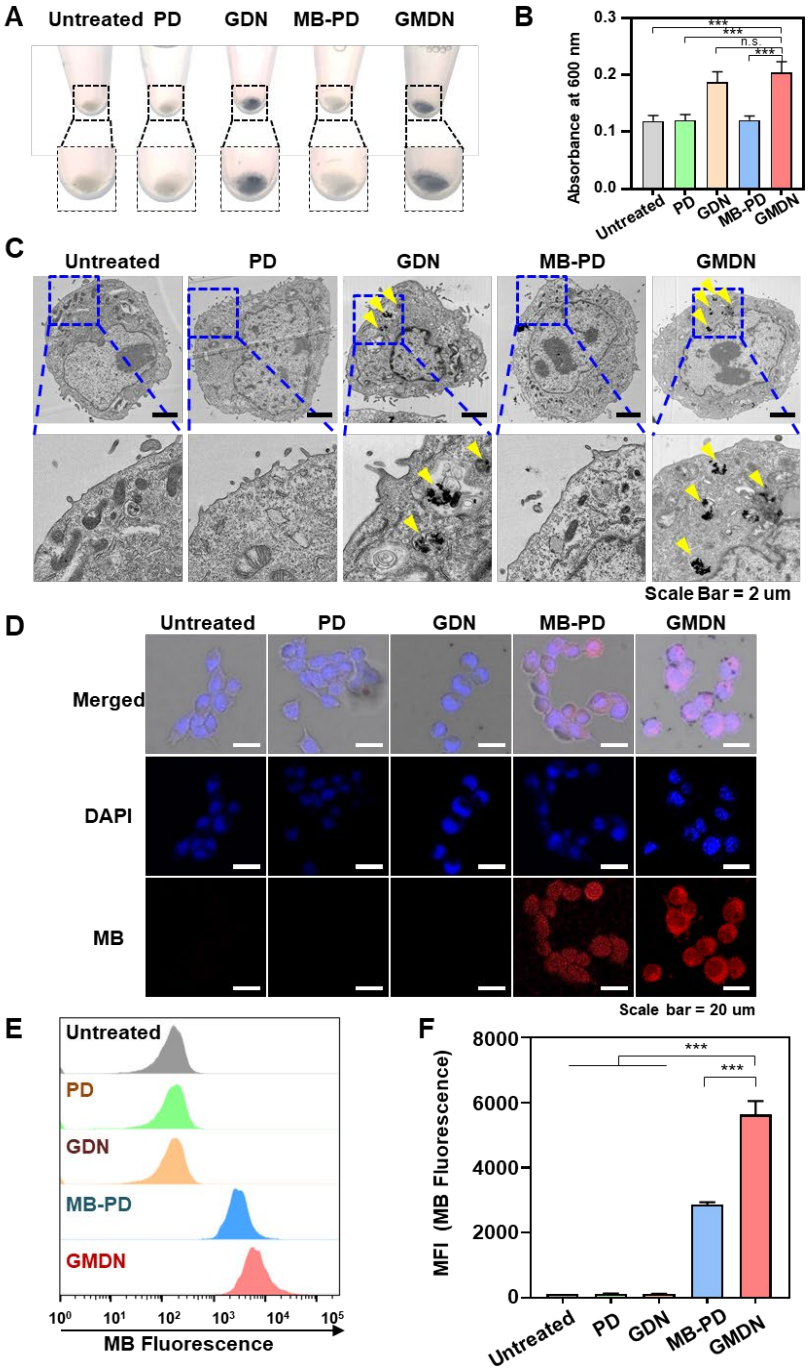

Figure 3. Cellular uptake of nanoclusters. (A) Cell pellets were observed after cells were treated with PD, GDN, MB-PD, or GMDN. (B) Absorbances of cell suspensions were measured at 600 nm. (C) Cellular internalization of gold nanoclusters was observed by TEM imaging. (D) Cells were treated with the various formulations and fluorescence was observed by confocal microscopy. (E,F) Cellular uptake of nanoclusters was measured by flow

cytometry (E) and analysis of average fluorescence intensity (F) (***$p<0.001$).

In Vitro Phototherapeutic Effects of GMDN

The dual light responsiveness of GMDN resulted in ROS generation and temperature increase, which was able to kill cancer cells. Upon 660-nm irradiation, ROS generation was not detected in control groups treated with PD or GDN (Fig. 4A). However, MB-PD- and GMDN-treated CT26 cells showed robust ROS generation. Photothermal efficacy was observed only in GDN- and GMDN-treated cells (Fig. 4B, 4C). Upon NIR laser irradiation, negligible temperature increases were observed in PD- and MB-PD-treated cells, which lacked Au in the formulation (Fig. 4B). In contrast, significant temperature increases upon NIR irradiation were confirmed in GDN- and GMDN-treated cells, which exhibited increases of up to 47.2 ± 0.5 and 47.1 ± 0.8 °C, respectively (Fig. 4C). The ROS-mediated photodynamic effect and heat-mediated photothermal effect led to synergistic anti-cancer efficacy. Whereas cell viability was not affected by any of the tested formulations in the absence of irradiation (Fig. 4D), ROS generation upon 660-nm irradiation significantly reduced the cell viability of the GMDN group to 40.4% (Fig. 4E). Heat generation upon 808-nm NIR irradiation also induced significant cell death, with the GMDN-treated group showing 43.1% cell viability (Fig. 4F). When both lights were applied to the cells, a synergistic anti-cancer effect was confirmed (Fig. 4G). The GDN and MB-PD groups showed comparable cell viabilities above 40% upon dual light irradiation, whereas GMDN-treated cells showed significantly decreased cell viability under dual light irradiation, down to 5.4 ± 9.1% (Fig. 4G). The results of live and dead cell staining supported this synergistic anti-cancer efficacy by showing significantly lower levels of living cells and higher levels of dead cells when the dual light was applied to GMDN-treated cells compared to the GDN- or MB-PD-treated groups (Fig. 4H).

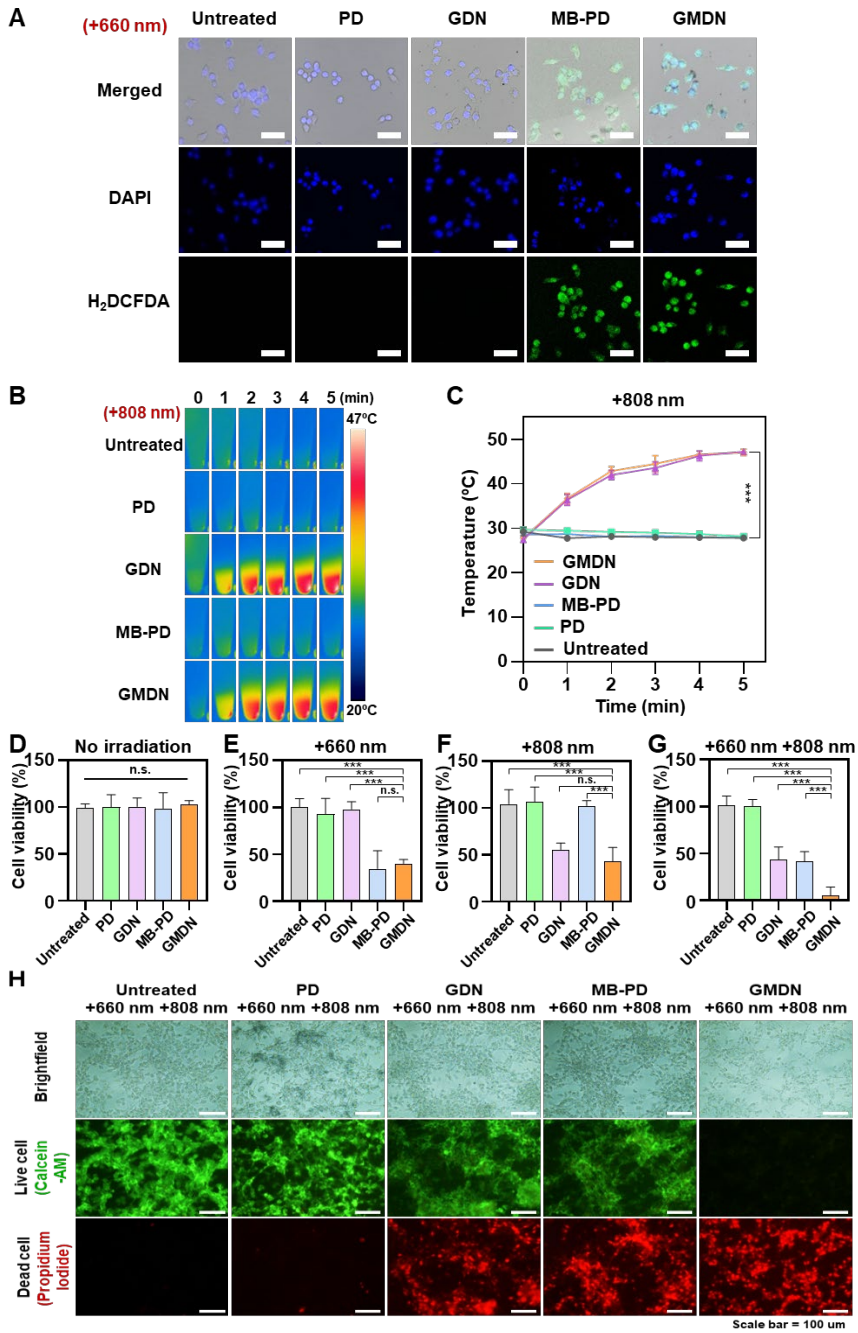

Figure 4. In vitro photodynamic and photothermal effects of GMDN. Various formulations were applied to CT26 cells for 4 h, followed by 660-nm or 808-nm irradiation. (A) ROS generation in the cells was evaluated by H2DCFDA detection upon 660-nm irradiation. (B) Upon 808-nm NIR laser irradiation, heat generation was observed by thermo-imaging. (C) The temperature was monitored during irradiation. (D–G) Anti-cancer efficacy was evaluated by measuring cell viability under no irradiation (D), 660-nm irradiation (E), 808-nm irradiation (F) and dual light irradiation (G). (H) The

anti-cancer efficacy was visualized by live and dead cell imaging (n.s., not significant; ***$p<0.001$).

In Vivo Anti-Tumor Efficacy of GMDN

The in vivo distribution and synergistic dual phototherapeutic effects of GMDN were confirmed in vivo (Fig. 5A). Each formulation was intravenously administered to CT26 tumor-bearing mice. Our results revealed that free MB was distributed throughout the whole body (Fig. 5B). However, the fluorescence signal was significantly increased at the tumor site of the GMDN-treated group, and lower distribution was seen in other organs (e.g., liver) under this treatment. Moreover, the accumulation of GMDN resulted in a temperature increase from room temperature to 47.1 ± 1.7 °C upon 808-nm NIR irradiation at the tumor site (Fig. 5C). When dual light was applied to the tumor, slight suppression of tumor growth was observed in the GDN- and MB-PD-injected groups, which showed average tumor volumes of 902.6 ± 306.9 and 981.3 ± 671.9 mm3, respectively, while the average tumor volume of the untreated group was 3169.1 ± 328.6 mm3 (Fig. 5D, 5E). However, dual light irradiation of the GMDN-treated group significantly inhibited tumor growth even further, yielding an average tumor volume of 140.0 ± 156.1 mm3. As a result, GMDN improved the survival of the mice (Fig. 5F). While no mouse survived to day 61 post tumor inoculation in any other group, GMDN-treated mice showed 100% survival up to day 65 (Fig. 5F). When splenic T cells were extracted from the surviving mice and co-cultured with tumor cells, a more robust anti-cancer response was observed compared to that obtained with naïve splenic T cells from untreated mice (Fig. 5G).

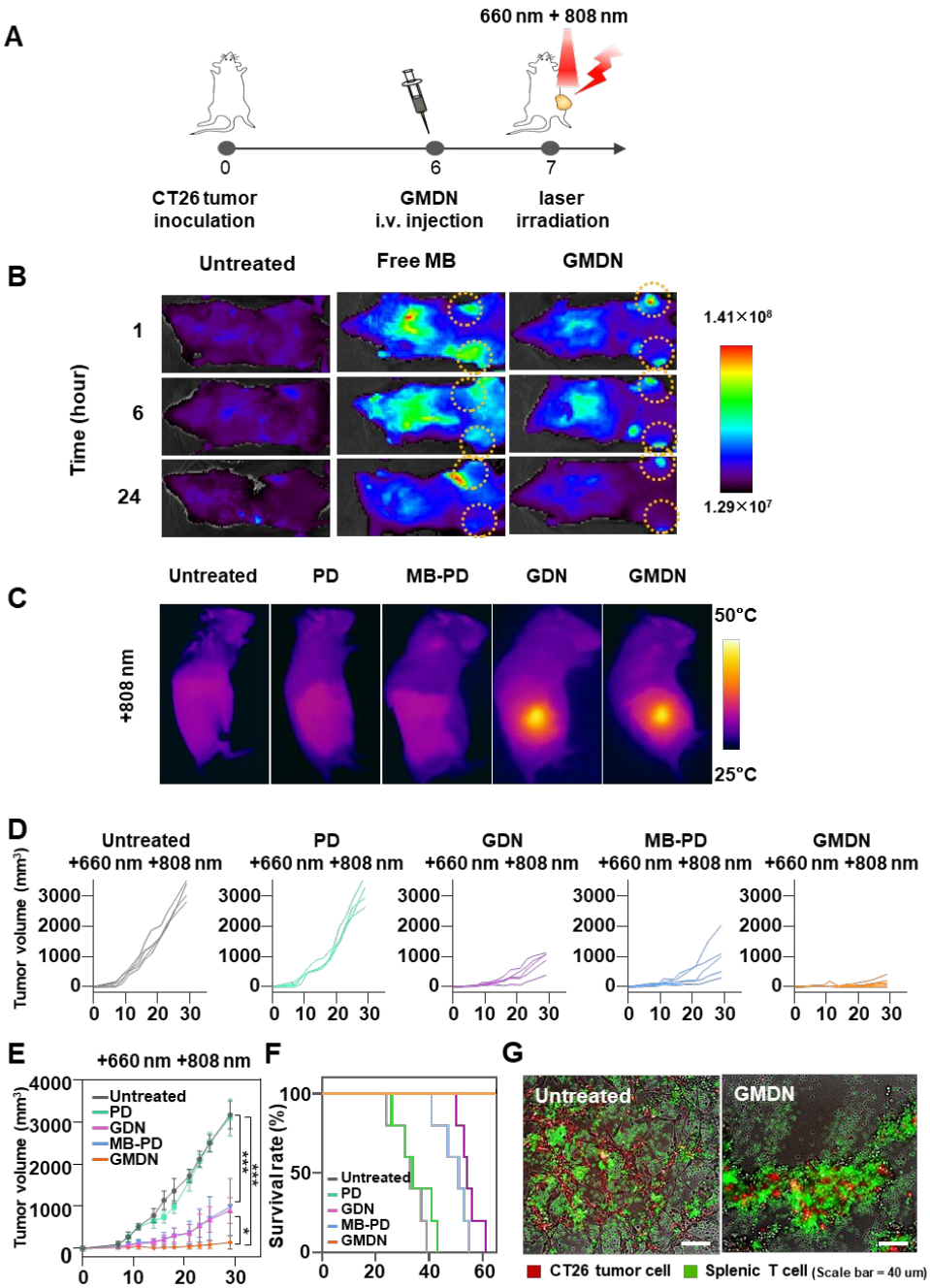

Figure 5. In vivo synergistic dual phototherapy of GMDN. The in vivo anti-tumor efficacy of GMDN was evaluated in CT26 tumor-bearing mice after light irradiation. (A) After CT26 tumor inoculation, GMDN were intravenously injected, followed by dual irradiation. (B) In vivo biodistribution of GMDN was evaluated by detecting fluorescence intensity from MB. (C) In vivo photothermal effect was confirmed by temperature measurement at the tumor site upon NIR irradiation. (D,E) In vivo anti-tumor efficacy was evaluated by tumor volume measurement up to 30 days after first

tumor inoculation. (F) Survival was monitored for 65 days. (G) Anti-tumor efficacy was evaluated in a tumor cell co-culture model involving splenic T cells from treated or untreated mice (*$p<0.05$; ***$p<0.001$).

4. Discussion

Here, we developed dual light-responsive nanocluster GMDN, which can exert a dual phototherapeutic effect for cancer phototherapy. Our use of a long DNA strand produced from RCA as a backbone for intercalating MB and clustering gold ions conferred multi-functionality to the nanoclusters as a theranostic formulation.

We used RCA to generate a repeated-sequence long PD strand that was then used as a scaffold for therapeutic cargo loading. As a natural biopolymer, the DNA nanostructure has great potential in nanotechnology [21]. For example, the fabrication and construction of a DNA-based structure can be easily controlled due to its intrinsic intermolecular interactions. DNA can form duplex, hairpin, loop, and/or G-quadruplex structures, which can endow the nanostructure with unique functions. The ease of sequence design can also give additional functionality. Most of all, DNA is a biocompatible and safe material that is suitable for clinical application.

The robust nanocluster formation by PD, MB, and gold was confirmed by elemental analysis. MB is a ROS-generating photoresponsive dye and DNA-intercalating agent [15]. By binding to double-stranded DNA with high affinity, the MB and PD formed a stable MB-PD complex. When gold ions were reduced to gold clusters on the PD backbone, the bulky PD structure was compacted to nano-size and MB-entrapping gold nanoclusters were formed.

The resulting GMDN nanoparticles could respond to dual light for photothermal and photodynamic therapy, respectively. When the GMDN were applied to cancer cells, the particles were efficiently internalized, whereas this was not true for the micro-sized bulky nanostructures used for comparison (Fig. 3F). The enhanced cellular uptake due to nanocluster formation was associated with a synergistic anti-cancer effect. Our in vitro studies revealed that while photothermal therapy or photodynamic therapy alone could not induce significant anti-cancer efficacy, the simultaneous treatment of dual phototherapy resulted in a dramatic anti-cancer killing effect (Fig. 4G, 4H). The use of dual lights has been reported to exert synergistic anticancer efficacy compared to single light irradiation [22-24]. The synergistic effects can be explained by several factors. First, the combination of dual lights has been shown to overcome the limited penetration depth of red light. Secondly, the hyperthermia condition by photothermal therapy at 808 nm has been observed to increase the uptake of photosensitizers by tumor cells [23]. Thirdly, the singlet oxygen generated by photosensitizers at 660 nm is known to attack heat-shock proteins, enhancing the photothermal effect by 808 nm [25].

GMDN can enable the imaging of tumor tissues, as MB has been used in clinical settings as a cancer diagnostic dye. When GMDN were administered intravenously, significant accumulation in tumor tissue was observed. Since nanoparticles are intrinsically able to accumulate in tumor tissues through the enhanced retention and permeability effect, a nano-

formulation that includes an imaging agent can aid in tumor diagnosis [26]. The biodistribution results obtained in this study suggest that GMDN showed improved tumor imaging with higher selectivity, as compared to the same amount of free MB.

For translation of this study to the colon cancer patients, optical fibers need to be used as a light source to irradiate the deep lesion of the patients [27]. A recent study reported that a 100 μm-diameter optical fiber could provide photothermal ablation of colorectal cancer metastasized to the liver [28]. In another study, an optical fiber with a 20-mm cylindrical diffuser has been used for photodynamic therapy of cancer patients [29]. Molecular imaging data obtained through GMDN might be useful for the treatment of image-guided phototherapy, which requires access to the correct lesion using optical fibers.

GMDN also showed a synergistic anti-cancer effect in an animal model. When tumor growth was monitored for 30 days after photo-treatment, photothermal therapy or photodynamic therapy alone showed limited therapeutic efficacy with continued tumor growth. However, complete tumor ablation was observed at day 65 after dual photothermal and photodynamic therapy, and no mortality was recorded during this period.

4. References

[1] Li F, Qin Y, Lee J, Liao H, Wang N, Davis TP, Qiao R, Ling D. Stimuli-responsive nano-assemblies for remotely controlled drug delivery. J Control Release. 2020 Jun 10;322:566-592.

[2] Kim D, Byun J, Park J, Lee Y, Shim G, Oh YK. Biomimetic polymeric nanoparticle-based photodynamic immunotherapy and protection against tumor rechallenge. Biomater Sci. 2020 Feb 21;8(4):1106-1116.

[3] Le QV, Suh J, Choi JJ, Park GT, Lee JW, Shim G, Oh YK. In Situ Nanoadjuvant-Assembled Tumor Vaccine for Preventing Long-Term Recurrence. ACS Nano. 2019 Jul 23;13(7):7442-7462.

[4] Shim G, Ko S, Park JY, Suh JH, Le QV, Kim D, Kim YB, Im GH, Kim HN, Choe YS, Cho J, Kim S, Oh YK. Tannic acid-functionalized boron nitride nanosheets for theranostics. J Control Release. 2020 Nov 10;327:616-626.

[5] Cho MH, Li Y, Lo PC, Lee H, Choi Y. Fucoidan-Based Theranostic Nanogel for Enhancing Imaging and Photodynamic Therapy of Cancer. Nanomicro Lett. 2020 Feb 4;12(1):47.

[6] Chen Y, Gao Y, Chen Y, Liu L, Mo A, Peng Q. Nanomaterials-based photothermal therapy and its potentials in antibacterial treatment. J Control Release. 2020 Dec 10;328:251-262.

[7] Zhao X, Yang CX, Chen LG, Yan XP. Dual-stimuli responsive and reversibly activatable theranostic nanoprobe for precision tumor-targeting and fluorescence-guided photothermal therapy. Nat Commun. 2017 May 19;8:14998.

[8] Shim G, Le QV, Suh J, Choi S, Kim G, Choi HG, Kim YB, Macgregor RB Jr, Oh YK. Sequential activation of anticancer therapy triggered by tumor microenvironment-selective imaging. J Control Release. 2019 Mar 28;298:110-119.

[9] Yang H, Le QV, Shim G, Oh YK, Shin YK. Molecular engineering of antibodies for site-specific conjugation to lipid polydopamine hybrid nanoparticles. Acta Pharm Sin B. 2020 Nov;10(11):2212-2226.

[10] Li X, Lovell JF, Yoon J, Chen X. Clinical development and potential of photothermal and photodynamic therapies for cancer. Nat Rev Clin Oncol. 2020 Nov;17(11):657-674.

[11] Choi K, Riviere JE, Monteiro-Riviere NA. Protein corona modulation of hepatocyte uptake and molecular mechanisms of gold nanoparticle toxicity. Nanotoxicology. 2017 Feb;11(1):64-75.

[12] Byun J, Kim D, Choi J, Shim G, Oh YK. Photosensitizer-Trapped Gold Nanocluster for Dual Light-Responsive Phototherapy. Biomedicines. 2020 Nov 20;8(11):521.

[13] Huang YY, Wintner A, Seed PC, Brauns T, Gelfand JA, Hamblin MR. Antimicrobial photodynamic therapy mediated by methylene blue and potassium iodide to treat urinary tract infection in a female rat

model. Sci Rep. 2018 May 8;8(1):7257.

[14] dos Santos AF, Terra LF, Wailemann RAM, Oliveira TC, Gomes VD, Mineiro MF, et al. Methylene blue photodynamic therapy induces selective and massive cell death in human breast cancer cells. Bmc Cancer. 2017;17.

[15] Jin H, Kim MG, Ko SB, Kim DH, Lee BJ, Macgregor RB, et al. Stemmed DNA nanostructure for the selective delivery of therapeutics. Nanoscale. 2018;10(16):7511-8.

[16] Shim G, Park J, Kim MG, Yang G, Lee Y, Oh YK. Noncovalent tethering of nucleic acid aptamer on DNA nanostructure for targeted photo/chemo/gene therapies. Nanomedicine. 2020 Feb;24:102053.

[17] Ali MRK, Wu Y, El-Sayed MA. Gold-Nanoparticle-Assisted Plasmonic Photothermal Therapy Advances Toward Clinical Application. J Phys Chem C. 2019;123(25):15375-93.

[18] Siddique S, Chow JCL. Application of Nanomaterials in Biomedical Imaging and Cancer Therapy. Nanomaterials (Basel). 2020 Aug 29;10(9):1700.

[19] Pearce K, Thipe VC, Henkel RR, Katti KV. Green Nanotechnology as an innovative drug delivery approach for Typha capensis and Naringenin-New class of phytochemical embedded biocompatible gold nanoparticles in prostate cancer therapy. J Drug Deliv Sci Tec. 2023;80.

[20] Rastinehad AR, Anastos H, Wajswol E, Winoker JS, Sfakianos JP, Doppalapudi SK, Carrick MR, Knauer CJ, Taouli B, Lewis SC, Tewari AK, Schwartz JA, Canfield SE, George AK, West JL, Halas NJ. Gold nanoshell-localized photothermal ablation of prostate tumors in a clinical pilot device study. Proc Natl Acad Sci U S A. 2019 Sep 10;116(37):18590-18596.

[21] Hu Y, Niemeyer CM. From DNA Nanotechnology to Material Systems Engineering. Adv Mater. 2019;31(26).

[22] Shim G, Kim MG, Jin H, Kim J, Oh YK. Claudin 4-targeted nanographene phototherapy using a Clostridium perfringens enterotoxin peptide-photosensitizer conjugate. Acta Pharmacol Sin. 2017 Jun;38(6):954-962.

[23] Liu X, Su H, Shi W, Liu Y, Sun Y, Ge D. Functionalized poly(pyrrole-3-carboxylic acid) nanoneedles for dual-imaging guided PDT/PTT combination therapy. Biomaterials. 2018 Jun;167:177-190.

[24] Li W, Yang J, Luo L, Jiang M, Qin B, Yin H, Zhu C, Yuan X, Zhang J, Luo Z, Du Y, Li Q, Lou Y, Qiu Y, You J. Targeting photodynamic and photothermal therapy to the endoplasmic reticulum enhances immunogenic cancer cell death. Nat Commun. 2019 Jul 26;10(1):3349.

[25] Heo JY, Noh JH, Park SH, Ji YB, Ju HJ, Kim DY, Lee B, Kim MS. An Injectable Click-Crosslinked Hydrogel that Prolongs Dexamethasone Release from Dexamethasone-Loaded Microspheres.

Pharmaceutics. 2019 Sep 1;11(9):438.

[26] Fang J, Islam W, Maeda H. Exploiting the dynamics of the EPR effect and strategies to improve the therapeutic effects of nanomedicines by using EPR effect enhancers. Adv Drug Deliver Rev. 2020;157:142-60.

[27] Khot MI, Andrew H, Svavarsdottir HS, Armstrong G, Quyn AJ, Jayne DG. A Review on the Scope of Photothermal Therapy-Based Nanomedicines in Preclinical Models of Colorectal Cancer. Clin Colorectal Cancer. 2019 Jun;18(2):e200-e209.

[28] Parchur AK, Sharma G, Jagtap JM, Gogineni VR, LaViolette PS, Flister MJ, White SB, Joshi A. Vascular Interventional Radiology-Guided Photothermal Therapy of Colorectal Cancer Liver Metastasis with Theranostic Gold Nanorods. ACS Nano. 2018 Jul 24;12(7):6597-6611.

[29] Shafirstein G, Battoo A, Harris K, Baumann H, Gollnick SO, Lindenmann J, Nwogu CE. Photodynamic Therapy of Non-Small Cell Lung Cancer. Narrative Review and Future Directions. Ann Am Thorac Soc. 2016 Feb;13(2):265-75.

Chapter III

Cold plasma-actuated on-site hydrogel for remodeling tumor immune microenvironment

1. Introduction

Immune checkpoint inhibitors work by inhibiting the immune-evading interaction between tumor cells and T cells and have recently emerged as major players in immunotherapy. Several immune checkpoint inhibitors have been developed as products for clinical use [1]. For example, anti-PD-L1 and anti-CTLA antibodies have been extensively used to treat various cancers. Despite the therapeutic success of immune checkpoint inhibitors, however, they are usually used in combination with anticancer chemotherapeutics [2]. This is due, at least in part, to the ability of a tumor's cold immune environment to limit the efficacy of immune checkpoint inhibitors.

To convert the cold immune environment to a "hot" immune environment in a tumor, various nanoparticle-based strategies have been investigated. Nanoparticles entrapping immune stimulants, such as toll-like receptor agonist and interferon-gamma (IFNγ), have been exploited to reeducate M2-like macrophages to M1-like macrophages [3-5]. Nanoparticle-based systems have also been used to improve T cell infiltration and activation [6,7]. Although progress has been made using diverse nanoparticles, it would be helpful to design a system that could facilitate the immunogenic cell death of tumor cells and the uptake of tumor-associated antigens (TAA) by activated dendritic cells (DC) as a means to enhance the immunotherapeutic efficacy. Notably, the sustainable and repeated delivery of antigens and adjuvants has been shown to increase the efficacy of antigen presentation by DC [8].

Cold atmospheric plasma (CAP) is an external stimulus that can generate reactive oxygen species (ROS) [9 ,10] and has been studied for biomedical applications [11]. Recent reports indicate that CAP irradiation can induce ROS-mediated tumor cell killing. The exposure of tumor cells to ROS has been shown to increase the exposure of "eat-me" signals on the damaged tumor cell surfaces, generating tumor-associated antigens (TAA) [12]. To fully remodel the tumor immune microenvironment, however, it will be necessary to trigger uptake of TAA by DC and increase subsequent antigen processing.

Here, we designed a formulation that exists as a liquid for injection but forms an on-site hydrogel in response to externally applied CAP. We hypothesized that CAP could: 1) function to generate ROS and produce TAA; and 2) make an on-site hydrogel that would act as a sustainable matrix of nanoadjuvants and TAA. To test these hypotheses, we exploited the ROS-responsive gelation feature of hyaluronic acid (HA)-tyramine conjugate (HAT) (Fig. 1A). As a model nanoadjuvant, we loaded transforming growth factor beta (TGFβ) receptor kinase inhibitor (TRKI) into lipid nanoparticles (TLN). CAP irradiation of nanoparticle-loaded HAT induced phenol polymerization of HAT to yield TLN entrapped in a matrix of CAP-induced hydrogel (TLN@CHG) (Fig. 1B). TLN@CHG is proposed to facilitate the phagocytosis of TAA by DC and activate tumor antigen presentation by the TLN nanoadjuvant, thereby remodeling the tumor immune microenvironment (Fig. 1C).

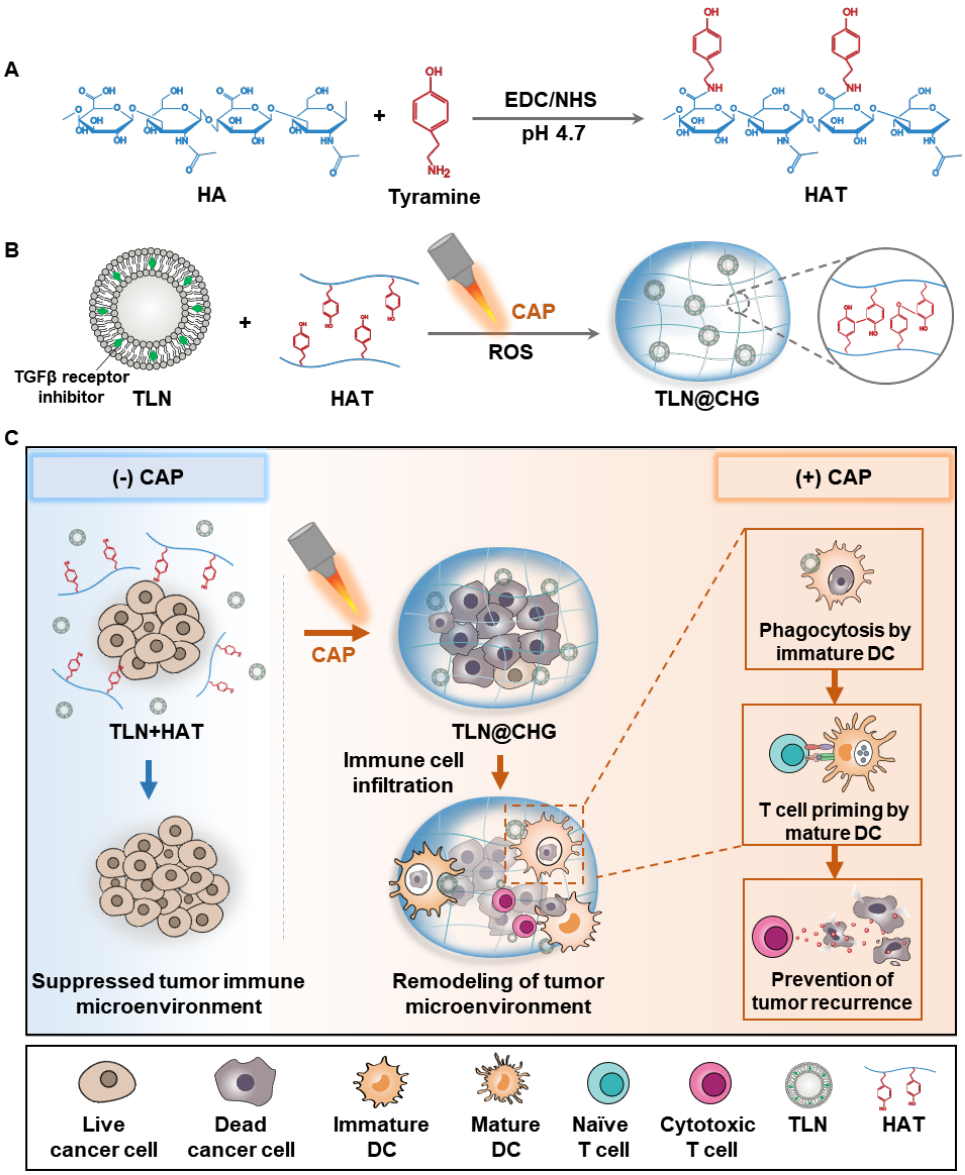

Figure 1. Schematic illustration of CAP-actuated hydrogel with TRKI-loaded nanoparticles and the proposed mechanism of immune-inflamed micro-network. (A) Chemical structure and CAP-induced crosslinking of HAT are depicted. (B) Schematic illustration of the CAP-induced formation of TLN@CHG. (C) In vivo gelation of TLN@CHG was executed by CAP treatment. CAP irradiation induced the immunogenic cell death of tumor cells, which express the "eat me" signal; this functions as a tumor-associated antigen (TAA). TLN@CHG acts as a TAA reservoir to remodel the tumor immune microenvironment, resulting in DC recruitment and maturation. The priming of T cells by mature DC can prevent tumor recurrence via a systemic immune response.

2. Materials and methods

Synthesis of HA derivative

HAT was synthesized as previously reported [13] with slight modification (Fig. S1A). Briefly, 100 mg of HA (201 kDa, 0.264 mmol; Contipro Inc., Dolní Dobrouč, Czech Republic) and 225 mg of tyramine hydrochloride (1.325 mmol; Sigma-Aldrich, St. Louis, MO, USA) were dissolved in 10 ml of triple distilled water (TDW). Subsequently, 100 mg of 1-ethyl-3-(3-dimethylaminopropyl) carbodiimide and 60 mg of N-hydroxysuccinimide were added. For the conjugation reaction, the mixture was stirred at room temperature overnight at pH 4.7. To remove unconjugated tyramine, the solution was dialyzed in 100 mM sodium chloride solution for 2 days, followed by dialysis against 25% ethanol solution for 1 day and against TDW for 1 day (molecular weight cutoff: 1000 Da). The resulting HAT was lyophilized. 1H nuclear magnetic resonance (NMR) spectral analysis was used to confirm the synthesis of HAT and calculate the degree of substitution for tyramine in HA (Fig. S1B).

Preparation and characterization of TGFβ receptor kinase inhibitor-loaded lipid nanoparticles

TGFβ receptor kinase inhibitor (TRKI, SB525334; Selleck Chemicals, Houston, TX, USA) was encapsulated in lipid nanoparticles. For nanoparticle preparation, egg L-α-phosphatidylcholine (PC), egg L-α-phosphatidyl-DL-glycerol (PG), cholesterol (Chol) and TRKI were mixed at a molar ratio of 2:2:1:0.1 and the organic solvent was evaporated under high vacuum using a rotary evaporator (CCA-1110; Tokyo Rikakikai, Tokyo, Japan). In some experiments, Lissamine™ Rhodamine B 1,2-dihexadecanoyl-sn-glycero-3-phosphoethanolamine (Rhodamine DHPE; Thermo Fisher Scientific, Inc., Waltham, MA, USA) was added to the lipid mixture during nanoparticle preparation. The thin lipid film was hydrated with phosphate buffered saline (PBS, pH 7.4), vortexed, and extruded through a 0.2-μm membrane filter (Thermo Fisher Scientific, Inc.) to yield TRKI-loaded lipid nanoparticles (TLN). Plain lipid nanoparticles without TRKI (PLN) were prepared as a control.

The size distribution and zeta potential were evaluated using an ELSZ-1000 (Photal, Osaka, Japan). The morphology of nanoparticles was observed by transmission electron microscopy (TEM). For TEM imaging, 10 μl of nanoparticles was dropped onto a copper grid and air dried. For negative staining, the grid was stained with 2% uracyl acetate and washed twice with TDW. The nanoparticles were observed under a transmission electron microscope (Talos L120C; Thermo Fisher Scientific, Inc.).

Characterization of CAP-induced hydrogel

CAP (P500-SM, Flamme Inc., Gyeonggi-do, Republic of Korea) with compressed air was used to induce the crosslinking of tyramine with horseradish peroxidase (HRP, Sigma-Aldrich). For the production of CAP,

compressed air was used at a flow rate of 1 liter per minute under a voltage of 15 kV at a frequency of 20 kHz. During CAP irradiation, the distance between the device and the mixture of HAT and HRP was fixed at 1 cm. Crosslinking of tyramine was evaluated by the color change and absorbance of tyramine solution. Tyramine solution (10 mg/ml) containing HRP (5 U/ml) was irradiated by CAP for 0, 1, 2, 3, 4, and 5 min. During the CAP irradiation, photographs and videos were recorded, followed by measurement of the absorbance spectrum with a SpectraMax M5 microplate reader (Molecular Devices, Silicon Valley, CA, USA). To fabricate CAP-induced hydrogel from HAT solution, 0.1 ml of HAT (10 mg/ml) was mixed with 0.5 U of HRP and irradiated with CAP for 5 min. The resulting CAP-induced HA-based hydrogel (CHG) was stored at 4ºC until use. To form TLN-loaded CHG (TLN@CHG), TLN containing 0.1 μmole of TRKI was mixed with 0.1 ml of HAT (10 mg/ml) and HRP, and irradiated with CAP. In some experiments, fluorescein-conjugated-bovine serum albumin (fBSA, 100 μg) was added to the binary mixture of HAT and HRP or the tertiary mixture of TLN, HAT, and HRP, and irradiated with CAP, resulting in fBSA-loaded CHG (fBSA@CHG) or fBSA-loaded TLN@CHG (TLN/fBSA@CHG), respectively. For comparison with TLN@CHG, TLN containing 0.1 μmole of TRKI was mixed with 0.1 ml of HAT (10 mg/ml) without CAP irradiation to form a physical mixture (TLN+HAT).

Rheological properties were evaluated using a rotational rheometer (DHR-1; TA Instruments Ltd., New Castle, DE, USA) at various viscoelastic parameters with fixed frequency. For analysis of the swelling ratio, dehydrated hydrogel was immersed in water and the weight of the rehydrated hydrogel was measured at various time points. The swelling ratio was calculated with the following equation: Wswollen-Wdry / Wdry × 100 = swelling ratio (%) [14]. The morphology and elemental compositions of the hydrogels were observed by field-emission scanning electronic microscopy (SEM) combined with energy dispersive spectroscopy (EDS; AURIGA, Carl Zeiss AG, Oberkochen, Germany).

Intracellular ROS and cell viability

Generation of intracellular ROS was detected using a fluorescent oxidative stress indicator. CT26 colon carcinoma cells (American Type Culture Collection (ATCC), Manassas, VA, USA) were treated with TLN, TLN+HAT, CHG, or TLN@CHG. For treatment of CT26 cells with CHG or TLN@CHG, a CT26 cell pellet (5×105 cells) was mixed with 0.1 ml of HAT (10 mg/ml) and HRP (5 U/ml), and irradiated with a plasma jet for 5 min to form CHG or TLN@CHG hydrogels containing CT26 cells. The hydrogels were treated with 1 ml of hyaluronidase (5 U/ml, Sigma-Aldrich) for 1 hr and isolated single cells were stained with CM-H2DCFDA (Thermo Fisher Scientific, Inc.) according to the manufacturer's protocol. The fluorescence intensity of intracellular ROS was measured by a flow cytometer (BD Biosciences, San Jose, CA, USA). Cell viability was evaluated by 3-(4,5-

dimethylthizol-2-yl)-2,5-diphenyltetrazolium bromide (MTT) assay. CT26 cells were treated with CHG or TLN@CHG and exposed to 1 ml of hyaluronidase (5 U/ml) for 1 hr, and isolated single cells were seeded to 24-well plates and incubated for 23 hr at 37oC. To quantify the dead cell population following CAP treatment, the cells were stained with MTT (Sigma-Aldrich).

Animal studies

Five-week-old Balb/c mice (Raon Bio, Yongin, Republic of Korea) were used for monocyte isolation and in vivo experiments. All studies using animals were conducted under the Guidelines for the Care and Use of Laboratory Animals of the Institute of Laboratory Animal Resources in Seoul National University (approved animal experimental protocol number, SNU-190417-15).

DAMP exposure study

The exposure of DAMP signals on cells was assessed to evaluate immunogenic cancer cell death. CT26 cells were treated with the various formulations and the resulting CHG or TLN@CHG hydrogels containing CT26 cells were treated with 1 ml of hyaluronidase (5 U/ml) for 1 hr. The level of ATP secretion, one of DAMP signals, was observed in supernatants of cells treated with various samplesusing an ATP determination kit (Thermo Fisher Scientific, Inc.). The isolated cell suspensions were seeded to 24-well plates and incubated for 1 day at 37oC. The cells were collected, stained with mouse anti-calreticulin (CRT) antibody (Santa Cruz Biotechnology, Inc., Dallas, TX, USA; catalog No. sc-166837, Lot No. C2917) for 1 hr, and further stained with Alexa Fluor®647-conjugated goat anti-mouse IgG antibody (BioLegend, Inc., San Diego, CA, USA; catalog No. 405322, Lot No. B275544) for 1 hr. The CRT-positive cell population was measured by flow cytometry. For in vivo assessment of CRT exposure, 5-week-old Balb/c mice were subcutaneously injected in the right flank with 106 CT26 cells. After 7 days, the tumor sites were injected with 0.1 ml of HAT (10 mg/ml) and HRP (5 U/ml). After CAP irradiation for 5 min, TLN (TRKI dose: 1.5 mg/kg) was injected to form TLN@CHG in vivo. One day later, the tumor tissues were extracted and single-cell suspensions were collected. The tumor cells were stained with anti-CRT antibody (Santa Cruz Biotechnology, Inc.) and subjected to flow cytometry.

Cancer cell phagocytosis by DC

To evaluate the phagocytosis of CAP-irradiated cancer cells by DC, CAP-irradiated cancer cells were co-cultured with bone marrow-derived DC (BMDC) and subjected to real-time recording and TEM imaging. BMDC were isolated from 5-week-old Balb/c mice as previously described [15]. For real-time recording, the BMDC were stained with CellTracker Red CMTPX dye (Thermo Fisher Scientific, Inc.) and seeded to a 96-well clear-bottom

black polystyrene microplate (Sigma-Aldrich). CT26 cells were irradiated with CAP for 5 min, labeled with CellTracker Green CMFDA dye (Thermo Fisher Scientific, Inc.), and then added along with TLN (TRKI dose: 10 μM) to the BMDC-seeded plate. Co-cultures of CT26 cells and BMDC were observed by an Operetta High-Content Imaging System (PerkinElmer, Inc., Waltham, MA, USA). For cellular TEM imaging, the cells were harvested after 24 hr and fixed with Karnovsky's solution for 2 hr at 4ºC. The collected cell pellets were washed with cold 0.05 M sodium cacodylate, fixed with 1% osmium tetroxide, and stained with 0.5% uranyl acetate. After dehydration through a graded ethanol series, cell pellets were resuspended in propylene oxide for 5 min and mixed with Spurr's resin. The resin was cut into thin sections (60 nm thick) with an ultramicrotome (Leica EM UC7; Leica Microsystems GmbH, Wetzlar, Germany) and observed by TEM (Talos L120C; Thermo Fisher Scientific, Inc.).

Activation of DC in co-culture with cancer cells

The ability of CAP-irradiated cancer cells to activate DC was investigated by assessing DC maturation markers. BMDC were seeded to a 24-well plate at 105 cells per well. On the following day, CT26 cells in TLN, TLN+HAT, CHG, or TLN@CHG were added to the BMDC-seeded plate. After 48 hr, the hydrogels were treated with hyaluronidase, the samples were centrifuged, and the supernatants were assessed for secreted cytokines using ELISA. The level of tumor necrosis factor-α (TNFα) was measured with a Quantikine ELISA kit (R&D Systems, Inc., Minneapolis, MN, USA) according to the provided instructions. The cells were then stained with fluorescein isothiocyanate (FITC)-conjugated anti-CD11c (BioLegend, Inc.; catalog No. 117306, Lot No. B277030) and anti-allophycocyanin (APC)-conjugated anti-CD86 (BioLegend, Inc.; catalog No. 105012, Lot No. B245162) for 1 hr. The stained cells were washed with fresh cold PBS and analyzed by flow cytometry.

Real-time recording of cancer cell phagocytosis by macrophages

Bone marrow-derived macrophages (BMDM) were differentiated to mimic TAM, and their cancer cell phagocytosis capability was measured. For differentiation to M2 type [16], BMDM were isolated from the femur bones of Balb/c mice (Raon Bio) and maintained in Iscove's Modified Dulbecco's medium (IMDM) supplemented with 10% fetal bovine serum (FBS; GenDEPOT, Katy, TX, USA), 100 U/ml penicillin (Capricorn Scientific, Ebsdorfergrund, Germany), 100 mg/ml streptomycin (Capricorn Scientific), and 10 ng/ml macrophage colony-stimulating factor (GenScript, New Jersey, USA). The cells were differentiated for 7 days with medium replacement on day 3. On day 7, the BMDM medium was replaced with M2-inducing IMDM containing 10% FBS and 10 ng/ml IL-4 (GenScript) and culture was continued for 1 day.

For the real-time recording, M2-like BMDM were stained with

CellTracker Red CMTPX dye (Thermo Fisher Scientific, Inc.) and seeded to a 96-well clear-bottom black polystyrene microplate. CT26 cells were irradiated with CAP for 5 min and labeled with CellTracker Green CMFDA dye (Thermo Fisher Scientific, Inc.). The CAP-treated CT26 cells and TLN (TRKI dose: 10 μM) were loaded to the BMDM-seeded plate and the co-culture of CT26 cells and BMDM was recorded in real-time using an Operetta High-Content Imaging System (PerkinElmer, Inc., Waltham, MA, USA).

Polarization study of macrophages co-cultured with cancer cells

The macrophage-reprogramming abilities of cancer cells treated with the various formulations were studied by assessing macrophage markers. The M2-differentiated BMDM were seeded to a 24-well plate at 105 per well and incubated overnight. CT26 cells in TLN, TLN+HAT, CHG, or TLN@CHG were loaded to the BMDM-seeded plate and culture was continued for 24 hr. The samples were centrifuged, the supernatants were collected, and the cell pellets were resuspended to single-cell suspensions, which were then stained with FITC-conjugated anti-CD11b (BioLegend, Inc.; catalog No. 101206, Lot No. B286843), APC-conjugated anti-F4/80 (BioLegend, Inc.; catalog No. 123116, Lot No. B268075), phycoerythrin (PE)-conjugated anti-CD206 (BioLegend, Inc.; catalog No. 141706, Lot No. B280038), and PE-conjugated anti-CD86 (BioLegend, Inc.; catalog No. 105008, Lot No. B267647) for 1 hr. The cells were washed and analyzed by flow cytometry. The levels of TNFα and IL-6 in the collected supernatant were quantified with a Quantikine ELISA kit (R&D Systems, Inc.).

Uptake of TLN by macrophages and DC

The cellular uptake of TLN was investigated using confocal laser scanning microscopy. M2-like BMDM and BMDC were stained with CellTracker CMFDA dye (Thermo Fisher Scientific, Inc.) and seeded to an 8-well chamber slide. CT26 cells were labeled with Vybrant™ DiD Cell-Labeling Solution (Thermo Fisher Scientific, Inc.) and irradiated with CAP for 5 min. Fluorescence-labeled TLN (Rhodamine; TRKI dose, 10 μM) and CAP-treated CT26 cells were loaded to the BMDM- or BMDC-seeded slides. On the following day, the treated cells were observed under confocal microscopy (TCS8; Leica).

In vivo ROS detection

TLN@CHG-mediated ROS generation in tumor-bearing mice was observed with the ROS indicator, hydro cyanine (hydro Cy)5.5, which was synthesized by reducing the iminium cations of cyanine dye [17]. The obtained hydro Cy5.5 was dissolved with dimethyl sulfoxide. Five-week-old Balb/c mice were subcutaneously injected in both flanks with 106 CT26 cells per injection. After 7 days, CT26 tumor-bearing mice were intravenously injected with hydro Cy5.5 (1 mg/kg). Ten minutes later, tumor sites or normal muscle areas were treated with TLN+HAT or TLN@CHG. The fluorescence

intensities of sample-treated sites were observed with an IVIS Spectrum In Vivo Imaging System (Perkin Elmer).

In vivo DC activation

The in vivo activation of DC was investigated by immunostaining of spleen tissues. Five-week-old Balb/c mice were subcutaneously injected in the left flank with 106 CT26 cells. Seven days later, the tumor sites of mice were treated with the various formulations. Forty-eight hours later, single-cell suspensions of splenocytes were obtained from spleens [18]. Red blood cells were lysed with ammonium/chloride/potassium-based buffer (ACK buffer; 0.15M NH4Cl, 1M KHCO3, 0.01M EDTA). The obtained splenocytes were stained with FITC-conjugated anti-CD11c, APC-conjugated anti-CD86, APC-conjugated anti-CD80 (BioLegend, Inc.; catalog No. 104714, Lot No. B271484), and APC-conjugated CD40 (BioLegend, Inc.) for 1 hr. The stained cells were washed with fresh cold PBS and analyzed by flow cytometry.

In vivo retention

The in vivo fate of TLN@CHG was observed by incorporating methylene blue during gelation and then tracing its fluorescence. Five-week-old Balb/c mice were subcutaneously injected with TLN@CHG and 10 nmole of methylene blue (Sigma-Aldrich), and then irradiated with CAP for 5 min. For comparison, TLN+HAT solution containing 10 nmole of methylene blue was subcutaneously injected to mice. Fluorescence intensity was observed daily using an IVIS Spectrum in Vivo Imaging System.

In vivo release of tumor-associated antigens from on-site hydrogel

To measure the in vivo release of TAA from TLN@CHG, fluorescence-conjugated bovine serum albumin (BSA; Sigma-Aldrich) was used as a model antigen. Alexa Fluor™ 680 N-hydroxysuccinimide ester (Thermo Fisher Scientific, Inc.) was conjugated with BSA according to the manufacturer's protocol. Five-week-old Balb/c mice were injected with TLN@CHG and 100 μg AlexaFluorTM 680-conjugated BSA (fBSA), and then subjected to CAP irradiation for 5 min. The fluorescence intensity of BSA in free form or in TLN/fBSA@CHG was measured using an IVIS Spectrum In Vivo Imaging System.

To study cross-presentation, B16F10-OVA cell pellets (5×105 cells) were mixed with 0.1 ml of HAT (10 mg/ml) and HRP (5 U/ml) and irradiated with the plasma jet for 5 min. TLN was then added to the hydrogel. This yielded a mass of B16F10 cells wrapped in TLN@CHG, which was strained (40-μm) and applied to BMDC. After 12 or 36 hr, the strainer was removed and the BMDC were stained with FITC-conjugated anti-CD11c and APC-conjugated anti-MHCI-SIINFEKL (BioLegend, Inc.; catalog No. 141606, Lot No. B273750) for 1 hr. The stained cells were washed with fresh cold PBS and analyzed by flow cytometry.

Immune cell profiling in primary and re-challenged tumor tissues

Active immune cells in tumor tissues were characterized using flow cytometry and immunofluorescence imaging. Five-week-old mice were subcutaneously inoculated with 106 CT26 cells in the left flank (day 0). After 10 days, mice were intratumorally injected with the various formulations and exposed to CAP irradiation. On the same day, 5×105 CT26 cells were subcutaneously re-challenged in the right flank. On day 14, primary tumors were extracted and single-cell suspensions were obtained from the tumor tissues. The cells were stained for dead cell exclusion using Zombie-UV fixable viability dye (BioLegend). For immune cell analysis, the cells were stained with BV421-conjugated anti-CD45 (BioLegend, catalog No. 103133, Lot No. B294378), PE/Cy5-conjugated anti-CD3, APC/Cy7-conjugated anti-CD8, PE-conjugated anti-CD11c, PerCP/Cy5.5-conjugated anti-CD11c, PerCP/Cy5.5-conjugated anti-TNFα, APC-conjugated IL6, Alexa 488-conjugated anti-MHCII, PE/Cy7-conjugated anti-CD86, FITC-conjugated anti-CD4, PE-conjugated anti-IFNγ, Alexa 647-conjugated anti-Granzyme B, and PE-conjugated anti-CD4 antibody. For high-dimensional FACS analysis, flow cytometry data were acquired on a BD LSRFortessa™ X-20 Flow Cytometer (BD Biosciences) using the BD FACS Diva software (BD Biosciences) and processed with the FlowJo software (FlowJo, Ashland, OR, USA). Live cell numbers were normalized to 16,000 for each group and dimensionality reduction was performed using the t-distributed stochastic neighbor embedding (t-SNE) method with six parameters and a perplexity of 30. Five cell populations were identified: CD45+CD3+CD8+ T cells, CD45+CD3+CD4+ T cells, CD45+CD3-CD11c+MHC+ dendritic cells, CD45+CD3-CD11c-MHCII- immune cells, and CD45- non-immune cells. These populations were manually gated and visualized in t-SNE plots.

For analysis of tumor-infiltrating lymphocytes, re-challenged tumors were harvested on day 14 and processed to single-cell suspensions, which were stained with anti-mouse CD3 and anti-mouse CD8. Immune cells were profiled as described above by flow cytometry. For immunofluorescence imaging, tumor tissues were extracted on day 14, fixed in 10% formalin, and processed to paraffin sections. The sections were stained with anti-mouse CD4 (Bio X Cell; catalog No. BE0003-1, Lot No. 699918M2B) and anti-CD8a using an OPAL Multiplex IHC kit (PerkinElmer, Inc.. The images were obtained using an automated multimodal tissue analysis system (Vectra, PerkinElmer, Inc.) and analyzed with the Inform software (PerkinElmer, Inc.).

Transcriptome analysis of the tumor immune microenvironment

Transcript expression of immune cells in tumor tissues was characterized by next-generation sequencing. Five-week-old mice were subcutaneously inoculated with 106 CT26 cells in the left flank and 10 days later treated with TLN@CHG. Four days later (day 14 of the experiment), tumors were extracted and processed to single-cell suspensions. T cells were stained with FITC-conjugated anti-CD3 and sorted using a FACSAria III (BD

Biosciences). Total RNA of sorted cells was obtained using TRIzol RNA Isolation Reagents (Thermo Fisher Scientific, Inc.) and tested for quality with an Agilent 2100 bioanalyzer running an RNA 6000 Nano Chip (Agilent Technologies, Amstelveen, Netherlands). Control and test RNA libraries were constructed using a QuantSeq 3' mRNA-Seq Library Prep Kit (Lexogen, Inc., Vienna, Austria) according to the manufacturer's instructions. High-throughput single-end 75 bp sequencing was conducted using a NextSeq 500 (Illumina, Inc., San Diego, CA, USA).

Primary tumor ablation and protection from tumor recurrence

The immunotherapeutic efficacy of each formulation was evaluated against primary and re-challenged tumors. CT26 cells (106) were subcutaneously transplanted into the left flanks of 5-week-old Balb/c mice. After 7 days, CT26 tumor-bearing mice were randomly distributed to six groups. Mice of the TLN@CHG group were intratumorally injected with 100 μl of HAT (10 mg/ml) supplemented with 0.5 U of HRP. After CAP irradiation for 5 min, the tumor site was treated with TLN (TRKI dose, 1.5 mg/kg) to form TLN@CHG. On the same day, 5×105 CT26 cells were subcutaneously re-challenged in the right flank. For depletion of CD8 T cells, mice were intraperitoneally injected with 200 μg of anti-CD8a antibody (Bio X Cell, West Lebanon, NH, USA; catalog No. BE0004-1, Lot No. 693018M2) on days 5, 8, 10, 12, 16, 23, and 30. The volumes of tumors were measured at 3-day intervals and calculated by the formula: tumor volume (mm3) = the longest length (mm) × the shortest length (mm)2 × 0.5 [19]. For assessment of long-term protective efficacy, completely cured mice were re-challenged with 5×105 CT26 cells at 180 days after the first inoculation. 4T1-luciferase (4T1-Luc cells; PerkinElmer, Inc.) breast cancer cells were inoculated as a negative control.

Tumor metastasis study

The systemic immune responses of mice treated with TLN@CHG were assessed in a lung metastasis model. 4T1-Luc cancer cells (106) were inoculated into the right flanks of mice. At day 7 post-inoculation, the mice were treated as described for the CT26 tumor model and then (on the same day) intravenously injected with 2×105 4T1-Luc cells. The growth of metastasized lung tumors was measured weekly using an IVIS Spectrum imaging system. At each studied time point, luciferin (PerkinElmer, Inc.) was intraperitoneally injected to the mice and luciferase activity was evaluated with bioluminescence imaging.

Analysis of memory T cells

To test the antigen-specific long-term immune response, the population of effector memory T (CD3+CD8+CD44highCD62Llow) cells was investigated among mice that had been completely cured by TLN@CHG. At 180 days after the first inoculation, these TLN@CHG-treated mice were re-

challenged with 106 CT26 cells in the right flank. After 7 days, the inguinal lymph nodes near or far from the tumor were extracted and dissociated to single-cell suspensions. The lymphocytes were stained with FITC-conjugated anti-CD3, PERCP/Cy5.5-conjugated anti-CD8a, PE-conjugated anti-mouse CD62L (BioLegend, Inc.; catalog No. 104412, Lot No. B266801), and APC-conjugated anti-mouse CD44 (BioLegend, Inc.; catalog No. 103007, Lot No. B239830) for 1 hr. The stained cells were washed and analyzed by flow cytometry.

Statistical analysis

One-way analysis of variance (ANOVA) with Tukey's post-hoc test was applied for statistical evaluation of experimental data. All statistical analyses were carried out using the GraphPad Prism software (v8.0, GraphPad Software, San Diego, CA, USA). A p-value less than 0.05 was considered statistically significant.

3. Results

Characterization of TLN and CAP-triggered hydrogel

CHG was generated on-site by crosslinking the tyrosine moieties of HAT with CAP-generated ROS. HAT was synthesized by conjugating the amine group of tyrosine to the carboxyl group of HA (Fig. 1A). The CAP-triggered crosslinking points between tyrosine moieties are illustrated in Fig. 1B. CAP was used as an external source to generate ROS (Fig. 2A). The air jet of CAP and the generated ROS are shown in Fig. 2B. The appearance of the tyramine solution changed from colorless to brown due to the crosslinking of tyramine, and the absorbance was increased upon CAP irradiation (Fig. 2C, Supplementary Video S1). CAP irradiation led to the formation of hydrogel, with the flowable HAT polymer shifting to the gel-form CHG (Fig. 2D). The entrapment of TRKI did not affect the size or zeta potential of TLN: It was nanoscale in size with a mean diameter of 112.2 ± 26.2 nm (Fig. 2E) and had a negative surface charge with a zeta potential of -47.38 ± 3.9 mV (Fig. 2F). Our release study revealed that the retention of TLN was highest in TLN@CHG (Fig. 2G). Our rheology study showed that the storage modulus of TLN@CHG was significantly higher than that of the physical mixture of TLN plus HAT (Fig. 2H). Unlike the physical mixture of TLN plus HAT, which showed no swelling capacity, TM@CHG showed a swelling ratio > 1500% after a 2-hr incubation in TDW (Fig. 2I). SEM imaging revealed that TLN@CHG had a porous network structure (Fig. 2J). Elemental mapping showed that TLN@CHG contained the carbon, oxygen, and nitrogen elements of HAT, and the phosphorus of TLN (Fig. 2K).

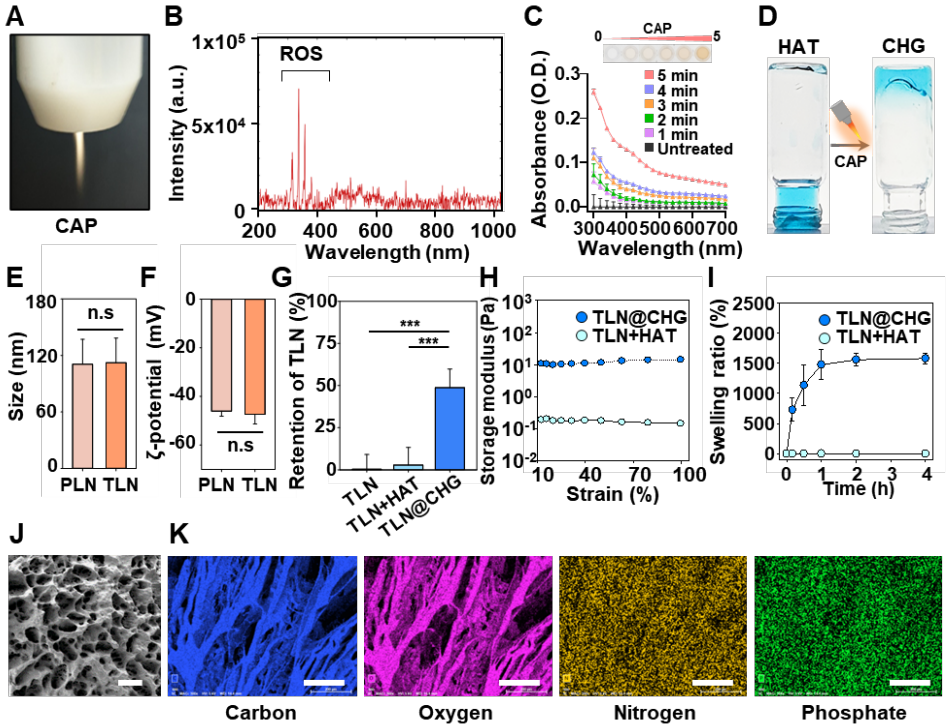

Figure 2. Characterization of TLN and TLN@CHG. (A) Plasma irradiation from a CAP generator. (B) Optical emission spectrum of CAP. (C) UV-Vis spectra of tyramine solution after CAP irradiation. (D) Appearance of HAT and CHG. (E,F) Average sizes (E) and zeta potentials (F) of PLN and TLN. (G) Retention of TLN was measured in a release study. (H) Storage modulus was measured using a rotational rheometer. (I) Swelling ratio was measured in TDW. (J) SEM imaging of TLN@CHG (scale bar, 100 μm). (K) EDS-TEM elemental mapping (scale bar, 200 μm) images of TLN@CHG (blue, carbon; purple, oxygen; yellow, nitrogen; green, phosphorus). (***$p < 0.001$; n.s., not significant) Supplementary Video 1. The formation of CAP-induced hydrogel is recorded.

DC-mediated phagocytosis of CAP-irradiated tumor cells and DC maturation

CAP irradiation induced immunogenic tumor cell death and TLN@CHG formation, with subsequent promotion of DC phagocytosis and activation (Fig. 3A). CHG- or TLN@CHG-treated CT26 cells showed significantly higher intracellular ROS levels than the other groups (Fig. 3B, 3C). The application of CAP affected the viability of CT26 tumor cells in an irradiation time-dependent manner (Fig. S1B). In CHG- and TLN@CHG-treated CT26 cells, cell viability decreased to 26.1 ± 6.3% and 24.1 ± 2.2%, respectively (Fig. 3D). DAMP signal-positive cells increased with the time of CAP irradiation (Fig. S1C-S1E). The ATP secretion of CT26 cells increased in the CHG- and TLN@CHG-treated groups (Fig. 3E). The CRT-positive populations were 44.8 ± 1.0% and 47.3 ± 0.8% in the CHG and TLN@CHG

groups, respectively (Fig. 3F, 3G). Immune cell recruitment of DAMP signals from TLN@CHG was observed by the migration of BMDC to the hydrogel (Fig. 3H). Compared to the untreated BMDC showing dispersed distribution, the coculture of BMDC with CT26 cells-loaded TLN@CHG showed migration into the hydrogel within 12 hr (Fig. 3H).

CAP-treated CT26 cells were co-cultured with BMDC and phagocytosis was observed by time-lapse imaging (Fig. 3I, Suppl. Video 2). Each step of phagocytosis is shown by representative capture images from video (Fig. 3I) and TEM imaging (Fig. 3J). Both live cell imaging (Fig. 3I) and TEM imaging (Fig. 3J) show the uptake of tumor cells by nearby DCs, and processing inside DC. Analysis of CD11c+ CD86+ cell populations of BMDC revealed that co-culture with CHG- or TLN@CHG-treated CT26 cells yielded 2.6- or 3.2-fold higher maturation effects, respectively, compared to co-culture with untreated CT26 cells (Fig. 3K). Similarly, TLN@CHG-treated CT26 cells induced the highest secretion of TNFα from BMDC (Fig. 3L).

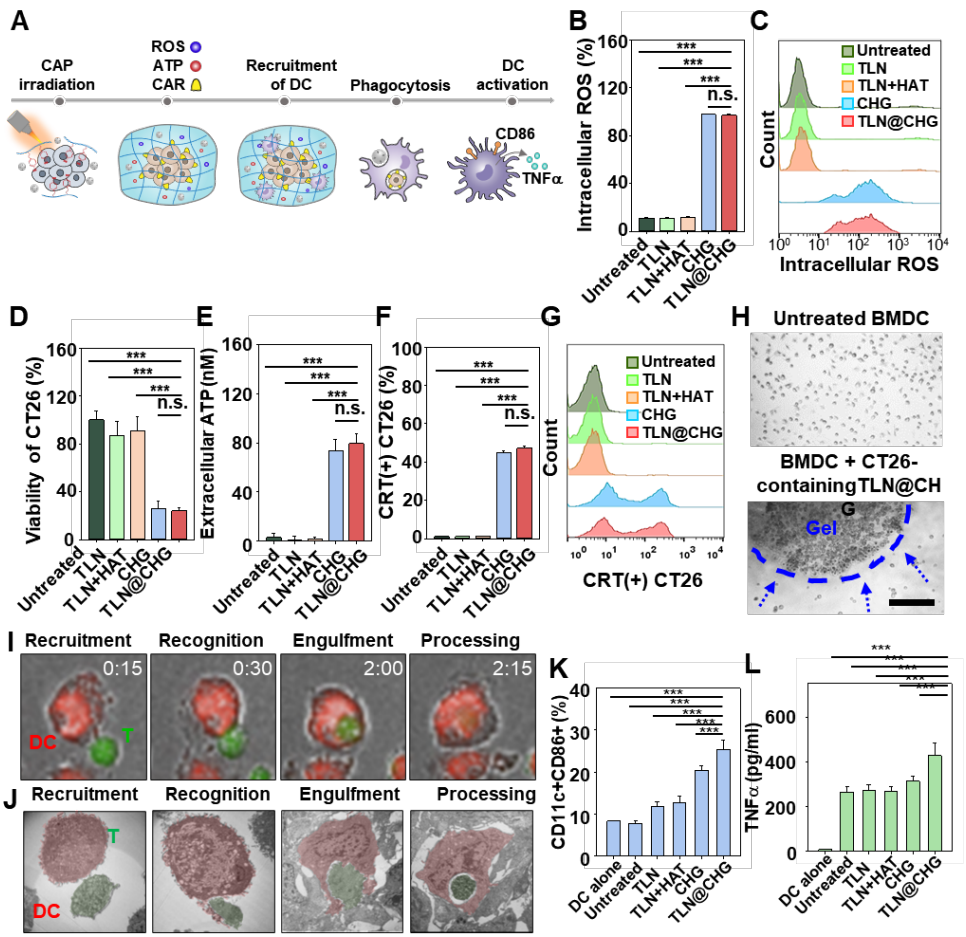

Figure 3. Phagocytosis of tumor cells by dendritic cells upon CAP irradiation (A) Schematic illustration of CAP-induced immunogenic tumor cell death and activation of DC. (B-G) CAP-mediated immunogenic cell

death of CT26 tumor cells treated with the various formulations. Intracellular ROS level was measured by H2DCFDA (B, C). (D) MTT assay was used to measure cell viability. (E) Secretion of ATP was measured in the supernatant of CT26 cells by assessment of luciferase activity. (F, G) Exposure of CRT on CT26 cells was analyzed by flow cytometry. (H) Recruitment of BMDC to CT26 cell-containing TLN@CHG was observed by microscopy. Scale bar = 50 μm. (I, J) Phagocytosis of CAP-irradiated tumor cells by BMDC was observed with live-cell imaging (J) and TEM imaging (J; BMDC, red; tumor cells, green). The actual time (H:MM) is displayed at upper right of images in (I). Real-time recording of tumor cell phagocytosis by BMDC is provided in Supplementary Video 2. (K) BMDC maturation ability was assessed by examining CD86 expression at 2 days after the addition of CT26 cells treated with the various formulations. (L) Secretory TNFα was measured from the supernatants of CT26 cell-treated BMDC. (*$p < 0.05$; **$p < 0.01$; ***$p < 0.001$; n.s., not significant)

In vivo retention of on-site hydrogel

The in vivo gelation of TLN@CHG can yield sustained release of TAA to the immune cells. CT26-bearing mice were treated with TLN@CHG and monitoring was performed for CHG (Fig. 4A, 4B) and fBSA as model antigen (Fig. 4C, 4D). The in vivo gelation of TLN@CHG was observed to entrap TLN and dying tumor cells, and thereby act as an antigen reservoir (Fig. 4A). The signal arising from the CAP-formable hydrogel was observed for up to 96 hr at the injection site, whereas the signal totally disappeared within 24 hr in the absence of CAP irradiation (Fig. 4B). Sustained release of antigen from the on-site hydrogel was confirmed using fBSA as a model antigen (Fig. 4C, 4D). The fluorescence signal of free fBSA at the injection site disappeared at 24 hr post-injection, whereas that of fBSA trapped within the CAP-responsive hydrogel was retained at tumor site (Fig. 4C), with 21.5% of the original signal level still observable at 48 hr post-injection (Fig. 4D).

CT26-bearing mice received intravenous injection of an ROS indicator and subsequent treatment the various formulations. Increased in vivo ROS generation was observed at tumor and non-tumor sites of TLN@CHG-treated CT26-bearing mice (Fig. 4E). Before CAP irradiation, the ROS level was 1.9-fold higher in the tumor tissue compared to the non-tumor tissue in TLN+HAT-treated mice. After CAP irradiation, the ROS level of TLN@CHG-treated mice was 4.1-fold greater in at the tumor site compared to the muscle site (Fig. 4F).

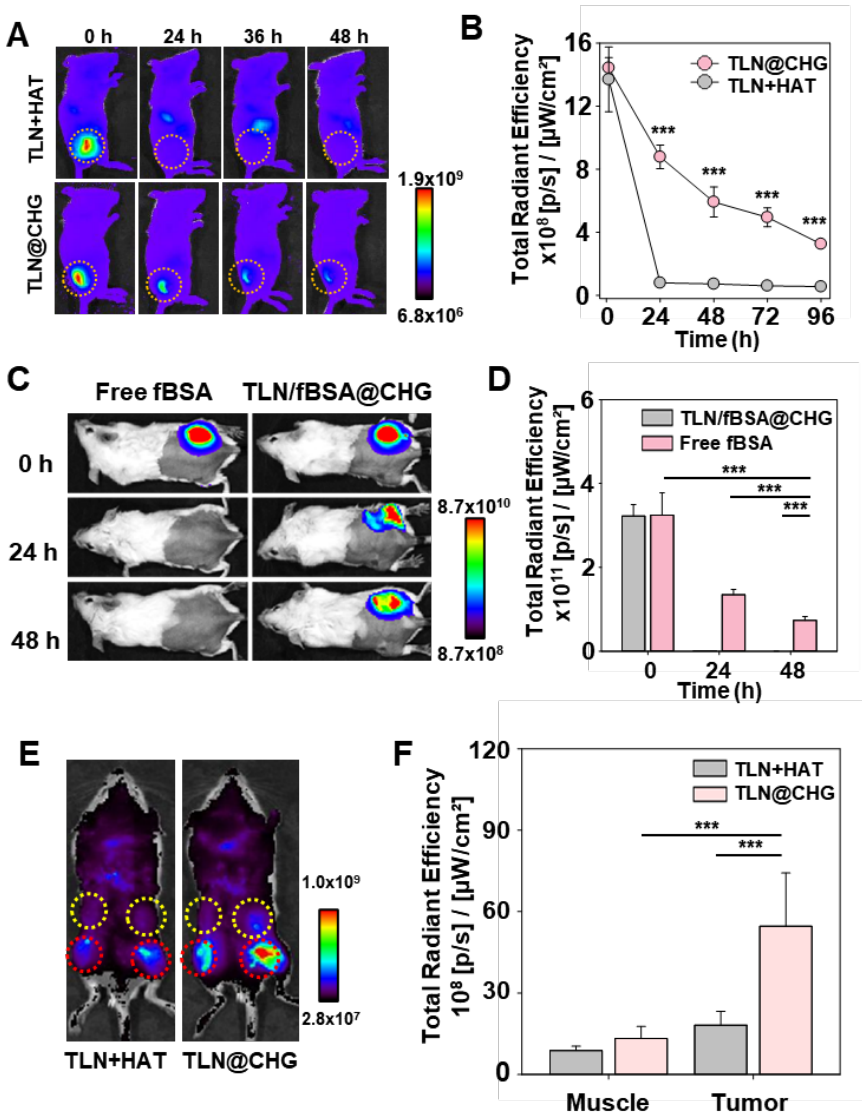

Figure 4. In vivo fate and ROS generation of TLN@CHG. (A) The in vivo fate of TLN+HAT or TLN@CHG was observed by in vivo molecular imaging. (B) The fluorescence intensity at the injection site was analyzed and plotted. (C) Retention of fBSA in TLN@CHG was assessed by in vivo molecular imaging. (D) Signal of fBSA was quantified at each time point. (***$p < 0.001$) (E, F) Balb/c mice were inoculated with CT26 tumor cells, treated with the various formulations, and monitored for ROS. (E) In vivo ROS generation was detected by fluorescence imaging of the ROS indicator immediately after CAP irradiation. (F) Fluorescence intensities were assessed at muscle (yellow circles) and tumor (red circles) sites.

Anti-tumor efficacy and protection effect of on-site hydrogel from the tumor recurrence

TLN@CHG revealed tumor ablation effects in primary tumors and

abscopal effects in models of distant tumor and lung metastasis. For the distant-tumor model, CT26 tumor-bearing mice were treated with the various formulations on day 7 after the first tumor inoculation, and the second tumor inoculation was performed at a distant site (also on day 7). Mice were monitored over 180 days (Fig. 5A). No mouse survived in the untreated, TLN, or TLN+HAT groups, and only 16% of CAP-treated group and 33% of CHA-treated mice survived to day 180 after the first tumor inoculation. In contrast, 100% mice of the TLN@CHG group showed tumor-free survival over the 180 days (Fig. 5B).

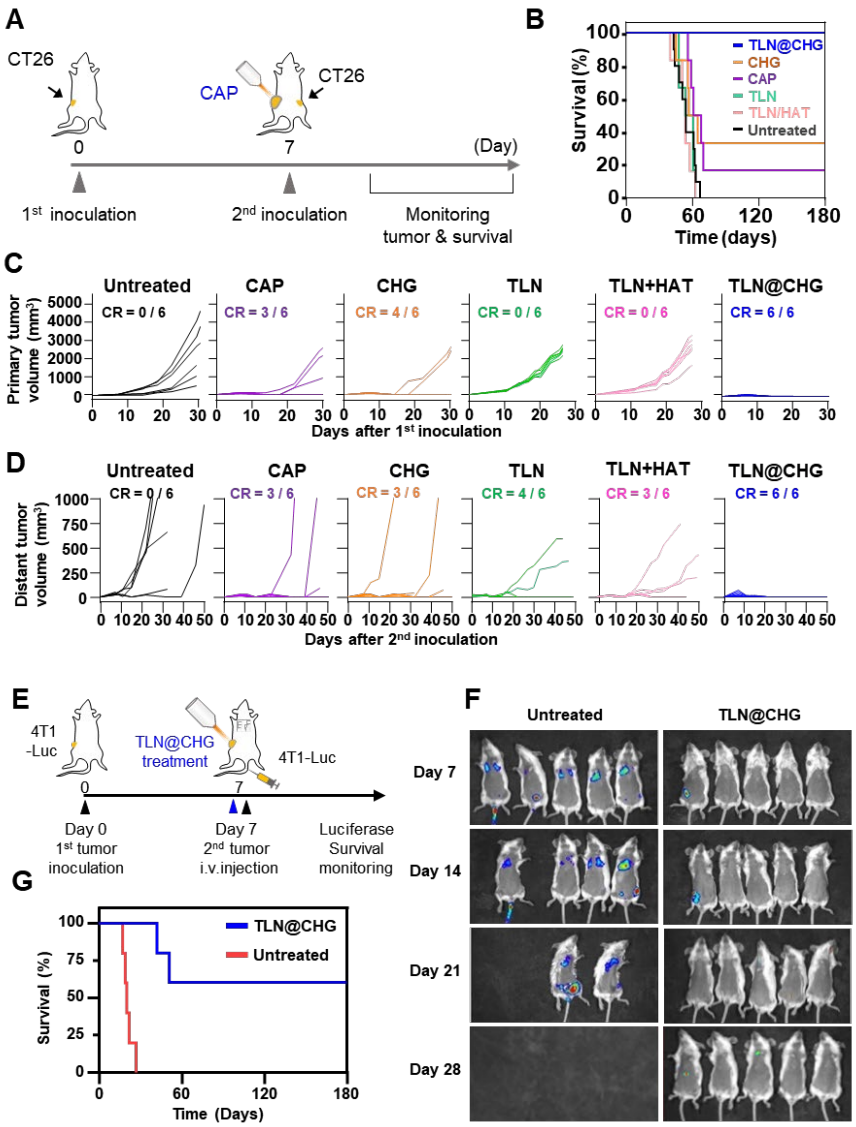

Figure 5. Anti-tumor efficacy of TLN@CHG treatment. (A) CT26-bearing mice were treated with the various formulations and given a second inoculation of CT26 tumor cells on the same day (day 7). (B) Survival of mice was monitored over 180 days. Primary (C) and rechallenged (D) tumors were

monitored and are shown as individual curves. (E) Scheme for generating the lung metastasis model using 4T1-Luc tumor cells. (F) Bioluminescence images of lung metastasis tumors in mice of the untreated and TLN@CHG groups. (G) Survival rate of 4T1 tumor-bearing mice treated with the different formulations.

Primary tumors were monitored for 30 days after inoculation. All mice of the untreated, TLN, and TLN+HAT groups exhibited tumor growth, while some of the CAP- and CHG-treated mice exhibited tumor burdens. In contrast, no tumor growth was observed in TLN@CHG-treated mice (Fig. 5C). After tumor re-challenge, complete response was observed in some mice of the CAP (3/6), CHG (3/6), TLN (4/6), and TLN+HAT (3/6) groups, whereas no mouse of the untreated group exhibited a complete response (0/6) (Fig. 5D). By comparison, 100% of TLN@CHG group mice exhibited a complete response (Fig. 5D). The anti-metastatic effect of our on-site hydrogel was investigated in the 4T1 lung metastasis model. Mice were treated with the various formulations on day 7 after the first tumor inoculation, and then received intravenous injection of 4T1-luciferase tumor cells (also on day 7) (Fig. 5E). Lung metastatic tumors were visualized by luminescence imaging of luciferase activity. The anti-metastatic effect in TLN@CHG-treated mice was significantly greater than that in untreated mice (Fig. 5F). Whereas 100% untreated mice were dead before day 28, 60% of TLN@CHG mice survived to 180 days (Fig. 5G).

Generation of immune-inflamed tumor micro-network by on-site hydrogel

Profiling of DC and T cells in the TLN@CHG-formed tumor micro-network was conducted by flow cytometry analysis and immunofluorescence imaging (Fig. 6A). The on-site gelation of TLN@CHG successfully increased the DC and T cell populations in the tumor (Fig. 6B). The DC population in TLN@CHG-treated mice was increased by 16.6- and 1.9-fold compared to the levels seen in untreated and CHG-treated mice, respectively (Fig. 6C). Significantly higher populations of CD4 T cells and CD8 T cells were observed in the TLN@CHG-treated group, which exhibited 13.6-fold (Fig. 6D) and 6.6-fold (Fig. 6E) increases, respectively, compared to the untreated group. Higher populations of CD4 T cells and CD8 T cells in TLN@CHG-treated tumors were also visualized with immunofluorescence imaging (Fig. 6F). Higher-level expression of DC activation markers was observed in DC of the TLN@CHG group. The expression levels of TNFA (Fig. 6G, K), IL-6 (Fig. 6H, L), MHCII (Fig. 6I, M), and CD86 (Fig. 6J, N) were 3.9-, 3.1-, 2.8-, and 4.1-fold higher, respectively, in DC of the TLN@CHG-treated group compared to the untreated group. In addition, we observed a prominent 5.7-fold increase of the IFNγ expression level of CD4 T cells in the TLN@CHG-treated group compared to the untreated group (Fig. 6O, Q). Significant elevation (6.2-fold) of the GzmB+ CD8 T cell population was also observed

in the TLN@CHG-treated group compared to the untreated group (Fig. 6P, R).

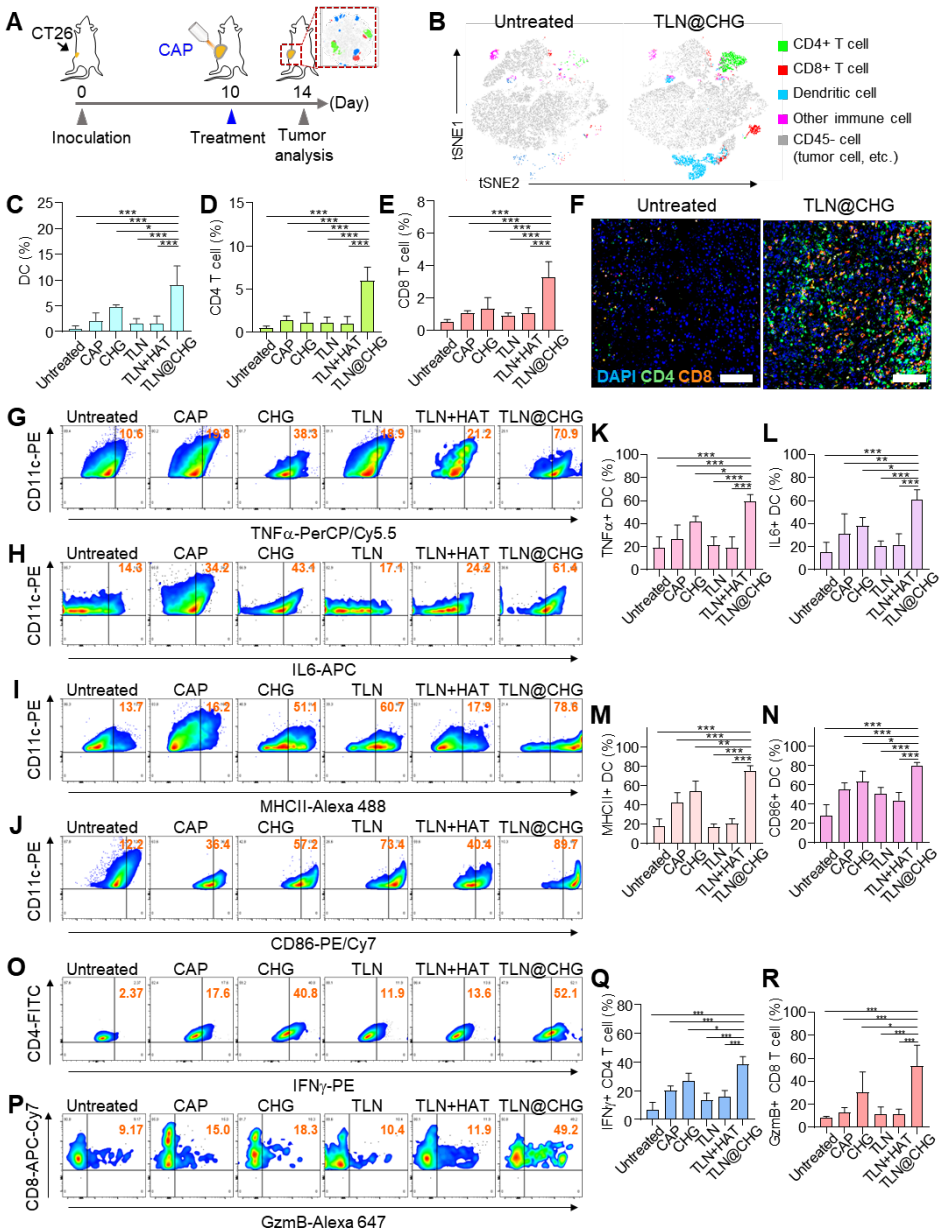

Figure 6. Immune cell profiling of primary tumors under TLN@CHG treatment (A) Schematic illustration of the experiment. (B) t-SNE projection for the analysis of DC, CD4 T cell, and CD8 T cell populations in tumor tissues. (C-E) Proportions of DC (C), CD4 T cells (D), and CD8 T cells (E) in tumor tissues. (F) Immunofluorescence imaging of CD4 and CD8 T cells in tumor tissues. (G-N) Representative flow cytometry plots and frequencies of DC positive for TNFA (G, K), IL6 (H, L), MHCII (I, M), and CD86 (J, N).

(O-R) Representative flow cytometry plots and frequencies of IFNγ-positive CD4 T cells and GzmB-positive CD8 T cells. (***p < 0.001; n.s., not significant)

Tumor immune microenvironment-modulating effects of on-site hydrogel

On-site hydrogel-mediated T cell activation was demonstrated by transcriptome analysis of TLN@CHG-treated tumor cells. Transcript profiles of T cells were obtained from mice treated with TLN@CHG, as compared to untreated mice. Relative gene expression levels were visualized with log2 transformed heat map clusters. TLN@CHG-treated tumor-infiltrating T cells exhibited increased expression levels of cytotoxic CD8 lymphocyte(CTL) phenotype genes including CD8a, eomes, TNFα, IFNγ and granzymes (Fig. 7B). Downregulation of Treg-phenotype genes incuding ID2, STAT5, LAG3, ICOS, CTLA4 and layilin was also observed (Fig. 7C). As TGFβ signaling was blocked by TLN, genes downstream of TGFβ revealed the patterns opposite those seen under TGFβ-induced gene expression under TLN@CHG treatment (Fig. 7D)

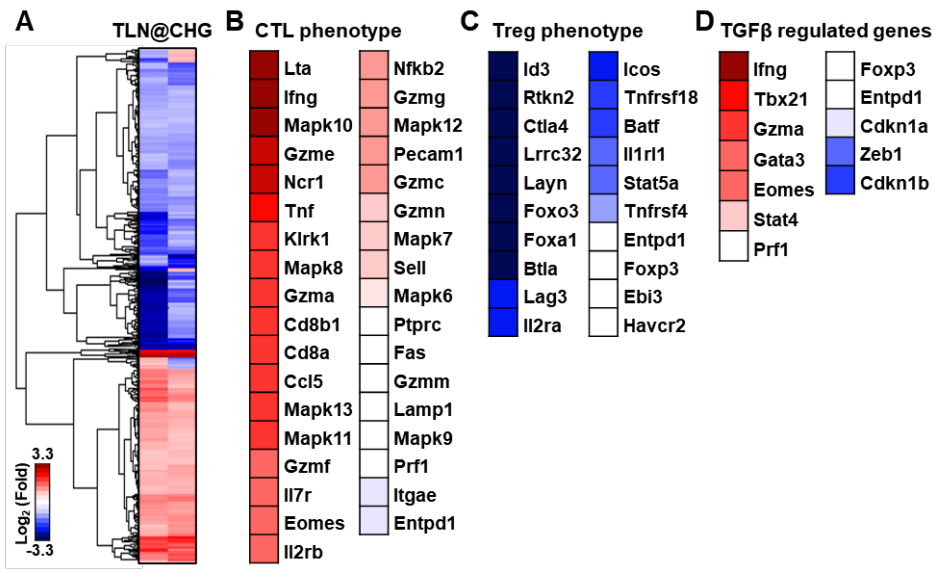

Figure 7. Transcriptome analysis of tumor-infiltrating T cells under TLN@CHG treatment Tumor-infiltrating CD3 T cells were sorted from CT26-bearing mice and RNA-seq analysis was performed. (A) Clustering heatmap for transcripts of tumor-infiltrating CD3 T cells from TLN@CHG-treated versus untreated tumor. (B-D) Heatmaps for differentially expressed genes in TLN@CHG-treated versus untreated tumor. Relative fold changes for transcript expression of CTL phenotype-related genes (B), Treg phenotype-related genes (C), and TGFβ downstream genes (D).

Antigen-specific cytotoxic CD8 T cell-mediated systemic immune response of on-site hydrogel

The mechanism of tumor recurrence prevention was investigated using a CD8 T cell-depletion study. CD8 T cells were depleted from TLN@CHG-treated mice by six repeated anti-CD8 antibody injections given at the indicated time points (Fig. 8A). All CD8 T cell-depleted mice revealed tumor growth (Fig. 8B) and 0% survival by day 60 (Fig. 8C). To evaluate the antigen-specific tumor prevention response, CT26-bearing mice were treated with TLN@CHG, rechallenged with 4T1 or CT26 tumor cells at day 7 after the first inoculation, and monitored for 180 days (Fig. 8D) All mice rechallenged with CT26 cells were alive at 180 days, whereas 0% survival at day 180 was seen among mice rechallenged with 4T1 tumor cells and naïve mice challenged with CT26 tumor cells (Fig. 8E). Complete suppression of tumor growth was observed in all TLN@CHG-treated mice (Fig. 8F, 8G). The survival rate exactly matched the tumor incidence rate. Development of memory effector T cells was observed at day 7 after mice were re-stimulated on day 180 with CT26 tumor cells (Fig. 8H). The percentage of memory effector T cells in the tumor-draining lymph nodes of TLN@CHG-treated mice was significantly higher than that of untreated mice (Fig. 8I).

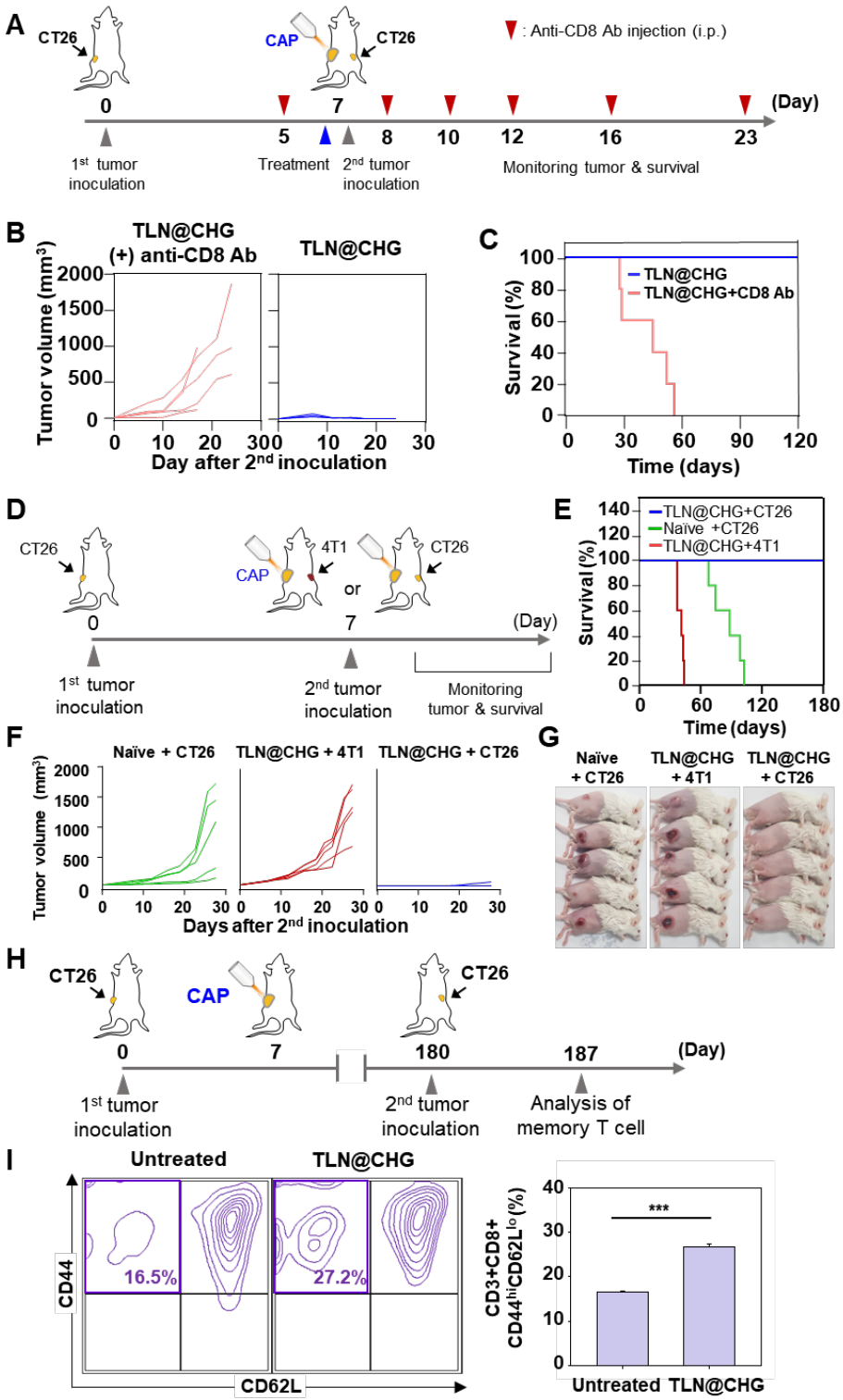

Figure 8. Mechanism study of adaptive immune responses. (A) CT26 tumor-bearing mice received anti-CD8 antibody six times before and after treatment with TLN@CHG, and were rechallenged with a second injection of

tumor cells at day 7. (B) Rechallenged tumors were individually monitored. (C) Survival of mice was monitored over 120 days. (D) TLN@CHG-treated CT26 tumor bearing-mice were rechallenged with CT26 or 4T1 tumor cells at day 7 after the first inoculation of CT26 tumor cells. Naïve mice were inoculated with CT26 cells as a control group. (E) Survival of mice was monitored over 180 days. (F) Tumor growth of mice was observed for 28 days after the second tumor cell inoculation. (G) Appearance of tumor-bearing mice was assessed on day 7 after the second tumor inoculation. (H) TLN@CHG-treated CT26-bearing mice were rechallenged with CT26 tumor cells at day 180 after the first inoculation. (I) Memory T cell populations were analyzed among T cells from tumor-draining lymph nodes. (***$p < 0.001$)

Supplementary Video

Supplementary Video S1. In situ crosslinking of tyramine under CAP irradiation. Tyramine solution was left unirradiated (left) or irradiated with CAP (right). Without CAP irradiation, no color change was observed in the tyramine solution (left). Upon 5 min of CAP irradiation, the tyramine solution (right) turned to a brown color due to the crosslinking of tyramine.

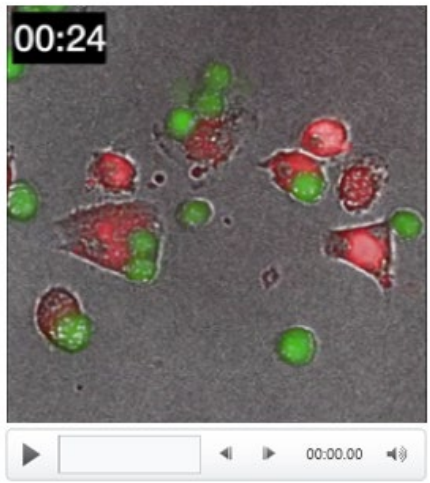

Supplementary Video S2. Phagocytosis of cancer cells by BMDC. Cancer cells (labeled with green dye) were treated with TN@CHG and co-cultured with BMDC (labeled with red dye). The actual time (HH:MM) of phagocytosis is displayed at the top left of the screen.

Supplementary Figures

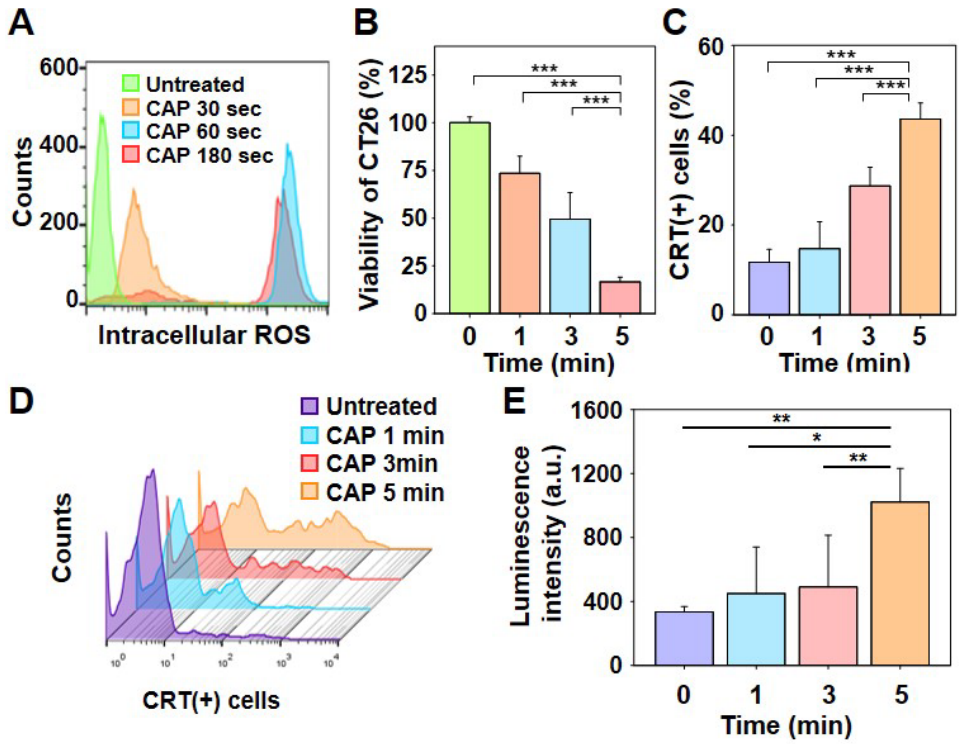

Supplementary Fig. S1. Immunogenic death of tumor cells upon CAP irradiation. CT26 tumor cells were treated with CAP for various periods. The levels of intracellular ROS (A), cell viability (B), and cell surface exposure of CRT (C, D) among CAP-treated cancer cells were analyzed by flow cytometry. (E) ATP secretion by CAP-treated cells was determined by luciferase activity (a.u., arbitrary unit). (*$p < 0.05$; **$p < 0.01$; ***$p < 0.001$)

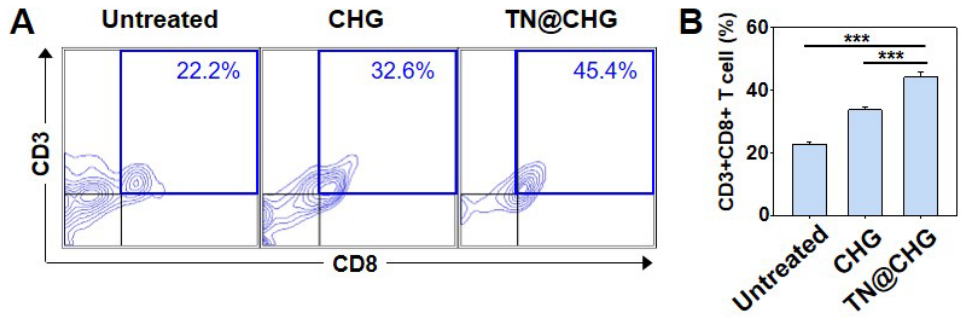

Supplementary Fig. S2. Cytotoxic T cells in tumor microenvironments. CT26-bearing mice were treated with the various formulations at day 7 after tumor inoculation. At day 14 after tumor inoculation, the populations of CD3+CD8+ cells in tumor tissues were analyzed by flow cytometry. (***$p < 0.001$)

4. Discussion

We herein demonstrate that external CAP can be used to induce on-site gelation via ROS generation, and the sustained release of TRKI from TLN@CHG can modulate immunological tumor microenvironments. The generation of ROS from CAP can play dual roles by inducing both gelation and the presence of DAMP signals on tumor cells. TLN@CHG could exert anticancer effects on primary tumors and prevent the growth of distant tumors.

CAP-derived ROS plays an actuating role in the on-site gelation of HAT via the peroxidase-catalyzed polymerization of phenols. This peroxidase-catalyzed polymerization is known to involve three steps: radical formation, radical transfer, and radical coupling [20]. ROS generated from CAP include superoxide anions, hydroperoxyl radicals, hydrogen peroxide, hydroxyl radicals, atomic oxygen, and singlet oxygen in the liquid phase [21]. In recent studies, hydrogen peroxide has been used for crosslinking of hydrogel matrix. In the studies, hydrogen peroxide was directly added to the solutions of polymers such as linear poly(ethylene glycol) [22], HA [13], gelatin [23], and alginate [24]. Unlike those studies using hydrogen peroxide-mediated crosslinking, the use of CAP offers the advantage of inducing hydrogels under mild external conditions without the use of toxic peroxide chemical reagents [25].

The phenolic moiety of HAT is crucial for the on-site formation of hydrogel upon CAP irradiation. In the presence of peroxidase, the phenol moiety is known to crosslink to form a hydrogel network. The formation of hydrogel by phenol residues was reported previously [13,22]. In the prior studies, tyramine residues were introduced to HA [13] and poly(ethylene glycol) [22] to enable hydrogels to form in the presence of hydrogen peroxide. For example, the tyrosine residues of silk protein were utilized as a crosslinking moiety for polymerization by HRP and hydrogen peroxide [26].

In this study, TLN@CHG showed a higher anticancer effect than CHG, supporting the ability of TLN to enhance immunotherapeutic efficacy. The TRKI of TLN is known to block TGFβ/Smad signaling [27]. TRKI inhibits the phosphorylation of TGFβ receptor, and thereby blocks downstream signaling. TGFβ makes an important contribution to the immune-suppressive tumor microenvironment [28] and has been demonstrated to suppress tumor-infiltrating T cells, their differentiation to Th1 T cells, and the antigen-presenting ability of DC [29]. The local release of TRKI from TLN@CHG may therefore contribute to the enhanced recruitment and activation of immune cells, such as DC and T cells.

The use of on-site gelation by CAP irradiation allowed us to entrap cancer cells in the hydrogel network. These entrapped and CAP-irradiated cancer cells may serve as an antigen reservoir. Sustained release of antigen has been reported to enhance immune activation and maintenance [30], such that an “antigen reservoir” effect can improve adaptive anti-tumor immunity [31]. Our hydrogel formulation also maintained the cross-presentation ability of DC for an extended period

In addition to directing on-site gelation, CAP irradiation can evoke the killing effect of cancer cells by ROS. CAP alone has been studied as a new modality for ROS generation-based anti-cancer treatment [21]. ROS-mediated cell death directly kills cancer cells and induces DAMPs on dead cancer cells, thereby exerting an immune-activating effect [32,33]. In addition, many of the limitations of conventional chemotherapy (e.g., chemoresistance, bioavailability, and certain adverse effects) could potentially be overcome through the use CAP anti-cancer technology.

Transcriptome analysis provided further evidence that TLN@CHG treatment was associated with reduction of the Treg phenotype and induction of the CTL phenotype. Because a TGFβ-abundant environment can restrain Th1 polarization [35] and suppress the effector function of CTL via Treg cells [36], the greatly enhanced CTL population in TLN@CHG-treated tumors compared to CHG-treated tumors might be attributed to the ability of TLN to block TGFβ. This modulation of antitumor immunity appears to contribute to the complete tumor ablation of primary tumors seen in TLN@CHG-treated mice.

TLN@CHG offers advantages in terms of its biodegradability, which is provided by its hyaluronic acid backbone. We observed that NP/fBSA@CHG was retained at the injection sited for at least 4 days, and gradually disappeared thereafter. This indicates that CHG undergoes biodegradation, possibly by endogenous hyaluronidase. Hyaluronic acid can be degraded to tetrasaccharide by hyaluronidase [37]. As TLN is composed of phospholipids, which are the main components of cell membranes, the degradation products of TLN and CHG should not be harmful to the body.

Our CAP-induced hydrogel can function for both gelation and removal of the primary tumor. Several studies have studied the use of immunotherapeutic hydrogel after primary tumor surgery [38]. The post-insertion of hydrogel was found to prevent the recurrence of cancer cells after surgical treatment through the sustained release of immunomodulators. Our CAP-formable hydrogel, in contrast, can kill primary tumors without surgery. Moving forward, the local-site injection of HAT mixed with TLN followed by CAP irradiation could potentially replace and improve upon the surgical implantation of hydrogels.

In conclusion, we herein used CAP-induced on site gelation to entrap dying tumor cells and TLN in hydrogel networks. CAP-induced ROS triggered both gelation and immunogenic tumor cell death. The local release of TRKI from TLN@CHG modulated the immunological tumor microenvironment by activating innate effector immune cells. The uptake of ROS-exposed cancer cells by DC and the presentation of tumor antigens to T cells provided protection against secondly challenged distant tumors. Although we used TLN in this study, other immune-modulating agents or nanoadjuvants might be used with CHG to modulate tumor immunological microenvironments.

5. References

[1] Robert C. A decade of immune-checkpoint inhibitors in cancer therapy. Nat Commun. 2020 Jul 30;11(1):3801.

[2] Galluzzi L, Humeau J, Buqué A, Zitvogel L, Kroemer G. Immunostimulation with chemotherapy in the era of immune checkpoint inhibitors. Nat Rev Clin Oncol. 2020 Dec;17(12):725-741.

[3] Rodell CB, Arlauckas SP, Cuccarese MF, Garris CS, Li R, Ahmed MS, Kohler RH, Pittet MJ, Weissleder R. TLR7/8-agonist-loaded nanoparticles promote the polarization of tumour-associated macrophages to enhance cancer immunotherapy. Nat Biomed Eng. 2018 Aug;2(8):578-588.

[4] Li MO, Flavell RA. TGF-beta: a master of all T cell trades. Cell. 2008 Aug 8;134(3):392-404.

[5] Shields CW 4th, Evans MA, Wang LL, Baugh N, Iyer S, Wu D, Zhao Z, Pusuluri A, Ukidve A, Pan DC, Mitragotri S. Cellular backpacks for macrophage immunotherapy. Sci Adv. 2020 Apr 29;6(18):eaaz6579.

[6] Yin Q, Yu W, Grzeskowiak CL, Li J, Huang H, Guo J, Chen L, Wang F, Zhao F, von Boehmer L, Metzner TJ, Leppert JT, Chien YH, Kuo CJ, Davis MM. Nanoparticle-enabled innate immune stimulation activates endogenous tumor-infiltrating T cells with broad antigen specificities. Proc Natl Acad Sci U S A. 2021 May 25;118(21):e2016168118.

[7] Korangath P, Barnett JD, Sharma A, Henderson ET, Stewart J, Yu SH, Kandala SK, Yang CT, Caserto JS, Hedayati M, Armstrong TD, Jaffee E, Gruettner C, Zhou XC, Fu W, Hu C, Sukumar S, Simons BW, Ivkov R. Nanoparticle interactions with immune cells dominate tumor retention and induce T cell-mediated tumor suppression in models of breast cancer. Sci Adv. 2020 Mar 25;6(13):eaay1601.

[8] Pulendran B, S Arunachalam P, O'Hagan DT. Emerging concepts in the science of vaccine adjuvants. Nat Rev Drug Discov. 2021 Jun;20(6):454-475.

[9] Lin AG, Xiang B, Merlino DJ, Baybutt TR, Sahu J, Fridman A, Snook AE, Miller V. Non-thermal plasma induces immunogenic cell death in vivo in murine CT26 colorectal tumors. Oncoimmunology. 2018 Jul 26;7(9):e1484978.

[10] Chen G, Chen Z, Wen D, Wang Z, Li H, Zeng Y, Dotti G, Wirz RE, Gu Z. Transdermal cold atmospheric plasma-mediated immune checkpoint blockade therapy. Proc Natl Acad Sci U S A. 2020 Feb 18;117(7):3687-3692.

[11] Laroussi M. Cold Plasma in Medicine and Healthcare: The New Frontier in Low Temperature Plasma Applications. Front Phys-Lausanne. 2020;8.

[12] Li W, Yang J, Luo L, Jiang M, Qin B, Yin H, Zhu C, Yuan X, Zhang

J, Luo Z, Du Y, Li Q, Lou Y, Qiu Y, You J. Targeting photodynamic and photothermal therapy to the endoplasmic reticulum enhances immunogenic cancer cell death. Nat Commun. 2019 Jul 26;10(1):3349.

[13] Loebel C, Szczesny SE, Cosgrove BD, Alini M, Zenobi-Wong M, Mauck RL, et al. Cross-Linking Chemistry of Tyramine-Modified Hyaluronan Hydrogels Alters Mesenchymal Stem Cell Early Attachment and Behavior. Biomacromolecules. 2017;18(3):855-64.

[14] Lee J, Le QV, Yang G, Oh YK. Cas9-edited immune checkpoint blockade PD-1 DNA polyaptamer hydrogel for cancer immunotherapy. Biomaterials. 2019 Oct;218:119359.

[15] Wu Y, Li Q, Shim G, Oh YK. Melanin-loaded CpG DNA hydrogel for modulation of tumor immune microenvironment. J Control Release. 2021 Feb 10;330:540-553.

[16] Yu T, Gan S, Zhu Q, Dai D, Li N, Wang H, Chen X, Hou D, Wang Y, Pan Q, Xu J, Zhang X, Liu J, Pei S, Peng C, Wu P, Romano S, Mao C, Huang M, Zhu X, Shen K, Qin J, Xiao Y. Modulation of M2 macrophage polarization by the crosstalk between Stat6 and Trim24. Nat Commun. 2019 Sep 25;10(1):4353.

[17] Kundu K, Knight SF, Willett N, Lee S, Taylor WR, Murthy N. Hydrocyanines: a class of fluorescent sensors that can image reactive oxygen species in cell culture, tissue, and in vivo. Angew Chem Int Ed Engl. 2009;48(2):299-303.

[18] Kim D, Wu Y, Li Q, Oh YK. Nanoparticle-Mediated Lipid Metabolic Reprogramming of T Cells in Tumor Microenvironments for Immunometabolic Therapy. Nanomicro Lett. 2021 Jan 4;13(1):31.

[19] Shim G, Ko S, Park JY, Suh JH, Le QV, Kim D, Kim YB, Im GH, Kim HN, Choe YS, Cho J, Kim S, Oh YK. Tannic acid-functionalized boron nitride nanosheets for theranostics. J Control Release. 2020 Nov 10;327:616-626.

[20] Mashhadi N, Taylor KE, Biswas N, Meister P, Gauld JW. Oligomerization of 3-substituted quinolines by catalytic activity of soybean peroxidase as a wastewater treatment. Product formation and computational studies. Chem Eng J. 2019;364:340-8.

[21] Bauer G, Sersenová D, Graves DB, Machala Z. Cold Atmospheric Plasma and Plasma-Activated Medium Trigger RONS-Based Tumor Cell Apoptosis. Sci Rep. 2019 Oct 2;9(1):14210.

[22] Wang D , Yang X , Liu Q , Yu L , Ding J . Enzymatically cross-linked hydrogels based on a linear poly(ethylene glycol) analogue for controlled protein release and 3D cell culture. J Mater Chem B. 2018 Oct 14;6(38):6067-6079.

[23] Thi PL, Lee Y, Tran DL, Thi TTH, Kang JI, Park KM, Park KD. In situ forming and reactive oxygen species-scavenging gelatin hydrogels for enhancing wound healing efficacy. Acta Biomater. 2020 Feb;103:142-152.

[24] Liu J, Fang Q, Lin H, Yu X, Zheng H, Wan Y. Alginate-poloxamer/silk fibroin hydrogels with covalently and physically cross-linked networks for cartilage tissue engineering. Carbohydr Polym. 2020 Nov 1;247:116593.

[25] Bazaka K, Jacob MV, Ostrikov KK. Sustainable Life Cycles of Natural-Precursor-Derived Nanocarbons. Chem Rev. 2016 Jan 13;116(1):163-214.

[26] Choi J, McGill M, Raia NR, Hasturk O, Kaplan DL. Silk Hydrogels Crosslinked by the Fenton Reaction. Adv Healthc Mater. 2019 Sep;8(17):e1900644.

[27] Li S, Luo M, Wang Z, Feng Q, Wilhelm J, Wang X, Li W, Wang J, Cholka A, Fu YX, Sumer BD, Yu H, Gao J. Prolonged activation of innate immune pathways by a polyvalent STING agonist. Nat Biomed Eng. 2021 May;5(5):455-466.

[28] Ju H, Kim D, Oh YK. Lipid nanoparticle-mediated CRISPR/Cas9 gene editing and metabolic engineering for anticancer immunotherapy. Asian J Pharm Sci. 2022 Aug;17(5):641-652.

[29] Batlle E, Massagué J. Transforming Growth Factor-β Signaling in Immunity and Cancer. Immunity. 2019 Apr 16;50(4):924-940.

[30] Xie X, Hu Y, Ye T, Chen Y, Zhou L, Li F, Xi X, Wang S, He Y, Gao X, Wei W, Ma G, Li Y. Therapeutic vaccination against leukaemia via the sustained release of co-encapsulated anti-PD-1 and a leukaemia-associated antigen. Nat Biomed Eng. 2021 May;5(5):414-428.

[31] Rakhra K, Abraham W, Wang C, Moynihan KD, Li N, Donahue N, Baldeon AD, Irvine DJ. Exploiting albumin as a mucosal vaccine chaperone for robust generation of lung-resident memory T cells. Sci Immunol. 2021 Mar 19;6(57):eabd8003.

[32] Yang W, Zhang F, Deng H, Lin L, Wang S, Kang F, Yu G, Lau J, Tian R, Zhang M, Wang Z, He L, Ma Y, Niu G, Hu S, Chen X. Smart Nanovesicle-Mediated Immunogenic Cell Death through Tumor Microenvironment Modulation for Effective Photodynamic Immunotherapy. ACS Nano. 2020 Jan 28;14(1):620-631.

[33] Kim D, Byun J, Park J, Lee Y, Shim G, Oh YK. Biomimetic polymeric nanoparticle-based photodynamic immunotherapy and protection against tumor rechallenge. Biomater Sci. 2020 Feb 21;8(4):1106-1116.

[34] Kim TS, Shin EC. The activation of bystander CD8+ T cells and their roles in viral infection. Exp Mol Med. 2019 Dec 11;51(12):1-9.

[35] van der Leun AM, Thommen DS, Schumacher TN. CD8+ T cell states in human cancer: insights from single-cell analysis. Nat Rev Cancer. 2020 Apr;20(4):218-232.

[36] Lazarova M, Steinle A. Impairment of NKG2D-Mediated Tumor Immunity by TGF-β. Front Immunol. 2019 Nov 15;10:2689.

[37] Varela-Aramburu S, Su L, Mosquera J, Morgese G, Schoenmakers SMC, Cardinaels R, Palmans ARA, Meijer EW. Introducing

Hyaluronic Acid into Supramolecular Polymers and Hydrogels. Biomacromolecules. 2021 Nov 8;22(11):4633-4641.

[38] Chen Q, Wang C, Zhang X, Chen G, Hu Q, Li H, Wang J, Wen D, Zhang Y, Lu Y, Yang G, Jiang C, Wang J, Dotti G, Gu Z. In situ sprayed bioresponsive immunotherapeutic gel for post-surgical cancer treatment. Nat Nanotechnol. 2019 Jan;14(1):89-97.

Chapter 4

Liver fibrosis-activated antifibrotic peptide delivery

1. Introduction

Liver fibrosis is an incurable condition that afflicts millions of patients globally [1]. Cirrhosis, the most common cause of liver fibrosis, is responsible for over 1 million deaths per year [2]. Despite the clear clinical need, therapies for liver fibrosis are limited. Some drugs, including selonsertib, cenicriviroc and simtuzumab, are in clinical trials, but none has yet been approved for treatment of liver fibrosis [3]. Among the various cell types in the fibrotic liver, hepatic stellate cells play a central role in the progression of hepatic fibrogenesis. In response to liver injury, quiescent hepatic stellate cells transdifferentiate into activated hepatic stellate cells (aHSC), which possess fibrogenic properties [4]. aHSC are emerging as therapeutic targets for novel therapies against liver fibrosis [5]. Indeed, liver fibrosis can be ameliorated by reducing the aHSC population or inducing aHSC senescence. Nilotinib, which has been investigated for liver fibrosis therapy, is known to induce autophagic cell death and apoptosis of aHSC [6]. OSU-03012, a celecoxib derivative, has been investigated for its potential to induce senescence of aHSC and promote regression of liver fibrosis [7].

Fibroblast activation protein (FAP), a type II transmembrane glycoprotein, is known to be specifically overexpressed on the surfaces of aHSC in the fibrotic liver. In fact, it has been reported that FAP is exclusively overexpressed in aHSC [8-10]. The active site of FAP, located in an extracellular portion of the protein, cleaves a Pro-Xxx sequence in amino acid bonds. If FAP were used to activate antifibrotic therapy and shown to subsequently reduce the population of abnormally high aHSC in the fibrotic liver, the therapy should be fibrosis-specific. The naturally occurring peptide melittin has been reported to have therapeutic potential by virtue of its antifibrotic properties [11, 12]. Melittin, the principal peptide component of the venom of the honeybee, Apis mellifera, exhibits strong, non-specific lytic activity against lipid components of cell membranes. Although melittin can be effective in reducing aHSC populations in fibrotic liver tissues, clinical application of melittin against fibrotic diseases has been limited owing to its non-specific actions, which result in systemic toxicity. A specific activation system that enabled melittin to act only in fibrotic tissue would represent a significant repurposing of melittin.

In this study, we tested the hypothesis that FAP-selective liberation of the antifibrotic peptide, melittin, on the surfaces of FAP-overexpressing aHSC provides a targeted antifibrotic effect in the liver. To this end, we designed a delivery system in which promelittin is cleaved only in FAP-expressing (i.e., fibrotic) regions of the liver, resulting in melittin release into the fibrotic liver microenvironment. To enhance liver delivery and stability in the bloodstream, we further tethered promelittin onto the surfaces of PEGylated liposomes. Here, we report the antifibrotic and survival-prolonging effects of promelittin-tethered liposomes in three different in vivo liver fibrosis mouse models: the bile duct-ligation (BDL), carbon tetrachloride-induced, and high-fat diet-induced models.

2. Materials and methods

Preparation of promelittin peptide-modified liposomes

Liposomes surfaces were modified with promelittin peptide by covalently tethering the Cys-promelittin peptide, which sequence is N-CEPEAEADAEAGPAGIGAVLKVLTTGLPALISWIKRKRQQ-C, via a maleimide reaction. After being cleaved by FAP, EPEAEADAEAGPA-melittin peptide could be separated into EPEAEADAEAGP and A-melittin, as previously reported [43]. Liposomes were prepared by mixing egg L-α-phosphatidylcholine (PC; Avanti Polar Lipids, Alabaster, AL, USA), egg L-α-phosphatidyl DL-glycerol (PG; Avanti Polar Lipids), cholesterol (Chol; Sigma-Aldrich), and 1,2-distearoyl-sn-glycero-3-phosphoethanolamine-N-[maleimide(polyethylene glycol)-2000] (mal-PEG-DSPE; Avanti Polar Lipids) at a molar ratio of 2:2:2:0.4 in chloroform. For comparison, 1,2-distearoyl-sn-glycero-3-phosphoethanolamine-N-[(polyethylene glycol)-2000] (PEG-DSPE; Avanti Polar Lipids) was used in place of mal-PEG-DSPE in some experiments. After removal of chloroform using a rotary evaporator, the resulting thin lipid films were hydrated with 1 mL of phosphate-buffered saline (PBS; pH 7.4), vortexed, and extruded three times through 0.2-μm polycarbonate membrane filters (Millipore Corp., Billerica, MA, USA). This process resulted in maleimide-activated, PEGylated liposomes (ML) or plain PEGylated liposomes (PL). The resulting ML were further used to prepare promelittin-modified liposomes (PRL). For preparation of PRL, 0.8 μmol cys-promelittin (Peptron, Daejeon, Republic of Korea) was mixed with 1 mL of ML containing 0.4 μmol of mal-PEG-DSPE. The cysteine in the peptide was reacted with maleimide groups of ML by incubating at room temperature for 6 h.

In some experiments, a scrambled cys-promelittin sequence (N-CEAGAEPAA EPKPATSGDILWVLAARLTVLIGEQKQKRIG-C) or a promelittin-mimicking fluorescence-quenched peptide [CEPEAEADA-E (fluorophore)-AGPAGIGAVLK-quencher], was linked to the surface of ML, resulting in scrambled cys-promelittin peptide-tagged liposomes (SCL) and promelittin-mimicking fluorescence-quenched peptide-tagged liposomes (FQL), respectively. This latter dual-modified promelittin-mimicking peptide, containing 5-[(2-aminoethyl) amino]naphthalene-1-sulfonic acid (EDANS) as a fluorophore and 4-((4-(dimethylamino) phenyl)azo)benzoic acid (DABCYL) as a quencher, was prepared as illustrated in Figure 2G. The EDANS-DABCYL–linked promelittin-mimicking peptide was tethered to the surface of ML containing 0.4 μmol of mal-PEG-DSPE. The resulting FQL were purified from unreacted peptides by chromatography on a PD-10 column (GE Healthcare Life Science, Cat. No. 17-0851-01, Mickleton, NJ, USA) and stored at 4°C until use. FAP-sensitive cleavage of promelittin peptide on liposomes was tested by monitoring fluorescence recovery of the quenched fluorophore.

Quantification of peptides on liposomes

The amount of peptides on liposomes was assayed using fluorescamine, a heterocyclic dione that reacts with primary amines of peptides. Specifically, an aliquot (32 μL) of fluorescamine solution (Sigma, cat. No. F-9015; 3 mg/mL in acetonitrile) was added to 100 μL of peptide-conjugated liposomes, and the mixture was allowed to react at room temperature for 10 min. The fluorescence intensity of fluorescamine-labeled liposomes was assessed at an excitation wavelength of 365 nm and an emission wavelength of 470 nm using a SpectraMAX M5 Multi-Mode Microplate Reader (Molecular Devices, San Jose, CA, USA). For calculation of peptides on liposomes, a standard curve was generated using serial dilutions of a cys-promelittin standard solution. The amount of phospholipids in liposomes was determined using a phosphate assay [Anderson et al., 1982].

Characterization studies

Liposomes were characterized by size, zeta potential, and morphology. The size and zeta potential of various liposome preparations were measured using dynamic light scattering and laser-Doppler micro-electrophoresis, respectively. The hydrodynamic diameters of liposomes were measured at an angle of 90° at 24.1°C using a HeNe laser (10 mW) and an ELS-8000 dynamic light-scattering instrument (Photal, Osaka, Japan). Zeta potential was measured at an angle of 22°. Data were analyzed using the ELS-8000 software package supplied by the manufacturer. Transmission electron microscopy (TEM) images were acquired using a Talos L120C TEM system (FEI, Brno, Czech) operating at 120 kV. Liposomes were loaded onto a 300-mesh copper grid coated with formvar-carbon (01753-F; Ted Pella, Redding, CA, USA). The grid was washed twice with distilled water and then negative-stained with 1% (w/v) uranyl acetate, after which images of negatively stained liposomes were obtained.

Stability test

The stability of liposomes was monitored up to 18 days in the presence and absence of FAP (5 nM). For 18 days, liposomes were stored with or without FAP at 4°C or room temperature. The hydrodynamic diameters of liposomes were measured 3 day intervals using an ELSZ-1000 instrument (Otsuka Electronics Co.)

FAP-mediated fluorescence recovery test

The cleavage activity of FAP towards promelittin sequences was tested using the quenching and dequenching feature of the promelittin-mimicking fluorescence-quenched peptide on FQL. FQL (0.9 mg phospholipid/mL) were incubated with 1 μM FAP or matrix metalloproteinase 9 (MMP9; R&D Systems Inc.) at 37°C for 1 h. Recovery of the fluorescence of EDANS liberated from the nearby quencher DABCYL was assessed by fluorometry at an excitation wavelength of 335 nm and an emission wavelength of 490 nm using a SpectraMAX M5 system (Molecular Devices).

Hemolysis assay

The hemolysis activity of various liposomes was tested using mouse red blood cells (RBCs). RBCs (2 x 104 cells/mL) were isolated from Balb/c mice and incubated with various liposome preparations in the absence or presence of 1 μM FAP. RBCs treated with 1% Triton X-100 served as a 100% hemolysis positive control, and a suspension of RBCs in PBS was used as a negative control. After centrifuging samples at 1000 x g for 10 min, supernatants containing hemoglobin released from lysed RBCs were transferred to a clear, flat-bottomed, 96-well polystyrene plate (SPL Life Sciences, Pocheon, Republic of Korea). The percentage of hemolysis was calculated by measuring the absorbance of each sample at 540 nm using a SpectraMax Plus plate reader (Molecular Devices).

Release kinetics of PRL

To evaluate the release kinetics of melittin by FAP, PRL (0.9 mg phospholipid/mL) was incubated without or with 5 nM of FAP. At various time points, the released melittin was separated from PRL by filtration with a 50-kDa membrane filter (Millipore, Billerica, MA, USA). The amounts of released melittin were measured using a fluorescamine assay.

FAP-mediated release kinetics of DABCYL-modified peptides from FQL

To evaluate the FAP-mediated release kinetics of fluorescent melittin from FQL, we incubated FQL (0.9 mg phospholipid/mL) without or with 5 nM of FAP or matrix metalloproteinase 9 (MMP9; R&D Systems, Inc.) at 37°C for various periods. The recovery of fluorescence representing EDANS-labeled melittin peptide liberated from FQL was assessed by fluorometry at an excitation wavelength of 335 nm and an emission wavelength of 490 nm using a SpectraMAX M5 system (Molecular Devices).

Cell culture

LX-2 human hepatic stellate cells (kindly provided by Professor Sang Geon Kim, College of Pharmacy and Research Institute of Pharmaceutical Sciences, Seoul National University, Republic of Korea) and FAP-negative Chang cells (kindly provided by Professor Mi-Ock Lee, College of Pharmacy and Research Institute of Pharmaceutical Sciences, Seoul National University, Republic of Korea) were used for testing FAP-mediated cleavage of peptides on various liposome preparations. Cells were cultured in Dulbecco's modified Eagle medium (DMEM) supplemented with 10% fetal bovine serum (FBS), 100 units/mL of penicillin and 100 μg/mL of streptomycin at 37°C in a humidified 5% CO2 atmosphere. For activation, LX-2 cells were stimulated with TGF-β1 (transforming growth factor-□1) (10 ng/ml; GenScript Biotechnology, Nanjing, China) for 24 h. In some experiments, LX-2 cells treated with or without small interfering RNA (siRNA) targeting FAP (siFAP) were seeded onto 6-well plates (SPL Life Sciences, Pocheon, Republic of

Korea) at a density of 4 × 105 cells/well and then incubated for 24 h to ~80% confluence.

Assessment of siFAP efficiency

The efficiency of siFAP was assessed by measuring the expression levels of FAP using flow cytometry. LX-2 cells were cultured in DMEM supplemented with 10% FBS, 100 units/mL of penicillin, and 100 μg/mL of streptomycin. LX-2 cells (4 × 105 cells/well) were seeded to a 6-well plate (SPL Life Sciences), incubated for 24 h, and transfected for 20 min with 50 nM siFAP (Bioneer Corporation, Daejeon, Republic of Korea) complexed with 5 μL of Lipofectamine 2000. The sequences of siFAP were 5'-CUC UAU GCA GUG UAU CGA AdTdT-3' (sense) and 5'-UUC GAU ACA CUG CAU AGA gdTdT-3' (antisense). In some experiments, scrambled-sequence siRNA (siSCR) was used as a control. After transfection, cells were incubated for an additional 48 h. Next, cells were stained with a rabbit anti-FAP primary IgG antibody (1:50, Abcam) for 1 h, followed by an allophycocyanin-conjugated goat anti-rabbit IgG antibody (1:100, Abcam). After staining, cells were analyzed via BD LSR Fortessa (BD Bioscience). Control cells were stained with rabbit IgG isotype antibody (1:50, Abcam) followed by an allophycocyanin-conjugated goat anti-rabbit IgG antibody (1:100, Abcam).

MTT assay

Cell viability after treatment with various liposome preparations was assessed by MTT [3-(4,5-dimethylthiazol-2-yl)-2,5-diphenyltetrazolium bromide] assay. Briefly, LX-2 cells were seeded onto 24-well plates at a density of 6 × 104 cells/well. After cells reached 70% confluence, they were treated with various liposome preparations for 24 h. MTT solution (500 μM) was then added to each well and plates were incubated for 2 h. The medium was then aspirated and 200 μL of dimethyl sulfoxide (DMSO; Sigma-Aldrich) was added to dissolve formazan crystals generated by metabolically active (live) cells. The viability of cells was quantified by measuring optical density at 570 nm using a microplate reader (Tecan Group Ltd., Seestrasse, Mannedorf, Switzerland).

Animals

Eight-week-old Balb/c mice and C57BL/6 mice (Raon Bio Co., Gyeonggi-do, Republic of Korea) were used for in vivo experiments. All animals (n = 5 mice per group) were maintained and used in accordance with Guidelines for the Care and Use of Laboratory Animals of the Institute of Laboratory Animal Resources, Seoul National University (Seoul, Republic of Korea; approved animal experimental protocol number, SNU-130129-3-1).

Establishment of the bile duct-ligation model

Liver fibrosis was induced in mice by performing BDL surgery under anesthesia (isoflurane 1.5%) as described previously [36] with slight

modifications. Briefly, the surgical area was shaved and cleaned preoperatively using a povidone-iodine solution, then an incision was made in the upper midline and the bile duct was exposed using a wet swab. The bile duct was ligated with silk thread knots at two sites and then cut between the knots, after which the abdominal wall was closed using nonabsorbable silk thread. On days 1 and 3 after BDL surgery, mice were intravenously injected with various liposome preparations.

In vivo efficacy test in carbon tetrachloride induced liver fibrosis model

To test the in vivo antifibrotic effect of PRL, the CCl4-induced chronic liver fibrosis model was established. Eight-week-old female C57BL/6 mice were intraperitoneally injected with CCl4 1 ml/kg (25% CCl4 in olive oil) twice a week for 6 weeks [16]. The liver fibrosis-bearing mice were then intravenously treated with the various liposomes every other day for 2 weeks and sacrificed at 2 weeks after the first treatment. Blood and liver tissues were collected for further analysis. To test the in vivo antifibrotic effect of PRL in an earlier phase of the CCl4-induced liver fibrosis model, 8-week-old female C57BL/6 mice were intraperitoneally injected with CCl4 at 1 ml/kg (25% CCl4 in olive oil) twice a week for 4 weeks. The liver fibrosis-bearing mice were then intravenously treated with PRL every other day for 2 weeks and sacrificed at 4 weeks after the first PRL treatment. Liver tissues were collected for analysis.

In vivo efficacy test in high fat diet-induced liver fibrosis model

The high fat diet-induced liver fibrosis model was established by being fed with a choline-deficient, L-amino acid-defined high-fat diet (CDAHFD, Research Diets, Inc. New Brunswick, NJ, USA) for 10 weeks. The mice were then treated with the various liposomes (dose = 0.27 mg phospholipid/mouse) every other day for 2 weeks and sacrificed 1 day after the last treatment. Blood and liver tissues were collected for further analysis.

FAP expression analysis by flow cytometry

FAP expression on aHSC of liver tissues was analyzed via flow cytometry. Single-cell suspensions of liver tissue were obtained as previously described with slight modification treatment [4]. Briefly, liver tissues were perfused with HEPES buffer (Sigma-Aldrich; cat. No. H4034) containing collagenase D (Sigma-Aldrich; cat. No. C5138-1G) and pronase (Sigma-Aldrich), and digested with stirring at 37°C for 30 min. Cells were collected by centrifugation at 580 xg for 10 min, and dead cells were excluded using a Zombie Red Fixable Viability Kit (BioLegend). The cells were then stained with PE/Cyanine7-conjugated rat anti-mouse CD26 antibody (BioLegend; cat. No. 137810), PE-conjugated rat anti-mouse CD31 antibody (BioLegend; cat. No. 102407, Lot. No. B261070), PerCP/Cy5.5-conjugated rat anti-mouse CD45 antibody (BioLegend; cat. No. 103132, Lot. No. B282872), and rabbit anti-mouse FAP antibody (Abcam; cat. No. ab28244, Lot No. GR217381-54)

for 1 hr at 4°C. Secondary antibody staining was performed with Alexa Fluor 647-conjugated goat anti-rabbit IgG antibody (Abcam; cat. No. ab150083, Lot No. GR3370563-1) for 30 min at 4°C. The HSC population was gated as CD26-CD31-CD45-VitA+ cells using FACS; quadrants for FAP+ HSC were selected relative to the fluorescence minus one (FMO) control.

Molecular imaging

The organ distribution of FQL was determined by molecular imaging. Five days after BDL surgery, BALB/c mice (5 mice per group) were intravenously injected with FQL at a dose of 0.27 mg phospholipid/mouse. One hour later, vital organs (i.e., liver, heart, lung, spleen, and kidney) were isolated and their fluorescence intensities were assessed using an In Vivo Imaging System (IVIS; PerkinElmer, Inc., Hopkinton, MA, USA) (n = 5 samples per group).

Assay of collagen in liver tissue

The amount of collagen in liver tissues was determined by measuring the content of hydroxyproline (HDP) using a Hydroxyproline assay kit (Abcam, Cambridge, UK) as described by the manufacturer. Briefly, 4 days after BDL surgery, mice treated with various formulations were sacrificed and their liver tissues were extracted and homogenized. The homogenate was then treated with 10N NaOH, incubated at 120°C for 1 h, and neutralized with 10N HCl. After centrifugation at 10,000 x g for 5 min, the supernatant was added to wells of a 96-well plate and dried at room temperature. The resulting crystalline residue was dissolved with 0.1 mL of oxidation-buffered chloramine T solution and incubated at room temperature for 20 min. After addition of 50 μL of acidic developer solution, provided in the kit, the plate was incubated at 65°C for 45 min and treated with 50 μL of the provided DMAB solution. Absorbance was measured at 540 nm using a SpectraMax Plus plate reader (Molecular Devices).

In vivo assessment of liver function

The antifibrotic effects of liposomes were tested in vivo using a hematological parameter assay and histological staining. BDL surgery was performed on 8-wk-old female Balb/C mice (Raon Bio). On days 1 and 3 after BDL surgery, mice were intravenously administered liposomes at a phospholipid dose of 2.7 mg/mL. Four days after BDL surgery, blood samples were collected and assayed for alanine transaminase (ALT), aspartate transaminase (AST), bile acid and total bilirubin levels by the Neodin VET Diagnostics Institute (Seoul, Republic of Korea). For histological assessment of liver tissues, the liver was extracted 4 days after BDL surgery, fixed in 10% formalin for 48 h, and paraffin-embedded. The tissues sections were analyzed with hematoxylin and eosin (H&E) staining, and Masson's trichrome staining. For H&E staining, tissue sections were immersed in filtered Harris hematoxylin for 10 sec and then in eosin for 30 sec. The percentage of

connective tissue areas in fibrotic regions on stained slides was calculated using a Vectra 3.0 Automated Quantitative Pathology Imaging System (PerkinElmer, Inc., Hopkinton, MA, USA). Images were analyzed using the InForm 2.2. software (PerkinElmer, Inc.).

Immunohistochemistry of liver tissues

FAP expression on aHSC in the liver was evaluated with immunofluorescent staining of formalin-fixed paraffin-embedded tissues. Liver tissues were sectioned at 4-μm thickness, de-paraffinized with xylene, and rehydrated with an ethanol series. Tissue slides were incubated with a Target Retrieval Solution (pH 6.0) (Agilent Dako, Santa Clara, CA, USA). After being washed, the slides were incubated with 0.1% Triton-X 100, blocked with 10% goat serum in PBS, and stained overnight at 4°C with rabbit anti-mouse FAP antibody (Abcam; cat. No. ab28244, Lot No. GR217381-54) and mouse anti-mouse alpha-smooth muscle actin (αSMA) antibody (Abcam; cat. No. ab7817, Lot No. GR3356520-4). Alexa Fluor 594-conjugated goat anti-mouse IgG antibody (BioLegend; cat. No. 405326, Lot. No. B324994) and Alexa Fluor 647-conjugated goat anti-rabbit IgG antibody (Abcam; cat. No. ab150083, Lot No. GR3370563-1) were applied for 1 hr at room temperature, and the slides were imaged using a Thunder imager 3D assay (Leica Microsystems GmbH, Wetzlar, Germany).

Populations of cells in the liver tissues were analyzed via immunohistochemistry using various cell markers. Fibrosis-induced mice were treated with various liposomes. One day after liposome treatment, mice were anesthetized using isoflurane and the liver was perfused via the vena cava with 30 mL of PBS, and then collected. Excised liver tissues were fixed in 4% paraformaldehyde for 48 h at 4°C. After dehydration in 30% sucrose solution overnight, liver tissues were embedded in OCT compound (Sakura Finetek, Japan) and frozen at -80°C. Frozen liver sections (8 μm thickness) were blocked with 10% goat serum (Abcam, Cambridge, UK) and stained with primary antibodies overnight at 4°C. Alexa Fluor 594 rabbit anti-mouse alpha-smooth muscle actin (αSMA) antibody (Cell Signaling Technology, Danvers, MA, USA; cat. No. 36110S), phycoerythrin (PE)-conjugated rat anti-mouse F4/80 antibody (BioLegend, San Diego, CA, USA; cat. No. 123110), allophycocyanin (APC)-conjugated rat anti-mouse CD26 antibody (BioLegend; cat. No. 137807), PE-conjugated rat anti-mouse CD31 antibody (Invitrogen, Waltham, MA, USA; cat. No. 12-0311-82), and rabbit anti-mouse cytokeratin 7 antibody (Abcam; cat. No. ab181598) were used as markers of HSCs, macrophages, hepatocytes, endothelial cells, and cholangiocytes, respectively.

After secondary antibody staining, tissues were counterstained with DAPI and examined by a VECTRA tissue analyzer (PerkinElmer, Inc.). Image analysis was applied using the InForm 2.2.1 image analysis software (PerkinElmer, Inc.).

qRT-PCR for analysis of cell types

Populations of cells in the liver tissues were also evaluated by running qRT-PCR. Total RNA was extracted from liver tissue using the TRIzol reagent (Invitrogen) and reverse-transcribed into cDNA by incubating at 42°C for 60 min and 70°C for 5 min using RT PreMix (Intron Biotechnology Inc., Seoul, Republic of Korea). The sequences of primers for qRT-PCR are listed in supplementary Table 1. qRT-PCR was performed at Applied Biosystems 7500 Fast Real-Time PCR System (Thermo Fisher Scientific, Waltham, MA, USA) using TOPreal qPCR 2x premix (Enzynomics, Daejeon, Republic of Korea, cat. No. RT501M). The housekeeping gene, glyceraldehyde-3-phosphate dehydrogenase, was used for normalization of each mRNA expression level.

Terminal deoxynucleotidyl transferase dUTP nick end labeling (TUNEL) assay

To evaluate apoptosis of cells in liver tissues, the TUNEL assay was performed. In brief, frozen liver tissue sections (8 μm thickness) were stained with a DeadEnd™ Fluorometric TUNEL System (Promega) according to the manufacturer's protocols. To identify the types of TUNEL-positive apoptotic cells, immunofluorescence staining was sequentially done using markers for various cells. Alexa 594-conjugated anti-αSMA antibody, PE-conjugated anti-F4/80 antibody, and APC-conjugated anti-CD26 antibody were used to mark aHSC, macrophages, and hepatocytes, respectively. After overnight incubation at 4 °C, DAPI staining and mounting were performed on the slides and fluorescence images of slide were obtained by VECTRA(PerkinElmer, Inc.). Then, images were analyzed by InForm 2.2.1 image analysis software (PerkinElmer, Inc.) followed by quantification of co-localization of TUNEL signals with each cell marker.

Safety study

To evaluate the toxicity of PRL, a survival study was conducted in normal mice. Eight-week-old BALB/c mice received repeated intravenous administrations of PL or PRL at a dose of 0.27 mg phospholipid/mouse. Mice were administered with PL or PRL four times over 2 weeks. The survival and body weight of mice were monitored over 60 days.

Statistics

Experimental data were statistically analyzed by two-sided, one-way analysis of variance (ANOVA) using a post hoc Student-Newman-Keul test. All statistical analyses were performed using SigmaStat software (version 12.0, Systat Software, Richmond, CA, USA). A P-value less than 0.05 was considered statistically significant.

3. Results

FAP-specific activation of PRL

PRL and various other liposome formulations, including PL, ML, SCL and FQL, are schematically depicted in Figure 1A. PRL were constructed by tethering cys-promelittin in which a cysteine residue was added to the C-terminus of promelittin to the surface of ML (Fig. 1A). Promelittin has a FAP-cleavable peptide sequence located at the N-terminus of mature melittin. The proposed working mechanism of PRL is illustrated in Figure 1B. Promelittin in PRL is cleaved by FAP on aHSC, releasing melittin. The liberated melittin creates pores in nearby aHSC, thereby reducing the aHSC population in fibrotic tissues and ultimately resulting in a decrease in collagen fibers and regression of fibrosis.

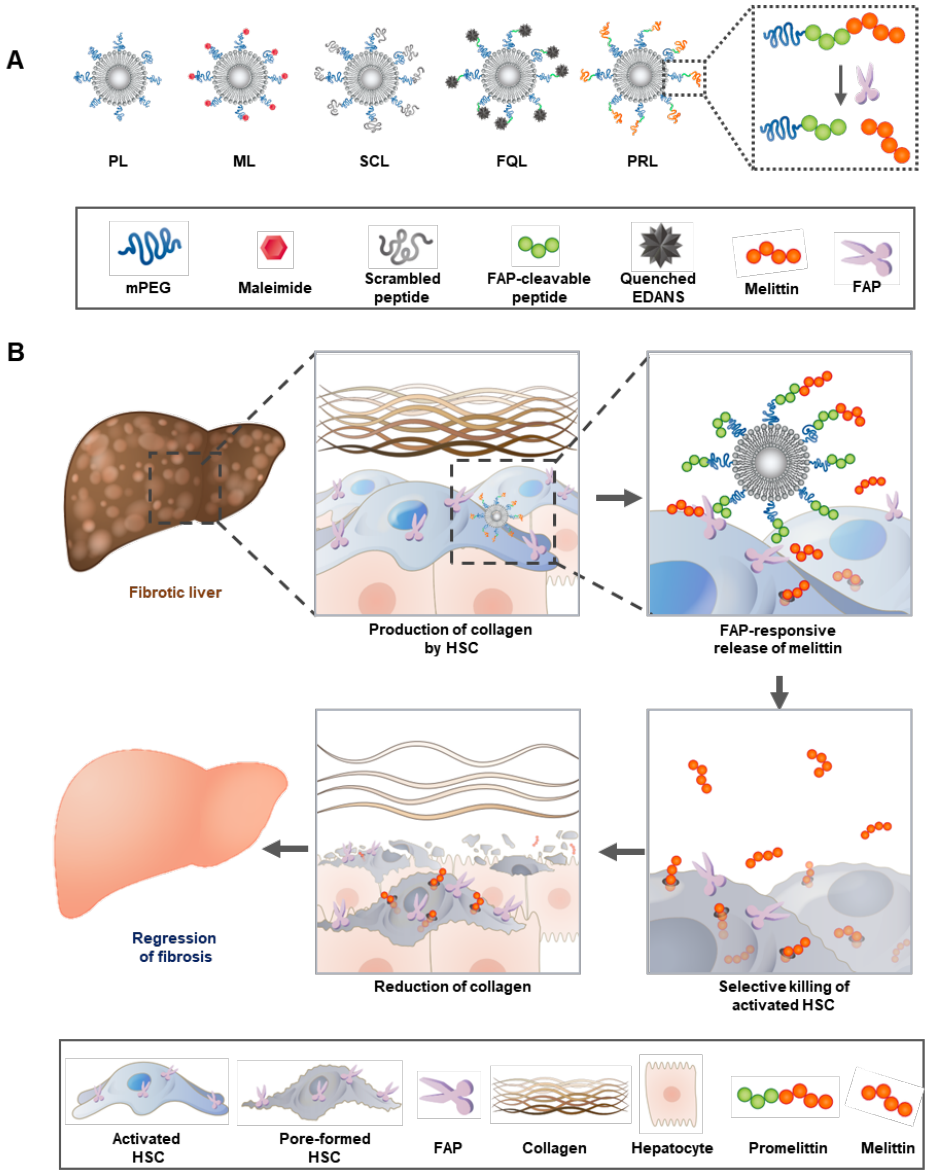

Figure 1. Proposed working mechanism of PRL against liver fibrosis. (A) Schematic illustration of various liposome formulations. FAP-responsive PRL were synthesized by linking cys-promelittin onto the surface of ML. (B) In a fibrotic microenvironment, the promelittin moiety on PRL is cleaved by FAP on aHSC. FAP-mediated cleavage of promelittin on PRL releases melittin, which diffuses to nearby aHSC, creating pores in their cell membranes. The resulting reduction in the number of aHSC in fibrotic tissues leads to decreased production of collagens and regression of fibrosis.

TEM images revealed that PRL adopted a spherical shape (Fig. 2A). Surface modification of ML with cys-promelittin or scrambled peptide did not significantly affect the size of liposomes (Fig. 2B). Zeta potentials of SCL and PRL increased slightly after peptide conjugation (Fig. 2C), but peptide-

to-phospholipid ratios did not differ significantly between PRL and SCL (Fig. 2D). The stability of liposomes was not affected by FAP. During the 18-day study period, none of the liposomes showed a significant size change, regardless of FAP or storage temperature (supplementary Fig. 2). Although the physicochemical features of PRL did not differ from those of SCL, the two formulations differed in their biological responsiveness to the FAP enzyme. In the absence of FAP, there was no hemolysis of RBCs regardless of liposome type (Fig. 2E). However, PRL, but not other liposome formulations, showed RBC hemolysis in the presence of FAP (Fig. 2F). The release of melittin from PRL was observed in the presence of FAP, but not in the absence of FAP (Fig. 2G). In the presence of FAP, the release of melittin from PRL linearly increased up to 12 h of incubation, when it reached 90.7% release. After 24 h of incubation, 99.6% release was observed.

FAP-specific cleavage of promelittin on PRL was further tested by monitoring the recovery of quenched fluorescence of FQL in the presence of FAP. The fluorescence intensity of FQL, dually modified with the fluorophore EDANS and quencher DABCYL, is quenched by FRET. Cleavage of promelittin by FAP disrupts the EDANS and DABCYL interaction and recovers the fluorescence of EDANS (Fig. 2H). Treatment with MMP did not significant change the fluorescence intensity of FQL (Fig. 2I). In contrast, FAP treatment substantially enhanced FQL fluorescence, increasing the fluorescence intensity of FQL at 490 nm by 31.3-fold compared with no-FAP controls (Fig. 2J). The release of fluorescent melittin from FQL was observed in the presence of FAP, but not in the absence of FAP or in the presence of MMP (Fig. 2K). In the presence of FAP, the release of fluorescent melittin gradually increased with time. More than 50% release was observed within 4 h of incubation with FAP. After 12 h of incubation, 92.6% of the fluorescent melittin had been liberated from FQL.

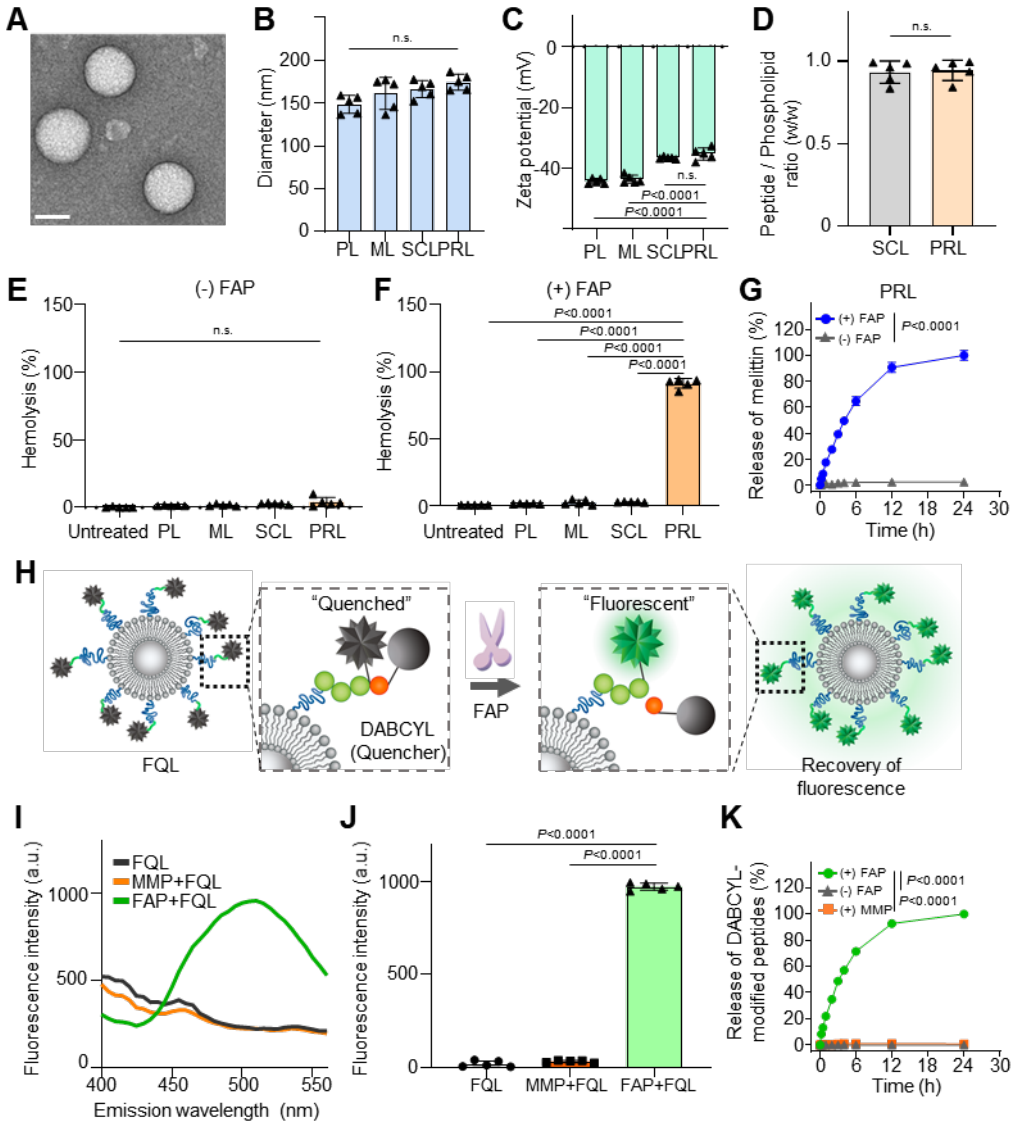

Figure 2. FAP-specific cleavage of promelittin peptide on PRL. (A) Transmission electron microscopy (TEM) imaging. TEM images of liposomes, obtained using a Talos L120C TEM system operating at 120 kV. Scale bar: 100 nm. (B) Size measurements. Liposomes size was measured using dynamic light scattering (n = 5 samples per group). (C) Zeta potential measurements. Zeta potential of liposomes was measured by electrophoretic light scattering (n = 5 samples per group). (D) Peptide-to-phospholipid ratios were estimated using fluorescamine and phosphate assays (n = 5 samples per group). (E, F) The hemolytic activity of PRL against mouse RBCs was evaluated using hemolysis assays (n = 5 samples per group). (G) Release kinetics of melittin from PRL. PRL was incubated with or without FAP for various periods. The release of melittin at each point was measured by fluorescamine assay (n = 5 samples per group). (H) Design of promelittin-

mimicking fluorescence-quenched peptide-tagged liposomes (FQL). A fluorescent FRET (fluorescence resonance energy transfer) moiety was attached to the promelittin-mimicking peptide containing a FAP-dependent cleavage site, and the FAP-specific activity of the peptide was determined by assessing FAP-responsive fluorescence. (I) Fluorescence emission spectra of FQL observed after FAP or MMP treatment. (J) Mean fluorescent intensity of FQL at an emission wavelength of 490 nm (n = 5 samples per group). (K) Release kinetics of DABCYL-modified peptides from FQL. FQL was incubated in the absence or presence of FAP, or in the presence of MMP. The release of DABCYL-modified peptides was evaluated via spectrofluorometry (n = 5 samples per group).

FAP-specific responsiveness of PRL to aHSC

Having demonstrated the responsiveness of PRL to FAP in a cell-free setting, we next assessed PRL responsiveness to aHSC using the human LX-2 hepatic stellate cell line as a model system. In these experiments, LX-2 cells or Chang cells, used as a FAP-negative control cell, were treated with various liposome formulations, and cleavage of liposomal promelittin by FAP on cells was assessed by monitoring recovery of quenched EDANS fluorescence. Flow cytometry data show that the treatment of LX-2 cells with FAP-specific siRNA (siFAP) significantly decreased the expression of FAP (Fig. 3A, 3B). In siFAP-treated cells, the expression level of FAP was silenced by 96.3% compared to that in untreated cells (Fig. 3C). Confocal imaging was used to further visualize the silencing of FAP protein in LX-2 cells (Fig. 3D). Following treatment with FQL, Chang cells showed no change in fluorescence intensity, whereas siFAP-pretreated LX-2 cells showed little change in fluorescence. In contrast, treatment of LX-2 cells with FQL induced a substantial increase in fluorescence (Fig. 3E), indicating effective cleavage of promelittin and recovery of EDANS fluorescence.

Using MTT assays to assess cell viability following treatment with various liposome formulations, we found that PL, ML, and SCL had no effect on the viability of Chang cells, LX-2 cells, or siFAP-treated LX-2 cells (Fig. 3F). Although PRL also had no significant effect on the viability of Chang cells or siFAP-treated LX-2 cells, they significantly affected the viability of LX-2 cells, reducing it to less than 40% (Fig. 3F). Fluorescence live/dead cell staining confirmed these effects, showing that Chang cells (Fig. 3G) and siFAP-treated LX-2 cells (Fig. 3H) retained full viability follow treatment with liposomes, regardless of liposome type, whereas only treatment of LX-2 cells with PRL resulted in an increase in the dead cell population (Fig. 3I).

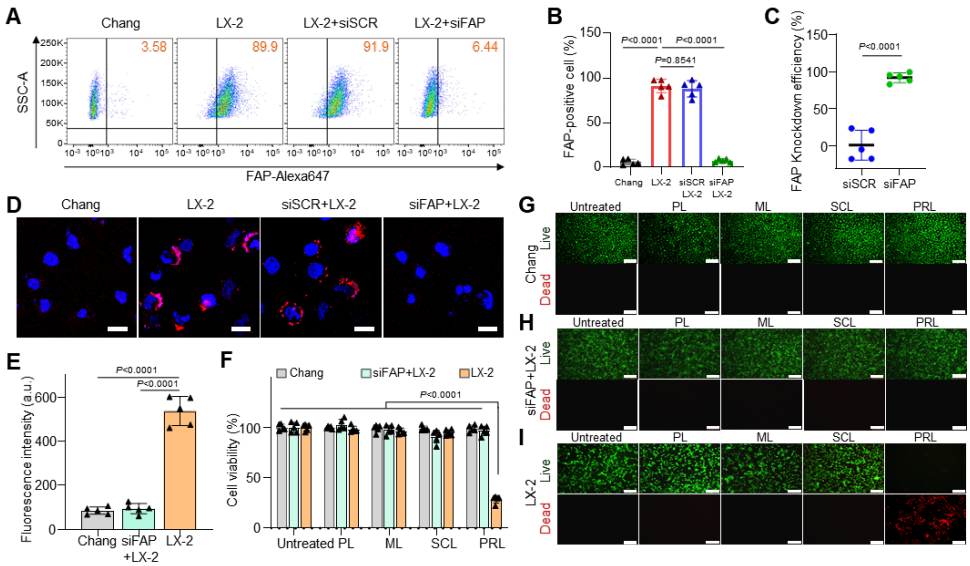

Figure 3. Viability of normal and hepatic stellate cells after treatment with various liposome formulations. (A) LX-2 cells, Chang cells, and siSCR or siFAP-treated LX-2 cells were stained with rabbit anti-FAP primary antibody and FITC-conjugated anti-rabbit secondary antibody. Fluorescence-positive cells were determined by flow cytometry (n = 5 samples per group). (B) FAP positive cell population was analyzed between LX-2 cells, Chang cells, and siSCR or siFAP-treated LX-2. (C) The efficiency of the siFAP in LX-2 cells was evaluated compare to siSCR. (D) Representative confocal images evaluating the efficiency of siFAP in LX-2 cells. Red color indicates FAP expression. (E) The fluorescence emission intensity of FQL was measured at a wavelength of 490 nm after incubation with LX-2 cells, Chang cells, or siFAP-treated LX-2 cells (n = 5 samples per group). (F) MTT assays were used to determine cell viability of following treatment with various liposome formulations (n = 5 samples per group). (G–I) Fluorescence microscopy assessment of live (green)/dead (red) Chang cells (G), siFAP-treated LX-2 cells (H) and LX-2 cells (I). Scale bar: 50 μm.

FAP expression and activation of PRL in a liver fibrosis model

We next tested whether expression of FAP was increased in a liver fibrosis model, and if so, whether promelittin on PRL could be cleaved in the liver. A BDL liver fibrosis model was established using the scheme illustrated in Figure 4A. Flow cytometry showed higher expression of FAP in aHSC from the BDL liver compared with cells from a normal liver (Fig. 4B, 4C). Immunohistochemical staining was performed to assess FAP expression in liver tissue from normal and BDL mice (Fig. 4D). Molecular imaging revealed that PRL was specifically activated at the liver in the BDL model. In normal mice, there was no significant difference of fluorescence intensity regardless of FQL treatment in all organs tested (Fig. 4E, and 4F). In BDL model mice, no significant difference was observed in the heart, lung, spleen,

or kidney (Fig. 4E, 4F). In the liver tissue of BDL model mice, in contrast, a significant difference was observed in the FQL-treated group, which showed 2.5-fold higher fluorescence intensity.

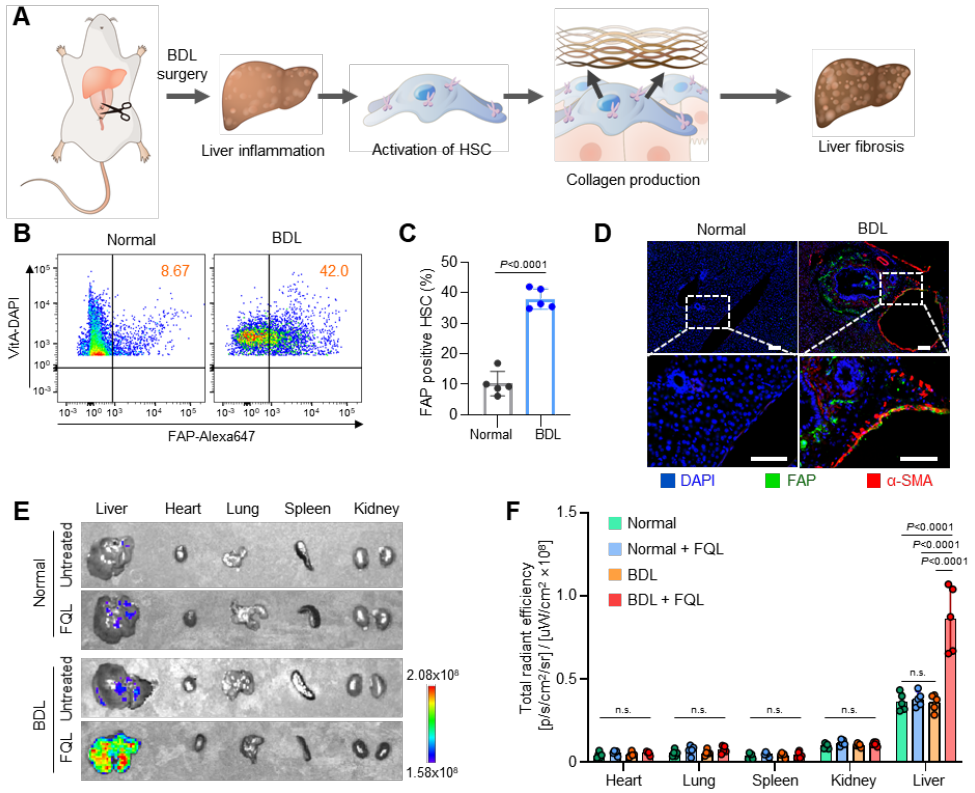

Figure 4. FAP-mediated cleavage of liposomal promelittin in BDL induced fibrosis mice. (A) Experimental scheme for induction of liver fibrosis using the BDL method (n = 5 mice per group). (B, C) FAP expression level in HSC from normal mice or BDL mice was analyzed by flow cytometry. (n = 5 samples per group). (D) Immunohistochemical staining for FAP in liver tissues from normal and BDL mice (n = 5 samples per group). Scale bar: 50 μm. (E) One hour after mice were intravenously injected with FQL, the fluorescence intensities of vital organs (liver, heart, lung, spleen, kidney) from normal and BDL mice were monitored using an IVIS Spectrum instrument equipped with excitation wavelength at 335 nm and emission wavelength at 490 nm. The color bar indicates fluorescence intensity (n = 5 samples per group). (F) Fluorescence intensity of each organ was calculated between normal and BDL mice.

In vivo antifibrotic effect

The experimental scheme for assessing the antifibrotic efficacy of various liposome formulations in a BDL animal model is illustrated in Figure

5A. Antifibrotic efficacy was evaluated using histological, biochemical, and serological analyses. Fibrotic regions of the liver were visualized by Masson's trichrome method, which stains collagen fibers blue and normal tissues red. Masson's trichrome staining showed fibrotic regions in the livers of mice treated with ML, PL, or SCL. In contrast, images of whole livers from mice treated with PRL showed fewer fibrotic (blue-stained) regions compared with livers from mice treated with any other liposome formulation (Fig. 5B). Similar to the Masson's trichrome staining results, H&E staining revealed tissue damage in the vicinity of blood vessels for groups treated with PL, ML, or SCL, but not PRL (Fig. 5B). A quantitative analysis of images revealed that Masson's trichrome-stained liver tissues from mice treated with PRL showed significantly fewer fibrotic regions than those from other treatment groups (Fig. 5C). Applying the METAVIR F staging system, we found that mice treated with PRL showed the lowest scores compared with mice treated with PL, ML, or SCL (Fig. 5D). Biochemical assessments of the antifibrotic efficacy of PRL showed that hydroxyproline levels in BDL mice treated with PL, ML, or SCL did not significantly differ from those in untreated mice. However, hydroxyproline levels in PRL-treated BDL mice were 7.2-fold lower than those in untreated mice (Fig. 5E).

We assessed survival of BDL mice following treatment with various liposome formulations. Among BDL mice treated with various liposome preparations, those treated with PRL showed the highest survival rate. Specifically, PRL-treated mice showed 80 % survival 12 d after BDL surgery, a time point at which mice in all other treatment groups had died (Fig. 5F). Regarding toxicity, normal mice receiving repeated intravenous doses of PRL showed complete survival (supplementary Fig. 3A). All five mice survived for 60 days after four repeated intravenous administrations of PL or PRL (supplementary Fig. 3B). Moreover, there was no significant difference in body weight among the groups (supplementary Fig. 3C).

Treatment of BDL mice with PRL altered the cell populations in liver tissues, which were analyzed with markers for macrophages (F4/80), hepatocytes (cluster of differentiation 26, CD26), endothelial cells (cluster of differentiation 31, CD31), cholangiocytes (cytokeratin7, Ck7), and aHSC (alpha-smooth muscle actin, αSMA). Immunofluorescence imaging (Fig. 5G), quantitative image analysis (Fig. 5G), and quantitative real time polymerase chain reaction (qRT-PCR) (supplementary Fig. 4) showed that the populations of macrophage, hepatocyte, and endothelial cell were not significantly different regardless of treatment. However, the populations of aHSC and cholangiocyte were significantly decreased by PRL treatment (Fig. 5G, 5H, supplementary Fig. 4).

We performed serological analyses with BDL induced liver fibrosis model. PL, ML, or SCL treatment had no significant effect on ALT (Fig. 5I), AST (Fig. 5J), bile acid (Fig. 5K) or total bilirubin (Fig. 5L) serum levels, which were comparable to those in untreated normal mice. However, 4 days

after BDL, serum levels of ALT, AST, bile acid and total bilirubin were all significantly lower following PRL treatment compared with untreated mice or mice treated with other liposome formulations.

TUNEL assays revealed that PRL had an aHSC-selective killing effect. TUNEL-positive cell analysis followed by IHC showed that the highest population of apoptotic cells was observed among αSMA-positive cells (Fig. 5M). Flow cytometry showed that about 78.6% of the apoptotically dying cell populations were aHSC marked with αSMA (Fig. 5N). The population positive for both TUNEL and αSMA was 9.6-fold higher than that positive for both TUNEL and F4/80.

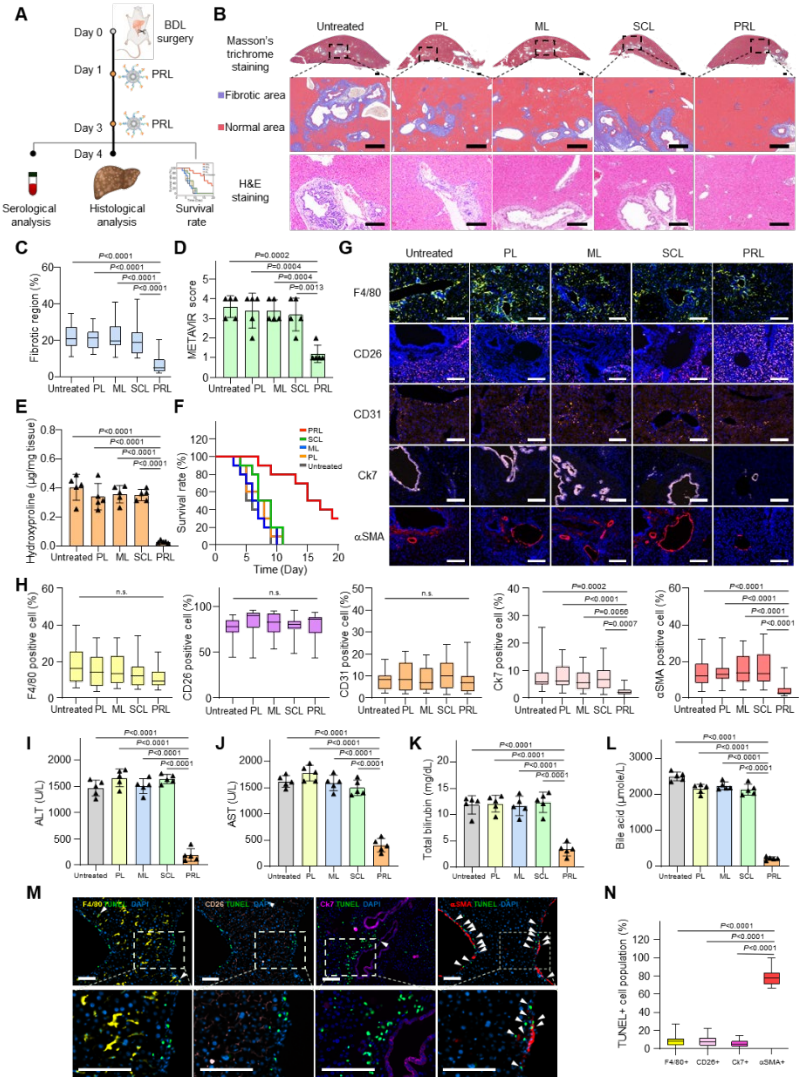

Figure 5. In vivo antifibrotic effects of various liposome preparations in the BDL induced lifer fibrosis model. (A) On days 1 and 3 after BDL surgery, mice were intravenously administered 1 mg/kg PL, ML, SCL or PRL. On day 4, liver tissues were extracted and further analyzed. (B) Top panel

shows representative Masson's trichrome-staining in BDL induced fibrotic liver. Lower panel shows pseudocolored images by InForm 2.2.1 analysis, distinguishing fibrotic regions (blue) from normal tissue (red). Bottom panel shows representative H&E staining in BDL-induced fibrotic liver treated with various liposomes. (n = 5 mice per group). Scale bar: 50 μm. (C) Quantification of connective tissue area, calculated from whole images of stained liver. (D) The severity of liver fibrosis for each group, assessed using the METAVIR scoring system. (E) Collagen content of fibrotic liver samples, measured using hydroxyproline assays. (F) Survival rates of BDL mice after treatment with various liposome formulations (n = 10 mice per group). (G) BDL-induced mice were treated with various liposomes. One day after the last dose, liver tissues were frozen-sectioned and stained with antibodies against F4/80 (macrophage), CD26 (hepatocyte), CD31 (endothelial cell), Ck7 (cholangiocyte), and αSMA (aHSC). (H) Populations of cells were analyzed using a VECTRA tissue analyzer and the InForm 2.2.1 image analysis software (n = 5 mice per group). Scale bar: 50 μm. (I-L) On day 4 after BDL surgery, blood was collected for serum analysis of ALT (I), AST (J), total bilirubin (K), and bile acid (L) (n = 5 samples per group). (M) Liver tissues were stained with TUNEL, followed by immune fluorescence staining with antibodies against αSMA, F4/80, or CD26, and final counter staining with DAPI. Representative images of each group (n = 5 mice per group) are shown. White arrows show TUNEL-positive spots. Scale bar: 50 μm. (N) Analysis of TUNEL-positive cells in 5 randomly selected fields per sample. ALT, alanine transaminase; AST, aspartate transaminase.

The antifibrotic efficacy of PRL was evaluated in the CCl4-induced chronic liver fibrosis model. The treatment scheme for the CCl4-induced liver fibrosis animal model is illustrated in Figure 6A. Immunohistochemistry (Fig. 6B), FACS analysis (Fig. 6C), and flow cytometry (Fig. 6D) showed that the expression of FAP was higher in mice treated with CCl4 over 8 weeks compared to normal mice. Sirius red (Fig. 6E) and Masson's trichrome (Fig. 6G) staining followed by image analysis (Fig. 6F, 6H, respectively) showed that the fibrotic regions were significantly decreased in the PRL-treated group compared to the other groups. The in vivo antifibrotic effect of PLR was also evaluated using the METAVIR F staging system (Fig. 6I), which revealed that the METAVIR score was lowest in the PRL-treated group. The level of hydroxyproline, a major component of collagen, was 3.2-fold lower in PRL-treated mice than in untreated mice (Fig. 6J).

Serological analysis revealed that PRL treatment significantly lowered the levels of AST (Fig. 6K) and ALT (Fig. 6L) relative to the other treatments and the untreated fibrotic control. Immunohistochemistry showed that the populations of cells positive for F4/80, CD26, or CD31 were not significantly different among the groups, regardless of treatment, whereas the level of the aHSC marker, αSMA, was significantly lower in the group treated with PRL relative to the other groups (Fig. 6M, 6N).

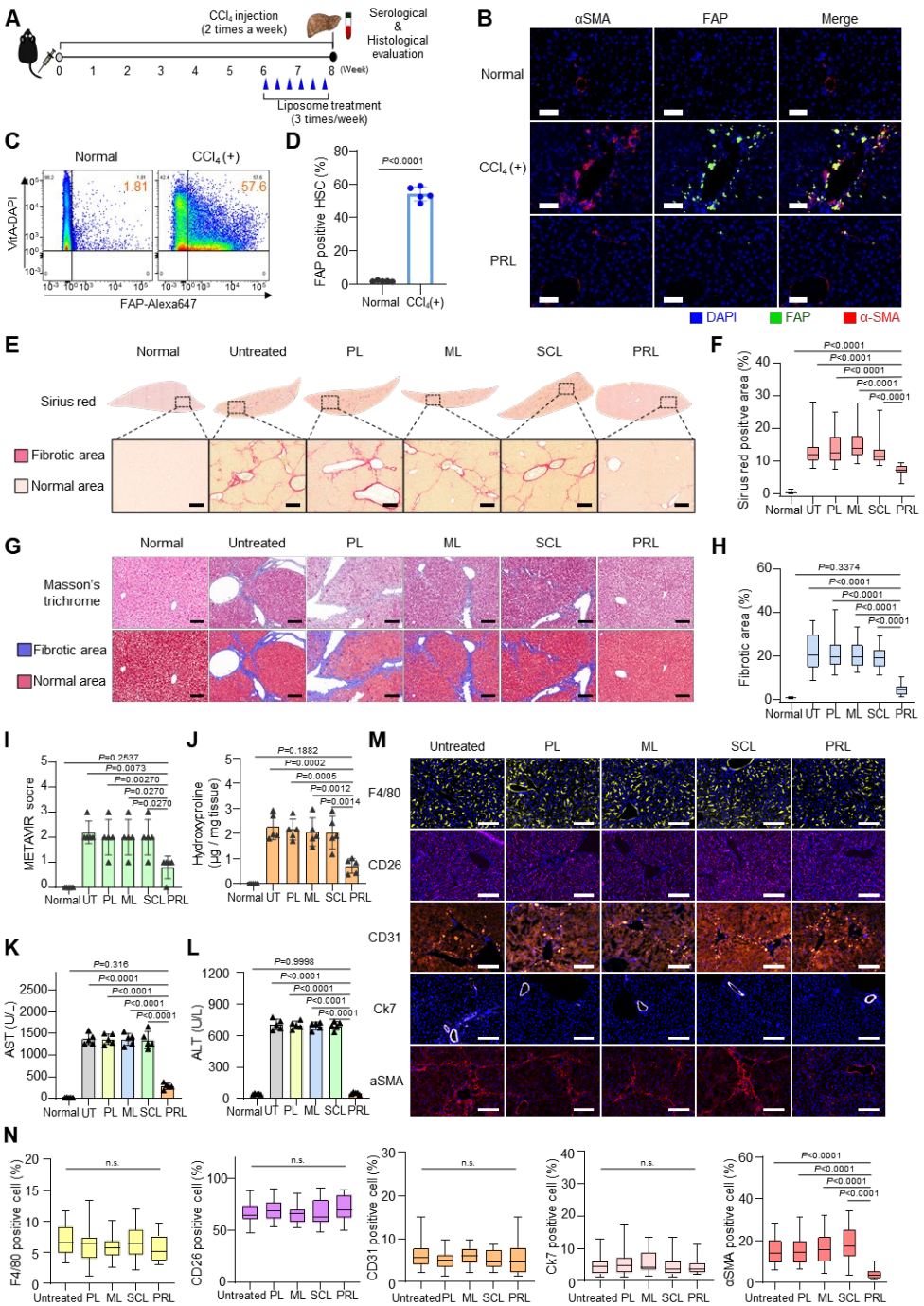

Figure 6. In vivo antifibrotic effects of various liposome preparations in the CCl_4-induced liver fibrosis model. (A) Schematic of the CCl_4-induced liver fibrosis model and treatment timelines for the various liposomes. (B) Immunohistochemical staining for FAP in liver tissues from normal and CCl_4-induced liver fibrosis mice (n = 5 samples per group). Scale bar: 50 μm. (C, D) FAP expression levels on HSCs from normal or CCl_4-induced fibrotic liver

were analyzed by flow cytometry (n = 5 mice per group). (E, F) Representative Sirius red-stained liver images for the evaluation of liver fibrosis, and quantification of the Sirius red-positive area (n = 5 mice per group). (G) Upper panel shows representative Masson's trichrome-stained images of CCl_4-induced fibrotic liver. Lower panel displays pseudocolored images by InForm 2.2.1 analysis, distinguishing fibrotic regions (blue) from normal tissue (red) (n = 5 mice per group). Scale bar: 50 μm. (H) Quantification of the connective tissue area under Masson's trichrome staining, as calculated from 5 randomly selected fields per sample. (I) The severity of liver fibrosis for each group, assessed using the METAVIR scoring system. (J) Collagen content of fibrotic liver samples, as measured using hydroxyproline assays. (K, L) Blood was collected for serum analysis of AST (K) and ALT (L) (n = 5 mice per group), UT: untreated group. (M) Representative immunofluorescence images of liver tissues stained with various cell markers including F4/80 (macrophage), CD26 (hepatocyte), CD31 (endothelial cell), Ck7 (cholangiocyte), and αSMA (aHSC). (N) Populations of cells were analyzed using a VECTRA tissue analyzer and the InForm 2.2.1 image analysis software (n = 5 mice per group). Scale bar: 50 μm.

The in vivo efficacy of PRL was evaluated in the CDAHFD-induced model. The liposome treatment scheme for CDAHFD-induced model mice is illustrated in Figure 7A. Compared to normal liver tissues, those of CDAHFD-induced model mice showed upregulated expression of FAP on αSMA-positive aHSC (Fig. 7B). FACS (Fig. 7C) and flow cytometric analysis (Fig. 7D) revealed that the level of FAP-positive cells was 5.2-fold higher in the CDAHFD-induced model compared to normal liver.

Histological evaluation with Sirius red, Masson's trichrome, and H&E staining consistently revealed that PRL had an antifibrotic effect. In Sirius red staining, the fibrotic regions were significantly smaller in the group treated with PRL compared to the other groups (Fig. 7E, 7F). Image analysis of Sirius red staining showed that the fibrotic region was 3.2-fold smaller in the PRL-treated group compared to PL-treated group. Masson's trichrome staining showed that the fibrotic region was lowest in the liver tissue of PRL-treated mice (Fig. 7G, H). Hydroxyproline levels in PRL-treated mice were 3.1-fold lower than those in untreated mice (Fig. 7I). The serum levels of AST (Fig. 7J) and ALT (Fig. 7K) were lowest in the group treated with PRL among the tested groups.

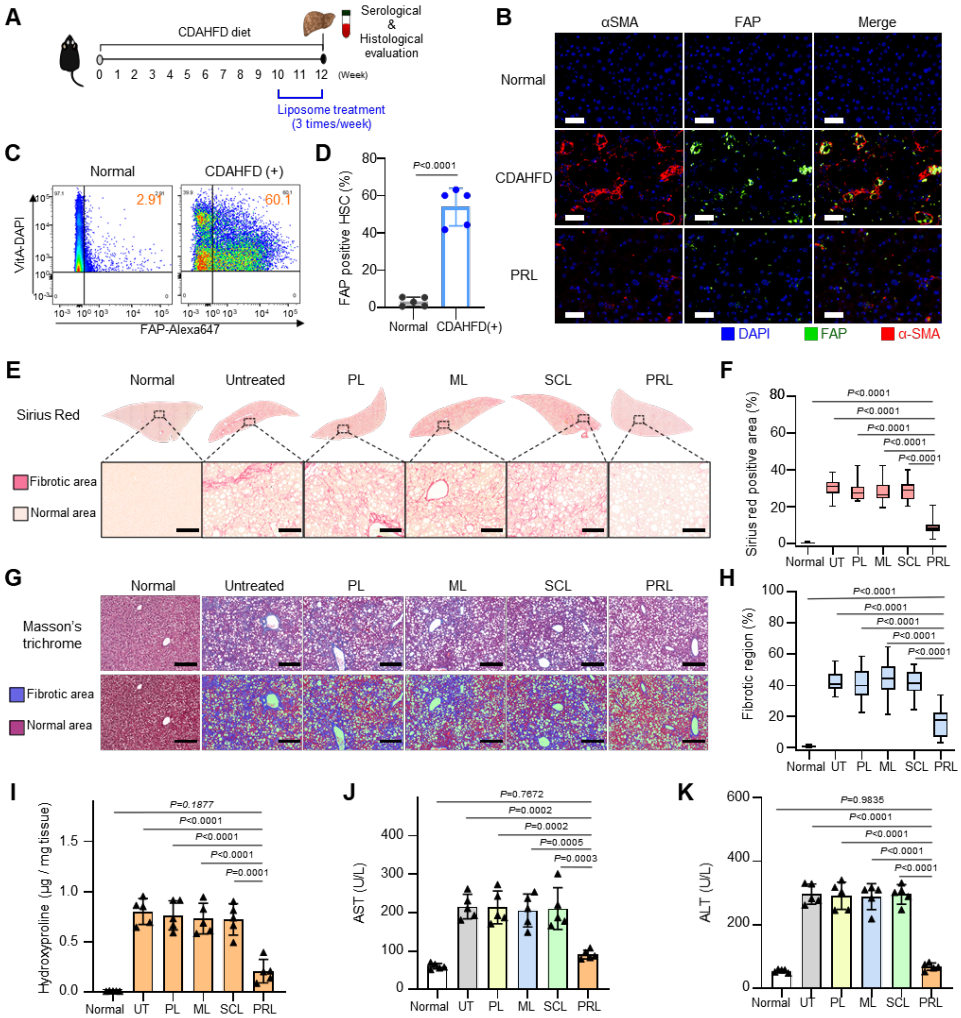

Figure 7. In vivo antifibrotic effects of various liposome preparations in the CDAHFD-induced fibrosis model. (A) Schematic of the CDAHFD-induced fibrosis model and treatment timelines for the various liposomes. (B) Representative images of liver sections stained for FAP (green), αSMA (red), and DAPI (blue) (n = 5 mice per group). Scale bar: 50 μm. (C, D) FAP expression levels on HSCs from normal or CDAHFD-induced fibrotic liver were evaluated by flow cytometry (n = 5 mice per group). (E, F) Representative Sirius red-stained liver images for the evaluation of liver fibrosis and quantification of the Sirius red-positive area (n = 5 mice per group). (G) Top panel shows representative Masson's trichrome-staining of liver. Bottom panel displays pseudocolored images by InForm 2.2.1 analysis, distinguishing fibrotic regions (blue) from normal tissue (red) (n = 5 mice per group). Scale bar: 50 μm. (H) Quantification of Masson's trichrome-stained connective tissue area calculated from 5 randomly selected fields per sample (n = 5 mice per group). (I) Collagen content of fibrotic liver samples, as measured using hydroxyproline assays. (J, K) Blood was collected for serum analysis of AST (J) and ALT (K) (n = 5 mice per group), UT: untreated group.

4. Discussion

In this study, we demonstrated that promelittin on PRL can be specifically cleaved by FAP in fibrotic liver tissues. The FAP-liberated melittin was shown to be capable of killing aHSC and alleviating fibrosis in mouse models of liver fibrosis induced by BDL, CCl4, or CDAHFD. The cleavage of PRL in liver tissues was visualized by molecular imaging of FQL. In the liver fibrosis model, PRL treatment exerted an antifibrotic effect and especially prolonged survival in BDL mice.

Recently, various strategies have been reported to induce antifibrotic effects. For example, hepatic macrophages have been targeted in relaxin-mediated liver fibrosis therapy. Relaxin is known to bind to aHSC and hepatic macrophages, and the binding of relaxin to macrophages was very recently reported to switch them from the profibrogenic to pro-resolution phenotype [13]. Other strategies have sought to induce antifibrotic effects by metabolic regulation aimed at inhibiting the activation of HSCs. For example, an adiponectin-based agonist was shown to regulate lipid and glucose metabolism by binding to relevant receptors and thereby suppress HSC activation [14]. Cotadutide, which is an agonist of the glucagon receptor and glucagon-like protein-1 receptor, was reported to alleviate fibrosis via modulating lipogenesis in hepatocytes [15].

In this study, different from inhibiting the activation of HSCs, PRL can selectively kill FAP-expressing aHSC to exert antifibrotic effects. The fibrosis-stimulated antifibrotic effect of PRL may prove useful for treating fibrosis in various fibrosis models. Indeed, we herein show that PRL exhibited antifibrotic effects in animal models induced by BDL surgery, CCl4, or a high-fat diet. Our results further show that PRL selectively kills aHSC, not macrophages, suggesting that the combination of PRL with relaxin gene therapy may widen the spectrum of effective antifibrotic strategies by inhibiting the activation of HSCs and depleting aHSC (supplementary Fig. 1).

In this study, we observed that PRL has substantial antifibrotic effects in the fibrosis models induced by CCl4 or high-fat diet. The severity of fibrosis reportedly depends on the dose and duration of CCl4 injection or high-fat diet feeding [16]. The dosing regimens of antifibrotic agents have differed across various studies, and different regimens have yielded different outcomes. For example, when adiponectin agonist treatment was initiated at week 3 of CCl4 injection, liver fibrosis was still evident 3 weeks later [14]. In another study, relaxin-based gene therapy was initiated at week 4 of CCl4 injection or week 8 of high-fat diet feeding, and complete absence of fibrosis was observed at 2 weeks after the initiation of gene therapy in both models [13]. When an antagonist of the binding of arginine-glycine-aspartate to integrin was delivered at week 6 of high-fat diet feeding, liver fibrosis was significantly ameliorated at week 4 after the initiation of antagonist treatment [17].

To obtain an optimal antifibrotic effect, we used a dosing regimen wherein PRL injection was initiated at week 6 of CCl4 injection or week 10

of high-fat diet feeding. Compared to studies in which treatment began at weeks 3 or 4 of CCl4 injection or weeks 6 to 8 of high-fat diet feeding, we began injecting PRL at later phases of CCl4 or NASH model development. FAP expression intensity has been shown to correlate with the severity of liver fibrosis [8, 18, 19, 20]. Since PRL needs FAP-expressing aHSC to exhibit antifibrotic effects, we hypothesized that progressed fibrosis would activate the antifibrotic effect of PRL more effectively than early-phase fibrosis. Indeed, we observed that the antifibrotic effect of PRL was less intense when PRL was given at week 4 of CCl4 treatment compared to the utilized regimen starting at week 6 of CCl4 induction (supplementary Fig. 7). The increased effect of PRL when given at the later phase of fibrosis seems to support the fibrosis-activated antifibrotic effect of PRL.

FAP-specific activation of PRL would be crucial for focusing the effects of melittin on target fibrotic cells and minimizing possible side effects of melittin in the bloodstream. To prevent the action of melittin on blood cells, we conjugated inactive promelittin to the surface of ML. Cys-promelittin was covalently tethered to the surface of ML using the maleimide reaction. Because a sulfide group is required for the maleimide reaction, we used cys-promelittin, in which a cysteine amino acid residue was added to the C-terminus of promelittin. RBC hemolysis assays support the conclusion that PRL is inactive against RBCs.

Instead of using the promelittin peptide per se, we used liposome formulations containing promelittin on the surface. PRL-bound promelittin has several potential advantages over free promelittin peptide. First, intravenous injection of nanoparticles has been reported to provide the highest distribution to the liver [21]. This is consistent with other previous reports showing that intravenously injected liposomes [22], polymeric micelles [23], and other nanoparticles [24] are distributed to the liver to a greater extent than to other organs. Second, the tethering of promelittin on the PEGylated surface of PRL may prevent the nonspecific adsorption of proteases to liposomes. PEGylation has been reported to reduce the nonspecific opsonization and adsorption of proteins onto liposomes [25]. Here, the use of PEGylated liposomes for PRL could contribute to reducing nonspecific interactions with and cleavage of promelittin peptide by proteases in the blood. Third, the use of PRL provides the further opportunity to deliver both melittin and other antifibrotic chemical drugs, such as silibinin [26, 27] and quercetin [28]. Although we used PRL without chemical agents to demonstrate proof-of-concept in this study, the co-delivery of other antifibrotic chemical drugs loaded inside liposomes could further increase the anti-fibrotic efficacy of PRL.

Quenching and dequenching FRET phenomena have been used to test the cleavage of substrate peptides by enzymes in vivo. For example, a capsid protease-sensitive FRET system has been used as a proteolytic assay for the chikungunya virus [29], and a FRET-based platform employing fluorescent carbon dots and MnO2 nanosheets have been used to detect glutathione in

human blood [30]. Here, we tested the FAP-specific cleavage of promelittin by assessing FAP-mediated recovery of fluorescence of FQL, composed of promelittin peptide dually modified with the fluorophore EDANS and quencher DABCYL. In the absence of FAP, FQL remains quenched owing to FRET between the fluorophore and the quencher. However, the cleavage of promelittin peptide by FAP abrogates the close interaction of EDANS with the quencher, resulting in a recovery of EDANS fluorescence. We found that not only was FQL fluorescence recovered by FAP in a cell-free system, it was also recovered by FAP-positive LX-2 cells, but not by Chang cells. Importantly, fluorescence was also increased in the livers of BDL mice intravenously injected with FQL, confirming cleavage of promelittin peptide in vivo. The recovery of FQL fluorescence both in vitro and in vivo supports the cleavage of promelittin on PRL by FAP in fibrotic liver tissues. The specific cleavage of PRL by FAP on fibrotic liver cells may enhance the activity of liberated melittin towards FAP-positive cells.

In this study, we observed that the treatment of activated LX2 cells with siFAP significantly reduced the expression of FAP without affecting cell viability under PRL treatment. This might occur because the cytotoxic effect of melittin is nonlinear (supplementary Fig. 5): The viability of activated LX-2 cells treated with 1.0 μg/ml melittin was 100%, whereas this viability decreased to 20% following treatment with 2.0 μg /ml melittin. To exert notable cytotoxicity against LX2 cells, therefore, melittin must be liberated at a level greater than its minimal effective concentration.

Our molecular imaging studies revealed that the activation of PRL was specific to the liver of BDL model mice, and was not seen in other organs. The notable fluorescence intensities of FQL at the liver of BDL model mice support the notion that the fluorescent signal is selectively liberated by the increased FAP expression in liver tissues of BDL model mice. We herein measured the activation of FQL using ex vivo organ tissues rather than in vivo whole-animal imaging because the fluorescence signal liberated from FQL has an excitation wavelength of 335 nm, which limits in vivo imaging. The results of our ex vivo imaging suggest that there was little FAP-mediated activation of PRL in other vital organs, such as the heart, lung, spleen, and kidney. This lack of activation in other vital organs indicates that there is little possibility that pore-forming melittin will be liberated at nontarget organs.

The antifibrotic efficacy of PRL is attributable to reductions in the population of aHSC through the cytotoxic action of liberated melittin. FAP was observed to be overexpressed in stellate cells from the fibrotic liver, but not those from the normal liver. Hepatic stellate cells in the fibrotic liver are known to be abnormally activated and overproduce collagen fibers [31]. The reduction of abnormally high aHSC populations may decrease the production of collagen fibers, and thereby reduce fibrosis. In this study, we observed that PRL, which killed FAP-positive sHSC, reduced the levels of hydroxyproline, a metabolite of collagen fibers [32]. The decrease in collagen fibers in the BDL liver also supports the efficacy of PRL against collagen fiber formation.

We observed that PRL did not affect the population of FAP-negative cells such as macrophages, hepatocytes, and endothelial cells. The decrease of cholangiocytes by PRL treatment might be attributed to the amelioration of fibrosis. It has been reported that cholangiocytes are involved in liver fibrogenesis [33].

Although we demonstrated the antifibrotic efficacy of PRL in a liver fibrosis model, the selective activation of PRL by FAP suggests the potential of PRL for the treatment of various fibrotic diseases in which FAP is overexpressed. FAP has drawn considerable attention as a target enzyme in various fibrotic diseases and cancer. In the tumor microenvironment, cancer-associated fibroblasts have been reported to overexpress FAP [34]. In addition to cancers, fibrotic livers and inflamed areas [9], as well as regions of lung fibrosis [35], have been shown to overexpress FAP. Moreover, although we used promelittin to demonstrate FAP-specific activation in fibrotic tissues, our strategy could be applied to design other FAP-specific activation systems for fibrotic tissues. For example, other bioactive antifibrotic peptides can be converted to a form that is inactive in the bloodstream by introducing additional sequences and tethering the peptides to the surface of liposomes. Accordingly, FAP-selective cleavage in fibrotic tissues can confer the targeted therapeutic efficacy of antifibrotic peptides in pathogenic sites.

In this study, we observed 100% mortality at 10 days after BDL surgery in BALB/c mice. It has been reported that the mortality of mice after BDL surgery can be affected by the utilized mouse species: Compared to C57BL/6 mice, BALB/c mice are more sensitive to liver fibrosis and show lower survival after BDL surgery [36]. The techniques used for BDL surgery are also expected to impact the mortality rate. BDL surgery can be done using either single-knot ligation or double-knot ligation with resection [37]. Single-knot ligation decreases but does not completely block the flow of bile through the bile duct, reflecting the conditions of cholestasis. Double-knot ligation with resection, which is often used to establish acute liver fibrosis, blocks bile flow and is associated with lower survival than single-knot ligation. The high mortality rate seen in our mouse model might be thus attributed to the use of the double-knot ligation method for BDL surgery in more susceptible BALB/c mice.

In conclusion, we showed that PRL is selectively activated by FAP overexpressed in the fibrotic liver and effectively alleviates fibrosis. The FAP-specific liberation of melittin in the fibrotic liver can reduce the population of abnormal hepatic stellate cells and reduce the overproduction of collagen fibers. PRL encapsulating other antifibrotic chemical agents in their interior may be designed to increase antifibrotic efficacy. Notably, the PRL described here also provides insight into the design of systems with FAP-selective activation of other nanomaterials for the effective treatment of a range of fibrotic diseases in which FAP is known to be overexpressed.

5. References

[1] Ge PS, Runyon BA. Treatment of Patients with Cirrhosis. N Engl J Med. 2016 Aug 25;375(8):767-77.

[2] Higashi T, Friedman SL, Hoshida Y. Hepatic stellate cells as key target in liver fibrosis. Adv Drug Deliv Rev. 2017 Nov 1;121:27-42.

[3] Lemoinne S, Friedman SL. New and emerging anti-fibrotic therapeutics entering or already in clinical trials in chronic liver diseases. Curr Opin Pharmacol. 2019 Dec;49:60-70.

[4] Li Y, Pu S, Liu Q, Li R, Zhang J, Wu T, Chen L, Li H, Yang X, Zou M, Xiao J, Xie W, He J. An integrin-based nanoparticle that targets activated hepatic stellate cells and alleviates liver fibrosis. J Control Release. 2019 Jun 10;303:77-90.

[5] Qiao JB, Fan QQ, Zhang CL, Lee J, Byun J, Xing L, Gao XD, Oh YK, Jiang HL. Hyperbranched lipoid-based lipid nanoparticles for bidirectional regulation of collagen accumulation in liver fibrosis. J Control Release. 2020 May 10;321:629-640.

[6] Shaker ME, Ghani A, Shiha GE, Ibrahim TM, Mehal WZ. Nilotinib induces apoptosis and autophagic cell death of activated hepatic stellate cells via inhibition of histone deacetylases. Biochim Biophys Acta. 2013 Aug;1833(8):1992-2003.

[7] Zhang J, Wang M, Zhang Z, Luo Z, Liu F, Liu J. Celecoxib derivative OSU-03012 inhibits the proliferation and activation of hepatic stellate cells by inducing cell senescence. Mol Med Rep. 2015 Apr;11(4):3021-6.

[8] De Decker A, Vliegen G, Van Rompaey D, Peeraer A, Bracke A, Verckist L, Jansen K, Geiss-Friedlander R, Augustyns K, De Winter H, De Meester I, Lambeir AM, Van der Veken P. Novel Small Molecule-Derived, Highly Selective Substrates for Fibroblast Activation Protein (FAP). ACS Med Chem Lett. 2019 Jul 9;10(8):1173-1179.

[9] Schuppan D, Ashfaq-Khan M, Yang AT, Kim YO. Liver fibrosis: Direct antifibrotic agents and targeted therapies. Matrix Biol. 2018 Aug;68-69:435-451.

[10] Lindner T, Loktev A, Giesel F, Kratochwil C, Altmann A, Haberkorn U. Targeting of activated fibroblasts for imaging and therapy. EJNMMI Radiopharm Chem. 2019 Jul 25;4(1):16.

[11] Park SH, Cho HJ, Jeong YJ, Shin JM, Kang JH, Park KK, Choe JY, Park YY, Bae YS, Han SM, Moon SK, Kim WJ, Choi YH, Chang YC. Melittin inhibits TGF-β-induced pro-fibrotic gene expression through the suppression of the TGFβRII-Smad, ERK1/2 and JNK-mediated signaling pathway. Am J Chin Med. 2014;42(5):1139-52.

[12] Lee G, Bae H. Anti-Inflammatory Applications of Melittin, a Major Component of Bee Venom: Detailed Mechanism of Action and Adverse Effects. Molecules. 2016 May 11;21(5):616.

[13] Hu M, Wang Y, Liu Z, Yu Z, Guan K, Liu M, Wang M, Tan J, Huang

L. Hepatic macrophages act as a central hub for relaxin-mediated alleviation of liver fibrosis. Nat Nanotechnol. 2021 Apr;16(4):466-477.

[14] Xu H, Zhao Q, Song N, Yan Z, Lin R, Wu S, Jiang L, Hong S, Xie J, Zhou H, Wang R, Jiang X. AdipoR1/AdipoR2 dual agonist recovers nonalcoholic steatohepatitis and related fibrosis via endoplasmic reticulum-mitochondria axis. Nat Commun. 2020 Nov 16;11(1):5807.

[15] Boland ML, Laker RC, Mather K, Nawrocki A, Oldham S, Boland BB, Lewis H, Conway J, Naylor J, Guionaud S, Feigh M, Veidal SS, Lantier L, McGuinness OP, Grimsby J, Rondinone CM, Jermutus L, Larsen MR, Trevaskis JL, Rhodes CJ. Resolution of NASH and hepatic fibrosis by the GLP-1R/GcgR dual-agonist Cotadutide via modulating mitochondrial function and lipogenesis. Nat Metab. 2020 May;2(5):413-431.

[16] Rong X, Liu J, Yao X, Jiang T, Wang Y, Xie F. Human bone marrow mesenchymal stem cells-derived exosomes alleviate liver fibrosis through the Wnt/β-catenin pathway. Stem Cell Res Ther. 2019 Mar 18;10(1):98.

[17] Ulmasov B, Noritake H, Carmichael P, Oshima K, Griggs DW, Neuschwander-Tetri BA. An Inhibitor of Arginine-Glycine-Aspartate-Binding Integrins Reverses Fibrosis in a Mouse Model of Nonalcoholic Steatohepatitis. Hepatol Commun. 2018 Dec 27;3(2):246-261.

[18] Levy MT, McCaughan GW, Marinos G, Gorrell MD. Intrahepatic expression of the hepatic stellate cell marker fibroblast activation protein correlates with the degree of fibrosis in hepatitis C virus infection. Liver. 2002 Apr;22(2):93-101.

[19] Wang XM, Yu DM, McCaughan GW, Gorrell MD. Fibroblast activation protein increases apoptosis, cell adhesion, and migration by the LX-2 human stellate cell line. Hepatology. 2005 Oct;42(4):935-45.

[20] Wang XM, Holz LE, Chowdhury S, Cordoba SP, Evans KA, Gall MG, Vieira de Ribeiro AJ, Zheng YZ, Levy MT, Yu DM, Yao TW, Polak N, Jolly CJ, Bertolino P, McCaughan GW, Gorrell MD. The pro-fibrotic role of dipeptidyl peptidase 4 in carbon tetrachloride-induced experimental liver injury. Immunol Cell Biol. 2017 May;95(5):443-453.

[21] Poon W, Zhang YN, Ouyang B, Kingston BR, Wu JLY, Wilhelm S, Chan WCW. Elimination Pathways of Nanoparticles. ACS Nano. 2019 May 28;13(5):5785-5798.

[22] Furuhashi H, Tomita K, Teratani T, Shimizu M, Nishikawa M, Higashiyama M, Takajo T, Shirakabe K, Maruta K, Okada Y, Kurihara C, Watanabe C, Komoto S, Aosasa S, Nagao S, Yamamoto J, Miura S, Hokari R. Vitamin A-coupled liposome system targeting free cholesterol accumulation in hepatic stellate cells offers a

beneficial therapeutic strategy for liver fibrosis. Hepatol Res. 2018 Apr;48(5):397-407.

[23] Fan QQ, Zhang CL, Qiao JB, Cui PF, Xing L, Oh YK, Jiang HL. Extracellular matrix-penetrating nanodrill micelles for liver fibrosis therapy. Biomaterials. 2020 Feb;230:119616.

[24] Liu Z, Li Y, Li W, Xiao C, Liu D, Dong C, Zhang M, Mäkilä E, Kemell M, Salonen J, Hirvonen JT, Zhang H, Zhou D, Deng X, Santos HA. Multifunctional Nanohybrid Based on Porous Silicon Nanoparticles, Gold Nanoparticles, and Acetalated Dextran for Liver Regeneration and Acute Liver Failure Theranostics. Adv Mater. 2018 Jun;30(24):e1703393.

[25] Suk JS, Xu Q, Kim N, Hanes J, Ensign LM. PEGylation as a strategy for improving nanoparticle-based drug and gene delivery. Adv Drug Deliv Rev. 2016 Apr 1;99(Pt A):28-51.

[26] Qiao JB, Fan QQ, Xing L, Cui PF, He YJ, Zhu JC, Wang L, Pang T, Oh YK, Zhang C, Jiang HL. Vitamin A-decorated biocompatible micelles for chemogene therapy of liver fibrosis. J Control Release. 2018 Aug 10;283:113-125.

[27] Hayashi K, Maruhashi T, Sakamoto W, Yogo T. Organic-Inorganic Hybrid Hollow Nanoparticles Suppress Oxidative Stress and Repair Damaged Tissues for Treatment of Hepatic Fibrosis. Adv Funct Mater. 2018;28(13).

[28] Wu L, Zhang Q, Mo W, Feng J, Li S, Li J, Liu T, Xu S, Wang W, Lu X, Yu Q, Chen K, Xia Y, Lu J, Xu L, Zhou Y, Fan X, Guo C. Quercetin prevents hepatic fibrosis by inhibiting hepatic stellate cell activation and reducing autophagy via the TGF-β1/Smads and PI3K/Akt pathways. Sci Rep. 2017 Aug 24;7(1):9289.

[29] Saha A, Acharya BN, Priya R, Tripathi NK, Shrivastava A, Rao MK, Kesari P, Narwal M, Tomar S, Bhagyawant SS, Parida M, Dash PK. Development of nsP2 protease based cell free high throughput screening assay for evaluation of inhibitors against emerging Chikungunya virus. Sci Rep. 2018 Jul 17;8(1):10831.

[30] Wang YH, Jiang K, Zhu JL, Zhang L, Lin HW. A FRET-based carbon dot-MnO2 nanosheet architecture for glutathione sensing in human whole blood samples. Chem Commun. 2015;51(64):12748-51.

[31] Zhang CY, Yuan WG, He P, Lei JH, Wang CX. Liver fibrosis and hepatic stellate cells: Etiology, pathological hallmarks and therapeutic targets. World J Gastroenterol. 2016 Dec 28;22(48):10512-10522.

[32] Li P, Wu G. Roles of dietary glycine, proline, and hydroxyproline in collagen synthesis and animal growth. Amino Acids. 2018 Jan;50(1):29-38.

[33] Glaser SS, Gaudio E, Miller T, Alvaro D, Alpini G. Cholangiocyte proliferation and liver fibrosis. Expert Rev Mol Med. 2009 Feb 25;11:e7.

[34] Chen X, Song E. Turning foes to friends: targeting cancer-associated fibroblasts. Nat Rev Drug Discov. 2019 Feb;18(2):99-115.

[35] Hamson EJ, Keane FM, Tholen S, Schilling O, Gorrell MD. Understanding fibroblast activation protein (FAP): substrates, activities, expression and targeting for cancer therapy. Proteomics Clin Appl. 2014 Jun;8(5-6):454-63.

[36] Canbay A, Higuchi H, Bronk SF, Taniai M, Sebo TJ, Gores GJ. Fas enhances fibrogenesis in the bile duct ligated mouse: a link between apoptosis and fibrosis. Gastroenterology. 2002 Oct;123(4):1323-30.

[37] Sanjel B, Shim WS. Recent advances in understanding the molecular mechanisms of cholestatic pruritus: A review. Biochim Biophys Acta Mol Basis Dis. 2020 Dec 1;1866(12):165958.

[38] Ghirga F, Bonamore A, Calisti L, D'Acquarica I, Mori M, Botta B, Boffi A, Macone A. Green Routes for the Production of Enantiopure Benzylisoquinoline Alkaloids. Int J Mol Sci. 2017 Nov 20;18(11):2464.

[39] Shim G, Le QV, Suh J, Choi S, Kim G, Choi HG, Kim YB, Macgregor RB Jr, Oh YK. Sequential activation of anticancer therapy triggered by tumor microenvironment-selective imaging. J Control Release. 2019 Mar 28;298:110-119.

[40] Tag CG, Sauer-Lehnen S, Weiskirchen S, Borkham-Kamphorst E, Tolba RH, Tacke F, Weiskirchen R. Bile duct ligation in mice: induction of inflammatory liver injury and fibrosis by obstructive cholestasis. J Vis Exp. 2015 Feb 10;(96):52438.

[41] Matsumoto M, Hada N, Sakamaki Y, Uno A, Shiga T, Tanaka C, Ito T, Katsume A, Sudoh M. An improved mouse model that rapidly develops fibrosis in non-alcoholic steatohepatitis. Int J Exp Pathol. 2013 Apr;94(2):93-103.

[42] Mederacke I, Dapito DH, Affò S, Uchinami H, Schwabe RF. High-yield and high-purity isolation of hepatic stellate cells from normal and fibrotic mouse livers. Nat Protoc. 2015 Feb;10(2):305-15.

[43] LeBeau AM, Brennen WN, Aggarwal S, Denmeade SR. Targeting the cancer stroma with a fibroblast activation protein-activated promelittin protoxin. Mol Cancer Ther. 2009 May;8(5):1378-86.

[44] Anderson RL, Davis S. An organic phosphorus assay which avoids the use of hazardous perchloric acid. Clin Chim Acta. 1982 May 6;121(1):111-6.

Chapter V

Conclusion

Conclusion

In this study, I developed three different types of the stimuli-responsive delivery system. Exogenous stimuli, which were light and cold atmospheric plasma, were used as a tool for tumor immune microenvironment modulation. On the other hand, to use endogenous stimuli derived from the fibrotic microenvironment, a fibroblast activation protein (FAP) responsive drug delivery system was exploited to deliver anti-fibrotic peptide to pathogenic fibroblast.

First, I utilized methylene blue (MB) as a model photosensitizer, gold nanocluster as a model photothermal agent, and polymerized DNA as the backbone of the nanocluster. We synthesized MB-intercalated gold DNA nanocluster (GMDN) via the reduction and clustering of gold ions on a template consisting of MB-intercalated long DNA. Upon dual-light irradiation, the tumor immune microenvironment was activated in terms of adaptive anti-tumor immune response by T cells. Tumor growth was almost completely eradicated in GMDN-treated tumor-bearing mice after dual light irradiation, and rechallenged tumor growth was also inhibited.

Second, cold atmospheric plasma, the ionized gas which is capable of inducing immunogenic tumor cell death, was exploited for on-site hydrogel application in the tumor microenvironment, aiming to facilitate the sustainable uptake of tumor-associated antigens and nanoadjuvants by dendritic cells. The hyaluronic acid-tyramine conjugate was intratumorally injected as a liquid and formed an on-site hydrogel under irradiation with cold atmospheric plasma. Intratumoral delivery of hyaluronic acid-tyramine conjugate with transforming growth factor β-blocking nanoadjuvant (TLN) followed by cold atmospheric plasmid irradiation yielded a micro-network of TLN-loaded hydrogel (TLN@CHG). In vivo intratumoral injection of TLN@CHG promoted the activation of dendritic cells and more effectively increased the proportion of CD4 T cells and CD8 T cells in the tumor microenvironment, compared to the groups receiving TLN or hydrogel alone. Moreover, in CT26 tumor model mice, cold atmospheric plasma-induced TLN@CHG therapy ablated the primary tumor and provided 100% survival among mice rechallenged with CT26 cells.

Lastly, a liver fibrosis-actuated antifibrotic peptide-delivery system was reported in which FAP overexpressed in fibrotic regions of the liver liberates the antifibrotic peptide, melittin, by cleaving a FAP-specific site in the peptide. The promelittin peptide was linked to PEGylated and maleimide-functionalized liposomes, resulting in promelittin-modified liposomes (PRL). The specific cleavage of promelittin on PRL by FAP was tested using fluorophore- and quencher-modified promelittin liposomes (FQL). Cleavage of the peptide by FAP, but not by matrix metalloproteinase, recovered the quenched fluorescence of FQL. In vitro experiments revealed that PRL was effective in reducing the viability of LX-2 activated hepatic stellate cells (aHSC), but not that of FAP-negative control cells or LX-2 cells treated with FAP-specific siRNA. In vivo experiments showed that the fluorescence signal

of FQL was recovered in bile duct-ligated mouse livers, but not in normal livers. In three types of liver fibrosis models, intravenously administered PRL significantly reduced fibrotic regions and the levels of hydroxyproline. All mice in groups treated with PEGylated or scrambled peptide-conjugated liposomes only died by day 15 after bile duct ligation. In contrast, PRL-treated mice showed 80% survival on day 12 after bile duct ligation.

In conclusion, the drug systems which were investigated here exploited different kinds of stimuli to tumor and fibrosis models. Although these delivery systems were tested in tumor and liver fibrosis, it could be extended to other diseases, such as wound healing, obesity and pulmonary fibrosis.

Since the exogenous stimuli were applied to the local diseased area, unpredictable systemic toxicity could be minimized with the system. One of the concerns is about the effective therapeutic depth of the stimuli-applied tissue. Since exogenous stimuli which were used in the thesis have limited penetration depth, other strategies like an upconversion system or microneedle could be combined to maximize the efficacy of microenvironment modulation.

For endogenous stimuli, the study can be applied to other fibrotic diseases including cardiac fibrosis, pulmonary fibrosis and kidney fibrosis since fibroblast activation protein is universal feature of activated pathogenic fibroblast. Furthermore, with knowledge of disease-specific enzyme-responsive materials, it can be broadened to other types of disease.

Taken together, the stimuli-activated drug delivery system is a promising microenvironment-targeted therapeutic option and has potential in terms of its compatibility with other synergetic systems.

요약

자극 기반 활성형 미세환경 내 약물 전달 시스템 개발 연구

서울대학교 대학원
약학과 약제학과 전공
변 준 호

질병 부위 내의 미세환경은 질병의 발달 및 치료에 중요한 역할을 담당한다. 질병 부위 내의 미세환경에서는 세포-세포간, 세포-환경간의 복잡한 상호작용이 일어난다고 알려져 있다. 따라서 미세환경을 어떻게 조절하느냐에 따라서 치료의 성공 여부에 큰 영향을 끼친다. 약물 전달 시스템을 이용하면 국소적인 질병 부위에 특이적으로 약물을 전달할 수 있다.

본 박사학위 논문에서는 이러한 점에 착안하여 자극에 기반하여 활성화되는 약물 전달시슽템을 개발하고, 이를 통해 질병의 미세환경을 조절하여 질병 치료 효과를 보고자 하였다. 약물 전달 시스템에 이용한 자극 및 미세환경의 활용 방법에 따라서 총 세 가지 주제로 연구가 진행되었다. 첫 번째와 두 번째 주제는 종양 모델에서의 항암 치료 및 미세환경 조절에 관한 연구이며 세 번째 주제는 간섬유증 모델에서의 섬유성 미세환경 특이적인 항섬유화 펩타이드 전달에 관한 연구이다.

첫 번째 연구는 종양 치료 및 종양 미세환경의 면역 활성을 위한 적외선/원적외선 감응형 금 나노클러스터에 대한 연구이다. 두 종류의 빛에 동시에 감응하여 종양미세환경 내에서 광역학치료/광열치료 효과를 동시에 유도할 수 있었다. 또한 면역원성이 있는 CpG DNA 가닥을 금나노클러스터의 주형으로 활용함에 따라 수지상세포를 활성화하였다. 이에 따라 종양 특이적인 T 세포 반응을 유도함과 동시에 원발성 종양 진행을 억제할 수 있었다.

두 번째 연구는 저온 대기압 플라즈마 감응성 하이드로겔을 기반으로 한 면역조절 나노입자 및 종양 항원의 지속적 전달 시스템에 관한 연구이다. 저온 대기압 플라즈마에 의하여 종양 조직 내부에 종양 항원과 면역 조절 나노입자를 포함하는 하이드로겔이 형성된다. 종양 내에 형성된 이러한 네트워크는 수지상세포와 T 세포를 하이드로겔로 유도하고 항암 효과를 나타낼 수 있는 종양 미세면역환경을 형성한다.

세 번째 연구는 간섬유증 미세환경 내에서 특이적으로 높게 발현하는

효소가 있다는 것에 착안하여 개발된, 간섬유증 특이적 항섬유화 펩타이드 전달 시스템에 관한 연구이다. 간섬유화를 일으키는 활성화된 간성상세포를 미세환경의 특징을 이용하여 특이적으로 사멸시킬 수 있었으며, 미세환경 내에서 간성상세포의 비율만 낮출 수 있었다. Bile duct ligation, CCl_4-induced fibrosis 그리고 지방간 기반 간섬유증까지 총 세 가지 간섬유화 모델에서 항섬유화 효과를 확인할 수 있었다.

이상의 연구들을 통하여 외부 자극을 통한 면역미세환경 조절 및 미세환경 내 내부 자극을 이용한 미세환경 조절을 약물전달시스템에 적용하였을 때 질병의 치료에 유의한 효과를 유도할 수 있다는 것을 확인할 수 있었다. 하지만 연구 별로 한계점이 존재하였다, 광열치료와 광역학치료에는 이를 유도할 수 있는 치료 물질이 포함되어야 하는데, 이 역시 임상적으로 사용되는 약물을 세심히 고를 필요가 있을 것으로 생각된다. 저온 플라즈마의 항암 치료에의 적용은 신규한 치료 방법이지만 그만큼 임상적으로 확인된 케이스가 적으므로 관련하여 더 많은 데이터를 축적할 필요가 있으며, 조직 내에서 플라즈마 기체가 작용할 수 있는 깊이가 깊지 않을 것이기 때문에 적용하고자 하는 종양의 크기가 치료 효과에 크게 영향을 끼칠 것으로 사료된다. 간섬유증 치료용 펩타이드의 전달은 치료 모델로서 간섬유화 모델을 이용했지만, 섬유아세포가 관여하는 다양한 섬유성 질환에 활용할 수 있을 것으로 사료된다. 다만 미세환경 내의 면역 세포 역시도 섬유증에서 중요한 역할을 담당하고 있다고 알려져있는데, 면역 세포의 변화를 평가하기 위해서는 추가적인 phenotype 연구가 필요하다. 본 연구에서는 흔하게 사용되는 페길화된 리포좀 제형을 사용하였으므로 제형 상 개선의 여지가 있으며, 세포를 표적화 할 수 있는 리간드와 함께 작용한다면 용량 대 약효를 더욱 증진시킬 수 있을 것이다.

질병의 미세환경은 복잡성을 띄고 있으며 질병의 종류 및 질병의 진행 정도에 따라, 그리고 개체 별로 큰 차이가 있을 수 있기 때문에 실제 임상에서는 효과가 어떻게 나타날지는 미지수이다. 또한 종양과 섬유성 질환 이외에도 미세환경 조절을 위한 약물전달 시스템을 개발하기 위해서는 더욱 넓은 범위의 연구가 필요하다. 따라서 자극 기반 약물전달시스템을 질병 미세환경에 적용하기 위해서는 질병 별로 보편성을 가지는 요소를 활용하여 질병에 적절한 자극을 선택하는 것이 중요할 것이다. 특히 저온 대기압 플라즈마를 포함한 외부 자극의 경우 대부분 피부 표면과 가까운 부위로 적용이 제한된다는 한계점이 있으므로 치료용 기기 등을 이용하여 이러한 한계를 극복하려는 노력이 필요하다.

여러 한계점에도 불구하고 미세환경의 조절과 국소적인 자극을 기반으로 한 약물전달 시스템의 시너지 효과는 주목할만한 잠재성을 가지고 있다. 특히 종양 및 섬유성 질환처럼 기존 치료법에 한계가 있는 질병에 대해서 본 연구에서 제시된 지극 기반 미세환경 조절용 약물 전달시스템은 유망한 치료 선택지가 될 수 있을 것이다.

주요어: Drug delivery system, tumor microenvironment, immunotherapy, fibrotic microenvironment, biologics delivery

학 번: 2017-20756